Cold Atoms Trapped near Surfaces

Daniel Sahagún Sánchez

July 2006

Thesis submitted in partial fulfilment of the requirements for the degree of Doctor of Philosophy of the University of London and the Diploma of Membership of Imperial College.

Imperial College, London
University of London

Abstract

Cold Atoms Trapped near Surfaces

Daniel Sahagún Sánchez

I report on experimental research towards the quantum control of cold atoms and Bose-Einstein condensates on atom chips, where atoms are trapped near dielectric or conducting surfaces.

We investigated in detail two decoherence mechanisms related to the interaction between the atoms and the surface of a conducting wire. Firstly, the coupling between the spin of atoms and the magnetic noise field of the wire induces spin flips. Such transitions contribute to undesirable atom loss from the trap, resulting in a lifetime less than 10 s when the atoms are held closer than 30 μm from the surface of the wire. We measured the lifetime of our trap as a function of the distance from the surface for two different spin-flip transition frequencies and eventually theory did achieve agreement with our results. This was the first observation of thermally driven spin flips near a surface, as opposed to technical noise. Secondly, we studied the atom cloud fragmentation in our trap which is caused by an anomalous component of the magnetic field parallel to the wire. We demonstrated that the field causing fragmentation decays with the distance y from the surface as a modified Bessel function of the second kind $K_1(2\pi y/\lambda)$, where λ is its spatial periodicity. This behavior is expected from a meandering current flowing inside the wire, which we surmise was due to defects in its internal structure.

After understanding the limitations on the control of atoms with atom chips, we continued to pursue the final goal of this project: atom interferometry on an atom chip. The last part of this thesis describes our first steps in this direction. I describe the inclusion of a new atom chip in the apparatus and the first experiments in which atoms were trapped on it.

Acknowledgments

Finally! It took me twice as long as I thought but this thesis is written and I'm not becoming part of Blackett's furniture. There are many people that were somehow related to it and it's only fair for me to take some time to thank all of them. I'll do it in chronological order. So don't be hurt if you are the last!

Mom and Dad, you are the base that never fails to provide me with support whenever and wherever I need it. For this PhD, it had to be transatlantic and I felt you always were backing me. Thanks for that and for loving me so much. Sepan que los amo con todo mi corazón.

Sisters, Vero and Ale. We've been apart physically but I think we are just getting closer. I know life hasn't been easy for you these recent years but we will always have passion to get us through the problems. See you soon!

Pepe, my sensei. Thanks for all the sincere advise you gave me when making hard decisions. I do really hope that we will get to work together again.

This bit is for the Manchester people. I want to express eternal gratitude to Helen Gleeson. I'll never forget how, regardless that it meant I would leave, you put me on track to what I think is my vocation. Andrew Murray, I bet you don't know the way in which you lecture changed my life! Thanks for that fantastic course. Nick and Helen, you guys are probably the reason that took me up north, a friendship for ever.

Ed, the wizard. It was a great honor (what took me a while to get used to) to be your apprentice. From you, I learnt that physics is really a game. Thanks for teaching me how to play Physics and for your patience.

Matt and Chris (Vale). Thanks for get me started in the lab. Certainly this thesis would't be the same without you guys. It's a pity you left so soon!

Here I thank to everyone, who shoulder to shoulder, fought against the MOT mice, mythologic characters that prevented us to trap atoms when we first moved to Imperial. First, Chris (Sinclair) and Paul for being my friends since we commenced together at Sussex. But also Ben, Jony, Mike, Stefan (thanks for your teaching in the lab and your empathy towards the end of this thesis writing), Anne and Brenton. Also

thanks to the bunch of great people who came along later, joined us in the effort and made the lab a very friendly place to work: Isabel, Rob, Jonathan, JILA Jon JILA ..., Fernando, Manu, Benoit and Gabriel. I hope not forgotten anyone! It was good that we managed to bring the lab happiness index higher up, which is proportional to the number of existing MOTs, from zero to.....three, four, five? I've lost count already. Recent investigations indicate that some of the mice were Mexicans. Figure 1 shows an image of a hat left by one of the mice when they were surprised, while celebrating a partial victory, by the imaging beam. Presumably they jumped on my baggage in one of my trips. Sorry! Also thanks to Jon Dyne for his excellent technical assistance.

Stefan Scheel, thanks for explaining me your theory and for your corrections to that bit of the thesis.

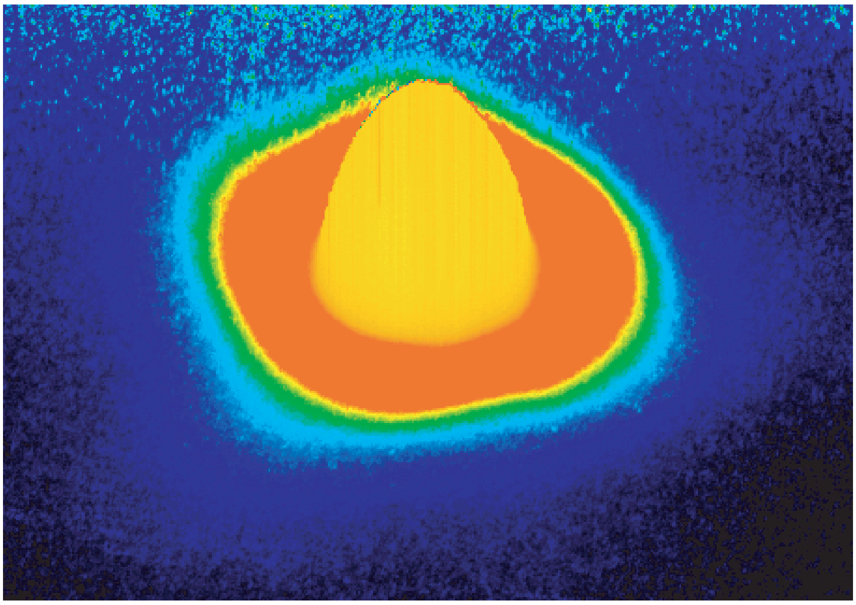

Figure 1: Evidence of one of the celebrations of the MOT mice when we were losing the battle. The party was interrupted by the imaging beam, which obviously scared the mouse who owned the hat.

Lorena, it's hard to acknowledge you here, in a few words because you're fundamental part of the biggest breakthrough in my life. I do really hope we both reach happiness quite soon.

Yellow? I want to shout a big: thanks!!! To the friends that kept my chin up when I was struggling: Robertito (thanks for allowing me in your room for 3 months, for listening and in general for being such a good friend), Olivita (remember: not even a year), Marianito, Evita, Isabelita, Alaita, Pablito, Miguelitos (the two of them) and of course, to Ben. Thanks for giving me shelter and a supporting shoulder on which I could cry without worries. The story just commences here my friends.

This is a second thanks to Olivita because I thought she'd like it.

Finally, to the Capoeria people, thanks for the therapy. If there is still some health in my mind is pretty much thanks to that..... salve!

This PhD was partially funded by the National Council for Science and Technology of México (CONACyT).

Contents

List of Figures

List of Tables

Chapter 1

Introduction

1.1 History of Atom Optics

The birth of quantum mechanics in the beginning of the last century led to the growth of diverse streams in modern physics. One of them is the study of matter waves. This research field was pioneered by W. Gerlach and O. Stern, who in 1921 deflected for first time a beam of neutral atoms with an inhomogeneous magnetic field [1]. This can be considered as the construction of the first spin polarizer beam splitter for neutral atoms. For more than five decades, the research in this field was constrained to highly-energetic wave packets using beams of atoms or molecules with a broad velocity distribution produced by ovens.

Atom optics, the study of thermal de Broglie waves, had a big step forward when lasers were invented in 1960 [2]. The availability of coherent optical fields opened the possibility to cool atoms efficiently with the radiation pressure of light. Amongst other implications, cooling atoms to low temperatures would bring the possibility of producing long matter waves, to create de Broglie waves whose wavelength

$$\lambda_T = \sqrt{\frac{2\pi\hbar^2}{mk_BT}}, \tag{1.1}$$

is in the micrometer scale. This length scale is comparable to the size of trapping potentials that could be created in research laboratories. In Equation (1.1), $\hbar$ is Planck's constant, m is the atom mass, k_B is the Boltzmann constant and T the thermal temperature of the atoms.

On the other hand, cooling atoms with laser light also would enable their confinement through weak couplings such as their interaction with magnetic fields. Both creating long de Broglie waves and enabling their confinement, would allow researchers to develop Atom Optics. However, these two pursued goals had to wait for further improvement of the laser technology and a better understating of the interaction between coherent light and atoms.

Laser cooling was first demonstrated with magnesium ions inside a Penning trap in 1978 by Wineland *et al.* [3]. Because they are charged, ions are strongly coupled to electric fields. Thus they can be first trapped and subsequently laser cooled. Neutral atoms have to be cooled before their interaction with magnetic fields is strong enough to trap them. Stopping neutral atoms so they could be trapped was attractive because they are weakly coupled to their surroundings and hence, it is relatively simple to create isolated systems with them.

The alkali group of elements were good candidates to be laser cooled because their D-lines are optically excitable with available laser technology. Sodium was the first species to be laser cooled; a beam of Na atoms was cooled down to 40 % of its initial thermal energy in 1982 [4, 5]. Thereafter laser cooling of Na was reported down to the Doppler limit (240 μK) by S. Chu *et al.* [6] . In this experiment, atoms were cooled along the three spatial dimensions with six counter propagating laser beams, a technique that the authors called ‘optical molasses’. Cooling below the Doppler limit was achieved in 1988 by Phillips *et al.* [7] with the use of polarization-gradient forces in the optical molasses [8, 9]. By 1989 researchers were able to routinely laser cool atoms down to a few tens of microkelvin. At such temperatures, a large fraction of the atoms have small enough kinetic energy to be trapped by magnetic or optical forces.

In parallel with the development of laser cooling, techniques to confine atoms with magnetic [10] and optical [11] forces were proposed and demonstrated. In order to confine atoms in these two types of trap, atoms were laser cooled with optical molasses. The combination of sub-Doppler cooling in optical molasses and magnetic trapping, led to a big boost in the research on matter waves in 1995. This was the independent achievement of Bose-Einstein condensation (BEC) in dilute gases of three different alkali species: Rubidium [12], Lithium [13] and Sodium [14]. BEC in dilute-alkali gases was first achieved using evaporation techniques [15] in magnetic traps.

A Bose-Einstein Condensate (or just ‘condensate’ in this thesis) is formed when the spacing between atoms is equal to λ_T. When BEC occurs, a significant fraction of particles in an ensemble occupy the ground state of the system. Then all atoms belonging to the condensed fraction behave together as a single matter wave. The achievement of BEC signified both the availability of big matter waves and a source of coherent atoms. It was in the mid-90s, greatly supported by the achievement of BEC, when the research field on matter waves of neutral atoms finally acquired its current name – Atom Optics.

1.2 Guiding atoms near wires

By the mid 90s, a wide range of experiments practically enabled researchers to prepare atom clouds with any desired temperature between five hundred kelvin and a few hundreds of nanokelvin. Techniques to create de Broglie waves and to manipulate them with magnetic fields became standard. The next step was to build devices that prepare and control atoms in fully defined quantum states of both internal and external degrees of freedom.

One of the answers found by researchers for the manipulation of matter waves are the guides for neutral atoms. These are potentials in which the motion of atoms is constrained to a line or a plane. With atom guides, it is possible to store atoms for relatively long times and atoms can be transported for example by simply tilting the potential. Many guides for neutral atoms have been proposed using the potential of optical [16, 17, 18, 19], electric [20] or magnetic [21, 22] fields. Magnetic potentials have been of great use to guide atoms since the first achievements of BEC. Specifically, guiding atoms with the field created by current carrying wires has been one important stop towards quantum control of neutral atoms.

As well as in three dimensional magnetic traps, neutral atoms are magnetically guided by the Stern-Gerlach force. The potential energy that is associated to this force, is the projection of their magnetic dipole moment $\boldsymbol{\mu}$ onto the local magnetic field $\mathbf{B}$,

$$U = -\boldsymbol{\mu} \cdot \mathbf{B}. \tag{1.2}$$

The orientation of $\boldsymbol{\mu}$ with respect to $\mathbf{B}$ depends on the internal energy state of the atoms. Atoms whose dipole moment is antiparallel to the local magnetic field have a positive potential energy given by Equation (1.2). Therefore they find their minimum energy state in magnetic field minima. These are called low-field seeking atoms. Conversely, if the internal quantum state of the atoms is such that their dipole moment is aligned with the local magnetic field (in which case U of Equation (1.2) is negative), they find low energy states in regions of high magnetic field. Atoms whose quantum state satisfies this condition are called high field seeking atoms.

Both high and low field seeking atoms can be guided with fields generated by current carrying wires [22, 23]. It is not possible to create local magnetic field maxima. Which means that high-field seeking atoms cannot be guided by DC magnetic fields alone. On the other hand, low field seeking atoms can be either trapped or guided with field minima, such as in the centre of a quadrupole magnetic field. These fields can be produced with current flowing through coils, wires or a combination of them.

The simplest configuration of fields in which low field seeking atoms are guided

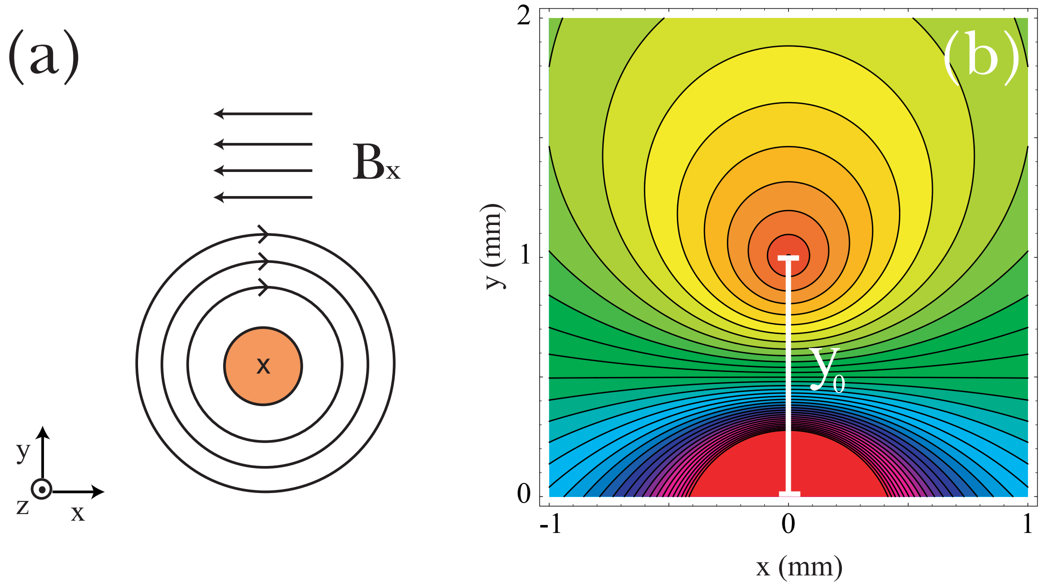

Figure 1.1: A simple way to create an atom waveguide with a current carrying wire. A wire carrying current flowing into the page plus a bias field B_x (a), creates a magnetic quadrupole with cylindrical symmetry whose axis lays parallel to the wire. The contour lines of the resulting magnetic field magnitude are shown in (b), where red and blue indicate regions of low and high field correspondingly. The centre of this waveguide (0,y_0) can be shifted in the vertical direction by changing the current I through the wire or the bias field B_x.

with a current carrying ('guide') wire is illustrated by Figure 1.1. The solid circle in Figure 1.1 (a) is the cross section of a wire, carrying a current that is flowing into the page – antiparallel to z. The straight arrows in Figure 1.1 (a) represent a bias field B_x in the -x direction that cancels the circular field at a distance

$$y_0 = \frac{\mu_0 I}{2\pi B_x} \tag{1.3}$$

from the centre of the wire as shown in Figure 1.1 (b). In a vicinity of this point, the created field can be considered as a quadrupole with cylindrical symmetry. Its centre follows a zero-field-line, parallel to the axis of the wire.

Figure 1.1 (b) is a cross section of constant magnetic field magnitude produced by the current through the wire and the bias field B_x on the xy-plane. The point (0, y_0) in which the field is zero, is the centre of a long guide for low field seeking atoms [23]. The restoring force of the trap is proportional to $\mu B_x/y_0$ as we discuss in Chapter 2. This is enhanced at small y_0 which is readily exploitable if one uses wires with microscopic cross sections. Near the surface of micron-scaled wires with moderate currents (on the order of one Ampere), this can provide us with traps whose ground state separation from the first excited is greater than the kinetic energy of the atoms achieved by standard cooling techniques [24, 25, 26]. This opened the possibility to guide single mode matter waves with magnetic fields.

The atoms' motion can be suppressed in a selected direction if the guiding potential constrains them to a shorter distance than their thermal de Broglie wavelength λ_T. λ_T is typically under one micrometer for atomic Rubidium in dilute gases at microkelvin temperatures. Due to the large field gradients achievable near microscopic wires, one can create guides whose ground state size is of the order of λ_T in the plane perpendicular to the wires [26]. Restricting the motion of atoms in these two dimensions would enable us to investigate the physics of ultra cold atoms in one dimension.

Near micro-fabricated wires, we can create potentials by which single mode matter waves are stored and transported in a chosen direction of motion. An atom guiding potential with these characteristics has been named 'waveguide' in analogy to microwave and optical waveguides.

1.3 Matter waves on atom chips

Atom chips have the potential to become a complete tool box of atom optical instruments, and have been in development since the first proposal of traps near microfabricated field sources – 'microtraps' – in 1995 [24]. The atom chip idea is to create small and strong potentials based on microscopic structures – to combine the availability of ultra cold atoms with micro or even nano-technology capable to build wires, magnets and optics components. Creating potentials with microscopic field sources enables us to form systems whose characteristic energy is greater than the kinetic energy of cooled atoms and whose ground state is comparable to the atom's de Broglie wavelength. All this is achievable with small power dissipation in the field sources.

The goal with atom chips, similarly with microelectronics chips where electrons are stored and transported to realise elaborated tasks, is to build circuits of cold atoms. Such circuits are built with magnetic, electric and optical potentials created with wires, permanent magnets and photons forming complex patterns. An atom chip is an Atom Optics device in which all these types of fields are integrated.

A fair amount of the technology required to build atom chips was already available in the late 90s. This allowed researchers to show the feasibility of the atom-chip proposals [25, 27, 20]. Trapping and guiding potentials near micro-fabricated structures were designed and successfully employed to manipulate atoms previously cooled by magneto-optical trapping techniques [28, 29]. Such potentials were long waveguides and three dimensional traps that nowadays are the building blocks of more complicated circuits in which neutral atoms are transported and stored. The microtraps complexity grew rapidly. Cold atoms were first magnetically guided along straight lines with diverse configurations of wires [30]. Waveguides with more complicated shapes, such as curves were also demonstrated with current carrying wires [31]; a beam splitter with Y-shape was built by combining current carrying wires and a bias field [32]. Transport of atom clouds confined in three dimensions was also demonstrated with the construction of a conveyor belt based on current carrying wires [33].

A major breakthrough in the Atom Optics research with atom chips was the achievement of BEC in 2001 by two independent groups [34, 35]. This signified the availability of coherent matter waves combined with the power and flexibility in the manipulation of cold atoms already demonstrated with microtraps. Storage and transport of single mode matter waves then became possible with atom chips.

Our research group was amongst the first to achieve BEC on atom chips [36, 37]. This gave us the capacity to position clouds of ultra cold atoms or condensates above a guide wire with an accuracy of the order of micrometers. We used atoms that were previously evaporatively cooled to probe the field near the surface of our guide wire. The interaction of atoms with the DC and AC field near surfaces lead to decoherence effects in microtraps. Probing surfaces to build atom chips is the main topic of this thesis. It is first extended in Section 1.4, and our work is explained in detail by chapters 3 and 4. Several other groups also realized these studies with different types of materials that can be used to build atom chips. These investigations led to optimize the materials and building methods used in the construction of subsequent atom chips.

The preparation of Bose-Einstein condensates on atom chips is now a standard process. The possibility to carry out powerful applications such as single mode atom interferometry is open. Interference between condensates on a chip was first observed with optical potentials [38]. Tailored micron-size potentials near conducting wires have already produced BEC interference [39]. Integrating RF fields to the atom-chip tool box has enabled researchers to create deterministic BEC interference, and controlled-quantum tunnelling is likely to be observed in these systems [40]. Quantum matter, subject to microscopic potentials displayed diffraction of matter waves up to the fifth order in recent beautiful experiments [41]. Which in turn is a fundamental step on a different path towards atom interferometry [42].

So far, a significant portion of the new physics with atom chips has been realized with magnetic potentials created by current carrying wires. However a promising alternative for magnetic confinement is to use permanent magnets. This possibility on atom chips emerged from the realization of magnetic mirrors for neutral atoms [43]. The mirrors were made of surfaces patterned with permanently magnetized structures, such as audio or videotapes. For example, there is an ongoing project in our group in which cold atoms have been loaded into a microtrap on a videotape [44] and successfully evaporated to BEC [45]. This project is currently working towards the realization of the first conveyor belt for ultra cold atoms based on a permanently magnetized surface. Simultaneously the technology to improve this type of microtrap is being developed. Now our group is able to write permanently magnetized patterns on silicon surfaces that can create micron-sized magnetic traps [46].

Several groups have plans to integrate microscopic optical components to couple atoms with small-waist laser beams. Microscopic fabrication of optics elements can lead to accuracy capable to detect single atoms [47]. Our group has also made experimental progress in this direction. An (absorption) imaging system accurate enough to detect tens of atoms is being developed with tapered fibres, as well as microscopic optical cavities in which it will be possible to detect a single atom [48].

There is much activity and effort being invested in order to complete the tool box of atom chips for the research on atom optics systems such as one dimensional quantum gases [49, 50], cavity quantum electrodynamics with atoms [51, 52], and atom interferometry [40, 39, 42]. These applications could lead to quantum gates for information processing with neutral atoms [53, 54].

1.4 Decoherence in microtraps

Atom chips potentially can provide full quantum control of cold atoms and condensates however, there is a fly in the ointment. There are decoherence effects in microtraps that become accentuated when atoms are located near the surface of atom chips. Amongst other research groups, we studied the interaction of ultra cold atoms with the surfaces of atoms chips. These investigations provided us on one hand, with a way to understand the limitations of the systems, as well as to improve the design for future atom chips. On the other hand, understanding this coupling opened a branch of interesting experiments and applications in which the field near surfaces can be characterized in an systematic manner.

Once BEC was achieved in microtraps, researchers immediately probed the (room temperature) surface of atom chips with atoms cooled at microkelvin temperatures and found three decoherence effects. Two of these effects, both consequences of the coupling of atoms with the AC field near surfaces, were already expected [55]. A third one, corrugations in the trapping potential due to the DC field near surfaces, was first found and then explained.

Firstly, theoretical studies predicted that the coupling between the near field at (audio) frequencies resonant to the trapped systems would lead to excitation of atoms, heating up the cloud. The principal source of this signal is technical noise, mechanical oscillations of the experimental equipment. The heating rates generated by audio frequency (AF) noise can normally be controlled and do not represent an obstacle for coherent control of atoms.

A second problem, whose origin is related to more fundamental physics, is derived from the spin coupling of atoms with radio frequency RF fields – thermal field fluctuations with frequencies from 100 kHz to 10 MHz. This is the typical frequency range of electron spin transitions in trapped atoms. Without appropriate care, spin-flips can become a major loss mechanism of atoms in magnetic traps. Spin flips induced by the thermal fluctuations of free space cause spontaneous decay at a very small rate that is not measurable during experimental time scales. Near surfaces however, the thermal oscillations of the vacuum field are enlarged by additional modes due to the presence of materials such as conductors or dielectrics. The rates of spontaneous relaxation in the trapped states are dramatically increased at tens of micrometers from the surfaces. This is an atom loss mechanism in microtraps that depends on the materials used to build atom chips. Spin flips are the same type of transitions that are employed in evaporative cooling techniques, leading to BEC in some of the alkalis.

The third effect of decoherence in microtraps was only found when condensed atoms were lowered closer to the surface of the atoms chips. The DC field near the current carrying wires showed deviations (about 1 part in 10^4) from the circular field induced by a straight current. These field deviations formed corrugations in the trapping potential that were greater than the typical BEC chemical potential, which is of a few hundreds of nanokelvin. At distances shorter than one hundred micrometers, this anomalous field is enough to break condensates or clouds of ultra cold atoms into lumps (see Figure 4.4), signifying a possible limiting effect on the spatial control of matter waves in microtraps.

We observed and studied in detail the three decoherence effects in a microtrap created near a single guide wire. Our results, combined with those of other research groups, led to a good understanding of the decoherence phenomena in cold atoms near the surfaces of atoms chips. This work enabled the atom chip community to find more suitable materials and techniques to build atom chips.

1.5 Overview of this thesis

This thesis is, in a manner of speaking, backwards. I started with a working apparatus and used it to study spin flips and atom cloud fragmentation. Only towards the end did I design and build an apparatus, which is now being used by the next PhD student.

The work being reported is part of a research project that has the ultimate goal to realise coherent control of matter waves on an atom chip. Reaching this goal requires the understanding of decoherence effects in atoms trapped near the surfaces of atom chips. Our studies on this subject were done with an atom chip that has a single guide wire (see Figure 2.10) on which we can create long microtraps based on the waveguide scheme illustrated by Figure 1.1. The experimental setup in which we carried out these investigations is the subject of Chapter 2. That chapter describes the cooling and trapping sequence that we used to routinely cool atoms down to BEC.

A theoretical description of thermally induced spin flips causing atom loss near the surface of atoms chips is presented in Chapter 3, followed by a description of the experiments we carried out to investigate this phenomenon. Next, I present the first measurements of thermally induced spin-flip rates near surfaces to be free of technical noise [56]. The last section of this chapter also presents a comparison of our results with the theoretical predictions by Henkel *et al.* [55] and by Rekdal *et al.* [57]

Our investigations of atom cloud fragmentation are described in Chapter 4. To understand this phenomenon, we investigated how the unwanted field causing fragmentation decays as a function of distance from the wire [58]. Our results on atom cloud fragmentation are presented there, together with a comparison with a model in which the anomalous potential is generated by a meandering current. Excellent agreement was found with this model.

Chapter 5 describes our initial work on a lithographically patterned atom chip. The changes carried out in order to incorporate the new chip into the experimental setup are described as well as the first experiments in which we trapped atoms on this atom chip. The conclusions and a summary of this thesis are presented in Chapter 6.

Chapter 2

Cooling and trapping rubidium atoms

The main body of this thesis is our research on the surface effects inducing decoherence in microtraps. These investigations were realized in an atom-chip setup that enabled us routinely to prepare condensates in dilute gases of ^{87}Rb. The present chapter describes the layout of our BEC apparatus, and the sequence of cooling and trapping techniques that led our group to be one of the first to make BEC on an atom chip [37, 36].

2.1 Overview

In every BEC setup, a series of cooling and trapping techniques aims to increase the phase-space density ρ_{PS} of an ensemble of atoms. The phase-space density is defined as the number of atoms contained in a cube with side equal to their de Broglie wavelength λ_T [Equation (1.1)]:

$$\rho_{\mathrm{PS}} \equiv n \left(\frac{2\pi\hbar^2}{m k_B T} \right)^{3/2}, \tag{2.1}$$

where n is the atom number density and T is the temperature of the atoms.

Every cooling and trapping technique applied in an experimental sequence to reach BEC aims either to increase the atom density or to decrease the temperature. BEC happens when the interatomic distance becomes comparable to λ_T, the thermal de Broglie wavelength of the atoms in the dilute gas. Then a large fraction of the atoms are in the ground state of the system. For atoms confined in a three dimensional harmonic potential, the phase transition occurs when $\rho_{\mathrm{PS}} = 2.612$, see for example [59].

In our experiments, the process of reaching BEC is started with atomic rubidium dispensed at temperatures of about 500 K inside the vacuum chamber with a typical base pressure of 10^{-10} torr and a number density of about 1.9×10^{6} cm^{-3}. Thus at this initial stage $\rho_{\mathrm{PS}} = 1.1 \times 10^{-21}$ in our experiments. The space-phase density of the dispensed dilute gas is to be increased by 21 orders of magnitude in order to reach BEC. The first cooling stage in our experiment is a magneto-optical trap (MOT) in which 1 $\times 10^{8}$ atoms of ^{87}Rb are cooled down to $T = 50$ μK and confined in a roughly spherical volume of about 4 mm diameter. In the magneto-optical trapping stage, ρ_{PS} is increased to 5.5×10^{-7}. The MOT is then compressed to an elongated shape for a further increment of ρ_{PS} in the atom cloud. Once the MOT is compressed, atoms typically have a temperature of 85 μK and the phase space density is increased to 1.4×10^{-6}. After the compressed MOT stage, the trapping light is turned off and the atoms are optically pumped to the $5S_{1/2}, | F = 2, m_F = 2\rangle$ sub-level of ^{87}Rb which is a low field seeking state. Another reason to compress the the MOT is to match the size and shape of the magnetic trap which has the form of a cigar. The microtrap is immediately switched on after optical pumping, capturing about 1.5×10^{7} atoms. The next step is evaporative cooling, which works well when atoms have a fast collision rate with each other. To achieve this, we compress the atom cloud by increasing the magnetic field gradient in the two transverse directions of confinement, increasing the aspect ratio of the cigar-shaped cloud. The hottest atoms in the compressed magnetic trap were evaporated by forced RF evaporation. With evaporative cooling we are able to reach any chosen temperature down to 100 nK [1], well below the BEC critical temperature of our system which is around 390 nK.

2.2 The laser system

The optical arrangement of this BEC apparatus prepares laser light to excite transitions in the D2 line of ^{87}Rb, which is resonant at $\lambda = 780$ nm. Three lasers supply the light interacting with atoms in our experiment. The source of trapping light is a Ti:Saphire laser, pumped with green light from a Verdi laser. Light for other diverse purposes is supplied by two diode lasers that were built by our group at Sussex University with a home made design based on a extended cavity scheme [60].

2.2.1 The D2 line of ^{87}Rb

Alkali atoms are commonly used for cooling and trapping experiments because they are accessible, relatively easy to manipulate and their D lines have transitions that are excitable with accessible laser technology. Specifically the D2 line of ^{87}Rb – shown in

---

[1] Trying to cool atoms to lower temperatures with this routine of evaporation is likely to empty the magnetic trap.

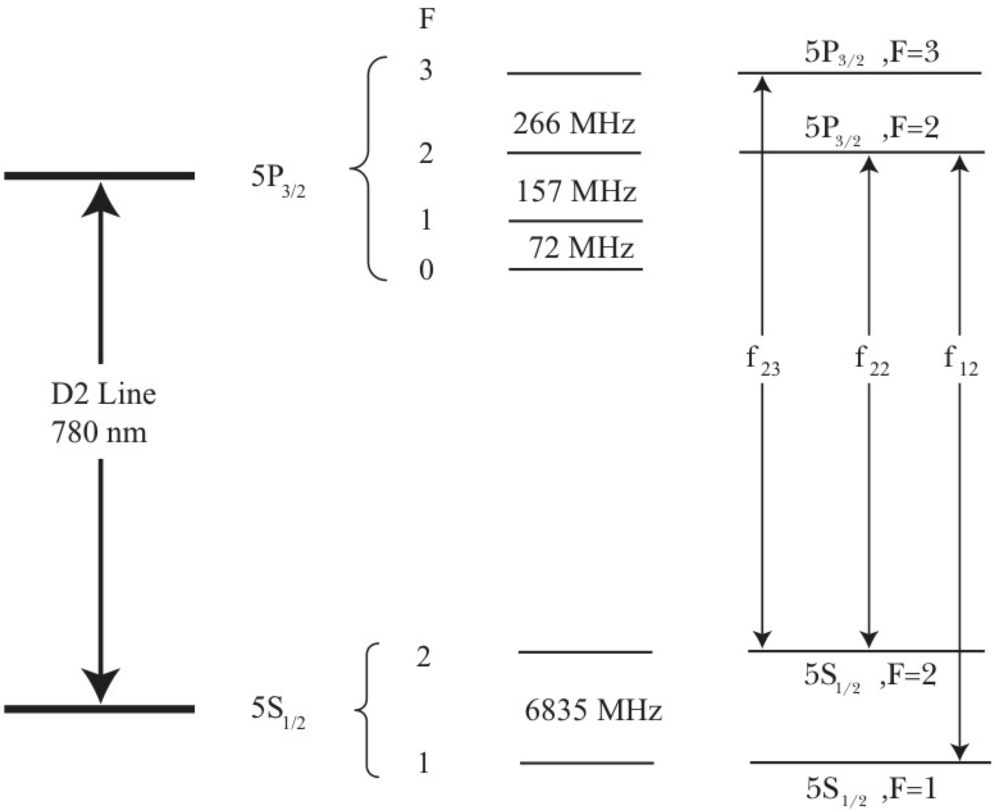

Figure 2.1: Transitions in the ^{87}Rb atomic structure employed in our experiment. These transitions are in the D2 line of ^{87}Rb which is resonant to 780 nm light. We exploit three transitions of this line: f_{23} to laser cool, trap and image atoms; f_{22} to optically pump atoms to the $5S_{1/2}, | F = 2, m_F = 2\rangle$ sub-level which is a low-field seeking state; and f_{12} to re-pump atoms to the trapping scheme. The hyperfine splitting values of the ground state $5S_{1/2}$ and excited state $5P_{3/2}$ were extracted from [61] and [62] respectively.

Figure 2.1 – connects the ground state $5S_{1/2}$ and excited $5P_{3/2}$ state of the isotope. This line has two optical transitions that are useful for laser cooling and trapping, resonant to f_{23} and f_{12} in Figure 2.1. The D2 line of ^{87}Rb also has a transition that is used to prepare atoms for magnetic trapping, whose resonant transition is f_{22} in Figure 2.1. The laser technology to produce light at these frequencies has been available for a couple of decades and has become relatively cheap with diode lasers. Thus atomic ^{87}Rb is now a workhorse to prepare condensates in Atom-Optics laboratories worldwide and also is the isotope used in our experiment.

The hyperfine structure of ^{87}Rb has been resolved since the late 50s. In particular the hyperfine splitting of its ground state $5S_{1/2}$ and excited state $5P_{3/2}$ were measured for first time in [63] 1956 and 1958 [64] respectively. ^{87}Rb became of great interest for the atomic and molecular physics community due to its use for laser cooling and magnetic trapping experiments. During the last decade, the interest in this isotope increased because its collisional properties are suitable for evaporative cooling [65], leading to a relatively simple realisation of BEC. The resolution in the transitions of interest has become higher with improved spectroscopic techniques such as absorption spectroscopy, which was used to provide the most recent and accurate measurement of the $5P_{3/2}$ excited state of ^{87}Rb [62]. Spectroscopy of laser cooled atoms has also provided the most precise measurement of the ground state $5\mathrm{P}_{1/2}$ splitting ^{87}Rb [61]. These are the values of splitting shown in Figure 2.1.

The radiation pressure needed to laser cool ^{87}Rb atoms is given by light tuned near the $5\mathrm{S}_{1/2}$, $F = 2 \rightarrow 5\mathrm{P}_{3/2}$, $F = 3$ hyperfine transition, labelled as f_{23} in Figure 2.1. After cooling, the atoms have to be placed in a stable low-field seeking state so they can be magnetically trapped. The Zeeman sub-levels $|F = 1, m_F = -1\rangle$, $|F = 2, m_F = 1\rangle$ and $| F = 2, m_F = 2\rangle$ of the $5\mathrm{S}_{1/2}$ ground state fit this description. Among them, the $5\mathrm{S}_{1/2}$,$| F = 2, m_F = 2\rangle$ state has the strongest coupling with the local magnetic field because it posses the biggest magnetic dipole moment. This hyperfine sub-level is the one we use to prepare atoms for magnetic trapping. We populate the $m_F = 2$ hyperfine state by optically pumping atoms with laser light tuned at the frequency f_{22} (see Figure 2.1), which is -266 MHz[2] from f_{23}. Optical pumping from the ground state $5\mathrm{S}_{1/2}$, $F = 2$ to the magnetic trapped sub-level requires the laser light to be σ^+ polarized with respect the atom's quantization axis.

Laser light tuned to the frequency f_{23} has a small probability of inducing off-resonance excitation of the $5\mathrm{P}_{3/2}$, $F = 2$ and $F = 1$ hyperfine sub-levels, which can decay to the $5\mathrm{S}_{1/2}$, $F = 1$ quantum state. This is -6835 MHz away from the $F = 1$ ground state, as shown in Figure 2.1, and is dark to the trapping light. Atoms in this state no longer feel the radiation pressure unless they are taken back to $F = 2$. This re-pumping is carried out by optically exciting the $5\mathrm{S}_{1/2}$,$F = 1 \rightarrow 5\mathrm{P}_{3/2}$, $F = 2$ transition. The 're-pump' transition, resonant to f_{12}, is also shown in Figure 2.1.

2.2.2 Preparation of the laser light

The light in our setup is supplied by a Ti:Saphire and two diode lasers. In this section I give a layout of the optics needed to laser cool and trap the atoms, prepare them for magnetic trapping, and take images of the trapped atom clouds.

The principal laser in our experiment is the Ti:Sapphire (model MBR-110), supplied by Coherent, Inc.. Its crystal is pumped by 532 nm light from a diode-pumped Verdi V8 laser from the same manufacturer. Both lasers appear in Figure 2.2. During most of the experimental time, the Ti:Sapphire is 106 MHz red-detuned from the trapping frequency f_{23}, giving a 300 mW output with 5 Watts of pumping power from the Verdi. About 220 mW of this power is passed through an AOM. The spot of

---

[2] In this thesis I use the convention in which the frequency of red detuned light is denoted as negative and the frequency of blue detuned light is denoted as positive.

first diffraction order from this AOM is up-shifted by 88 MHz respect to the original frequency ($f_{23} - 106$) MHz of the Ti:Sapphire. This is the main beam of trapping light as shown in Figure 2.2. We typically get 170 mW of trapping light once the beam has passed through the AOM. The final detuning of the trapping beam is -18 MHz from f_{23} as shown in Figure 2.2. The trapping light detuning is optimized against the atom number in the MOT. The main trapping beam is then divided into two 'MOT arms' [3] by a polarizing beam splitter. The re-pump light is incorporated to the MOT arms by overlapping it with the trapping beams through the same polarizing beam splitter as illustrated by Figure 2.2.

The source of re-pump light is one of the two diode lasers in the setup, shown in Figure 2.2. This laser is locked to the re-pump frequency f_{12} with an accuracy of one or two MHz by a polarization spectrometer [66, 67]. Both diode lasers are home built. Their design is a modified version of the scheme published in [60, 37]. The modification consists of the inclusion of a low-voltage piezoelectric stack element that enables us to scan the extended cavity through a 3GHz band around 785 nm, which is the nominal wavelength of the diodes (made by Sanyo, model DL7140-201). The two diode lasers output a power of 30 mW with an injection of 61 mA and a working temperature around 17 °C.

Our main laser, the Ti:Sapphire, is stabilized with its internal lock and tuned with a beat-note offset system. The Ti:Sapphire has a ring cavity tuned with an etalon and a birefringent filter. The ring frequency follows a reference cavity through a servo-electronics loop system. The reference cavity is externally tunable. We use it to change the laser frequency as appropriate for each stage of the experimental sequences. The offset frequency from f_{23} (equal to -106 MHz during the MOT and always around 100 MHz) is controlled by an implementation of the offset lock scheme proposed by U. Schünemann *et al.* [68]. This locking scheme is designed to compare the beat-note frequency from two lasers with the frequency of a voltage controlled oscillator (VCO). In our case, the beat signal is obtained by overlapping 2 mW from each of the Ti:Sapphire and the 'reference' diode lasers onto a fast photodiode located close to the centre of the optics arrangement, shown in Figure 2.2. The reference diode laser is locked to f_{23} by using a second polarization spectrometer on the optical table, see Figure 2.2. The beat-note signal is sent to the frequency control electronics, which in turn tunes the reference cavity of the Ti:Saphire. This locking system has the advantage of enabling us to change the Ti:Sapphire offset frequency in times as short as 5 ms [37].

---

[3] The names given in Figure 2.2 to the MOT arms, 45° and horizontal, correspond to the function of each one of them when creating the MOT. These functions are explained in Section 2.3

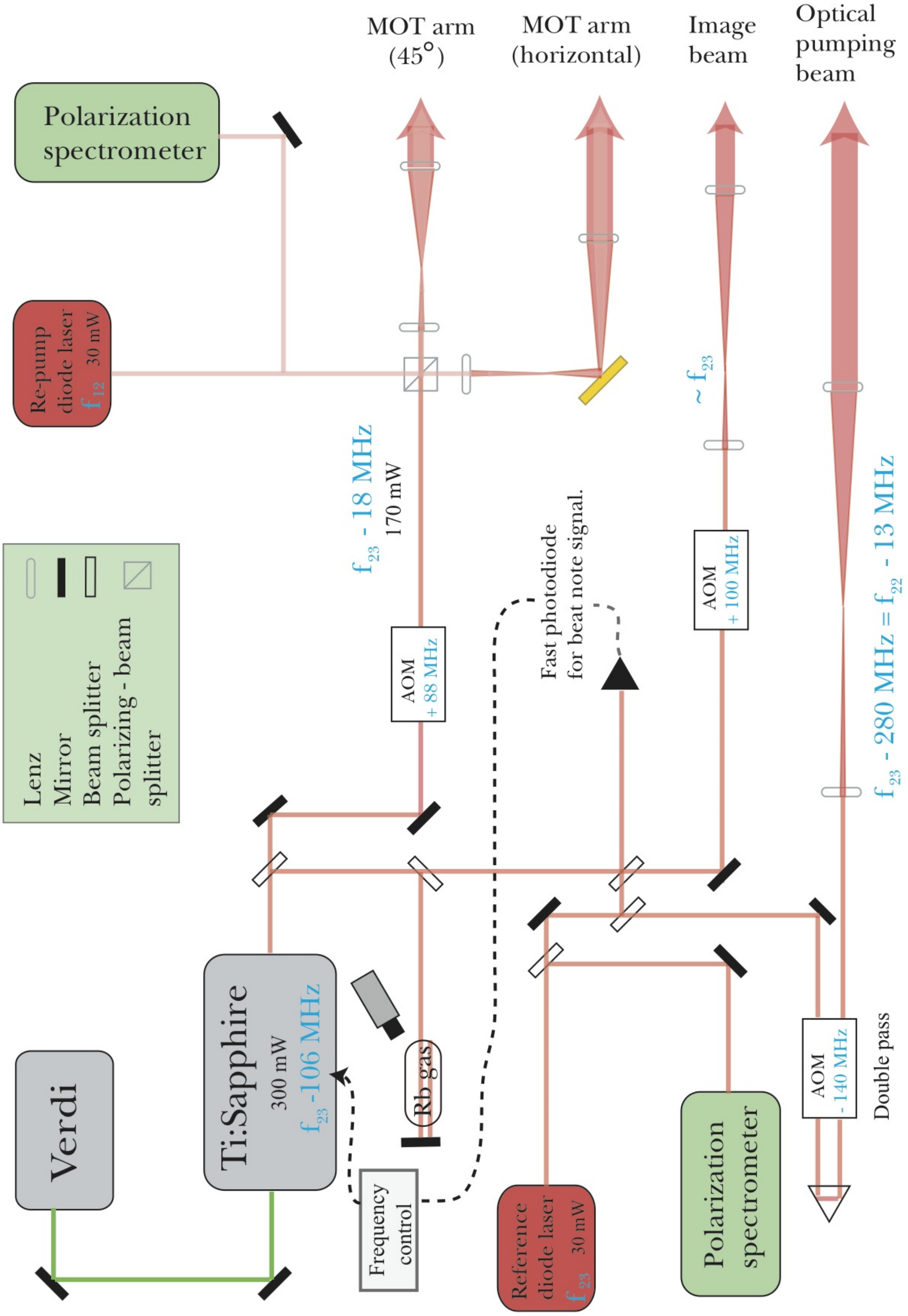

Figure 2.2: Layout of the optics arrangement used to prepare laser light for atom trapping and imaging. The Ti:Sapphire laser (pumped by the Verdi) is stabilized by a locking system in a beat-note scheme. The diode lasers are locked to the reference and re-pump frequencies (f_{23} and f_{12} respectively) using polarization spectroscopy. The re-pump light is incorporated to the MOT arms at the central polarizing beam splitter cube.

The reference laser also provides us with light to carry out optical pumping. The frequency f_{22} is 267 MHz tuned to the red of the reference (trapping) frequency f_{23}, as shown in Figure 2.1, but the optimum frequency is in fact 13 MHz to the red of f_{22}. This light is provided by splitting 5 mW from the reference laser and passing it twice through an AOM that is set to shift the light by -140 MHz per pass, as in Figure 2.2.

One moment during experiments, in which we have to change the offset frequency of the Ti:Sapphire, is when taking absorption images of atom clouds (see Section 2.2.3). This technique requires light that can be easily absorbed by the atoms. We use light with frequency near f_{23} so we can observe atoms in the trapped state. For absorption images the Ti:Sapphire is detuned 98.5 (instead of 106) MHz to the red from f_{23}. The 'imaging beam' is extracted from the output of the Ti:Sapphire and then shifted 100 MHz to the blue from $f_{23} - 98.5$ MHz by an AOM, see Figure 2.2.

2.2.3 Absorption imaging

Absorption images provided us with all the quantitative information about atoms that is contained in this Thesis. The present section explains the absorption imaging technique and its implementation in our setup.

In absorption imaging, the spatial density distribution of atoms is deduced from their shadow in a near-resonance laser beam, the imaging beam in our case. Figure 2.3 is a schematic of our absorption imaging system. The imaging beam is +1.5 MHz detuned from f_{23} in compensation for the Zeeman shift of atoms due to the imaging field, which is a uniform field of 0.1 mT in the x-direction (B_{xu} in Figure 2.3). The imaging beam is spatially filtered by a 40 μm pinhole and collimated with a spot size of about 12mm FWHM and 2.5 mW total power before entering the vacuum chamber. The polarization state of light is σ^+ with respect to B_{xu}. It is set by a $\lambda/4$ wave plate placed in front of the first imaging view port as shown by Figure 2.3.

In our BEC apparatus, images are captured by a Pentamax (5MHz) CCD camera. The CCD chip is an array of 1317 × 1035 square pixels with 6.8 μm side and 400-1080 nm spectral range. The shutter of the camera has a minimum exposure time of 10 ms. A minimum wait of 500 ms has to be left between images to allow total chip readout. During an exposure, through a 12 bit digital-to-analog converter (DAC), each pixel sums up to 4095 counts before saturation. Each 780 nm photon detected by a pixel is equivalent to 0.0256 counts read from the CCD chip. The imaging lens is a Comar aplanatic-doublet (model 03 TT 25) with 80.5 mm nominal focal length. It is located about 150 mm from the place where atoms are trapped. Deduced from the image and object distances, the magnification of this imaging system is 1.22(3).

The imaging beam is aligned straight across the vacuum chamber, passing through the centre of the imaging lens as shown in Figure 2.3. Its incidence angle to the normal of the CCD chip is 27.4°. Normal incidence of the imaging beam on the CCD chip creates fringes on the beam profile that are not completely removed when processing the images to eliminate the background signal. The origin of these fringes is a Fabry-Perot effect on the coherent light due to multiple reflections on the two windows in front of the chip. Their lack of reproducibility is likely to be due to vibrations on the camera when triggering its optical shutter. The best incidence angle was found empirically by making imaging tests [37]. Accounting for the incidence angle, together with the magnification provided by the imaging lens, each pixel is equivalent to an area $A = 4.95 \times 5.55$ μm of the real image.

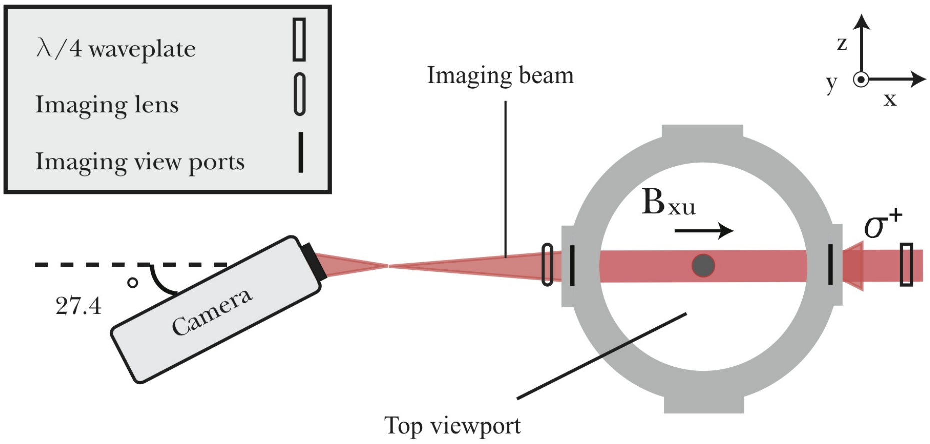

Figure 2.3: Schematic of the absorption-imaging system.

The profile of the beam is related to the atom density distribution as follows. When photons in the imaging beam are absorbed by atoms, the intensity $I_t(z, y)$ of the laser light becomes

$$I_\mathrm{t}(y, z) = I_0(y, z)e^{-D(y,z)} \tag{2.2}$$

according to Lambert Beer's law. In Equation (2.2), $I_0(y, z)$ is the profile of the probe beam. The optical density of the atoms is

$$D(y, z) = \sigma_\pi n(y, z), \tag{2.3}$$

where the column density profile of atoms is the integral of the local density $n_0(x, y, z)$ across the sample

$$n(y, z) = \int_{-\infty}^{\infty} n_0(x, y, z)dx. \tag{2.4}$$

In Equation (2.3), σ_π is the absorption cross section of the atoms

$$\sigma_\pi = \frac{3\lambda^2}{2\pi}\frac{1}{1 + I/I_\mathrm{sat} + (2\delta/\Gamma)^2}, \tag{2.5}$$

where λ is the incident light wavelength, I (2 mWcm^{-2} in our setup) is the intensity of the imaging beam, $\delta = \omega - \omega_r$ is the angular detuning from resonance of the scattered light, Γ is the natural linewidth of the transition and

$$I_{\text{sat}} = \frac{\pi}{3}\frac{hc\Gamma}{\lambda^3} \tag{2.6}$$

is the saturation intensity of the system. During images, the probe beam is pulsed for 35 μs leading to 1700 counts per pixel in a typical picture without absorption.

The signal captured by the CCD chip during an imaging pulse is

$$I_a(y,z) = I_0(y,z)e^{-D(y,z)} + I_b(y,z), \tag{2.7}$$

where $I_b(y,z)$ is the intensity of the optical background, non-imaging light reaching the CCD chip. There is always a possibility for a small portion of imaging light (scattered by the atoms) to be reflected on the viewport(s) of the vacuum chamber, and then to be incident onto the CCD chip. We found no effect of this light on the data obtained during the work being reported.

Now, by combining equations (2.7) and (2.3) we get for the column density

$$n(y,z) = -\frac{1}{\sigma_\pi}\ln\left(\frac{I_a(y,z) - I_b(y,z)}{I_0(y,z)}\right). \tag{2.8}$$

Assuming low optical density $\left[\frac{I_a(y,z)}{I_0(y,z)} >> \frac{I_b(y,z)}{I_0(y,z)}\right]$, which we found is valid for clouds of atoms at a few microkelvin but not for condensates as they are much denser, the density distribution of atoms is given by

$$n(y,z) = -\frac{1}{\sigma_\pi}\ln\left(\frac{I_a(y,z)}{I_0(y,z)}\right). \tag{2.9}$$

The method we used to extract the density profile of atom clouds from the images followed this principle. We took two pictures of the probe beam: one with the shadow of atoms and another one without it. Next, we divided the image with a shadow by the one without it, and took the logarithm of the resulting image. We obtained the number of atoms by summing the counts in each the pixel over the region covered by the atom cloud on the image and multiplying by the factor A/σ_π(228 in our case), giving

$$N = \sum_{\text{pixels}} \frac{A}{\sigma_\pi}\frac{I_a(y,z)}{I_b(y,z)}. \tag{2.10}$$

where A is the effective pixel area in the images.

2.3 Magneto-optical trapping

Magneto-optical trapping has become a standard technique to load cold atoms into optical or magnetic traps. Our microtrap is supplied with cold atoms by a MOT loaded directly from a thermal gas of Rb that is dispensed by pulses inside the vacuum chamber. Thus atoms are cooled down to temperatures that are suitable for magnetic trapping.

2.3.1 Laser cooling and trapping with a mirror MOT

The MOT enables us to cool hot atoms down to a few tens of microkelvin as can be achieved with optical molasses [7]. But additionally, the MOT also confines atoms in a small volume for seconds. It is for this reason that magneto-optical trapping has become the laser cooling technique preferred by researchers to load dipole or magnetic traps for a variety of experiments. There are a number of MOT versions used for different purposes, see [69, 70, 71, 72] for example. In our experiment we have an implementation of the mirror MOT [72]. This magneto-optical trapping technique is a convenient way to locate cold atoms near surfaces, as needed for experiments with atom chips.

The force that stops atoms in a MOT [73] is the same cooling force present in optical molasses. It is the scattering force of near-resonance light on atoms in a two energy-level scheme

$$F = \hbar k \frac{\Gamma}{2} \frac{I/I_{\mathrm{sat}}}{1 + I/I_{\mathrm{sat}} + 4(\delta/\Gamma)^2}, \tag{2.11}$$

where $k = 2\pi/\lambda$ is the wavenumber of the scattered light.

In three dimensional optical molasses, atoms are slowed with three pairs of counter propagating beams tuned to the red of the atomic transition. Temperatures of a few tens of microkelvin can be reached in each one of the spatial directions as a result of polarization-gradient cooling [8]. Similarly to an optical molasses arrangement, the construction of a MOT also requires a pair of counter propagating beams per cooling direction as illustrated in Figure 2.4 (a). The main difference is the addition of a magnetic quadrupole whose centre coincides with the centre of the volume in which the six laser beams overlap. A pair of coils with an anti-Helmholtz arrangement, also shown in Figure 2.4 (a), provides us with a magnetic quadrupole with spherical symmetry that is suitable for a MOT [73]. The arrows close to the centre of the MOT in Figure 2.4 (a) show the direction of the magnetic field produced by the coils along each axis.

A diagram of the cooling and trapping mechanism in one dimension, for the simple

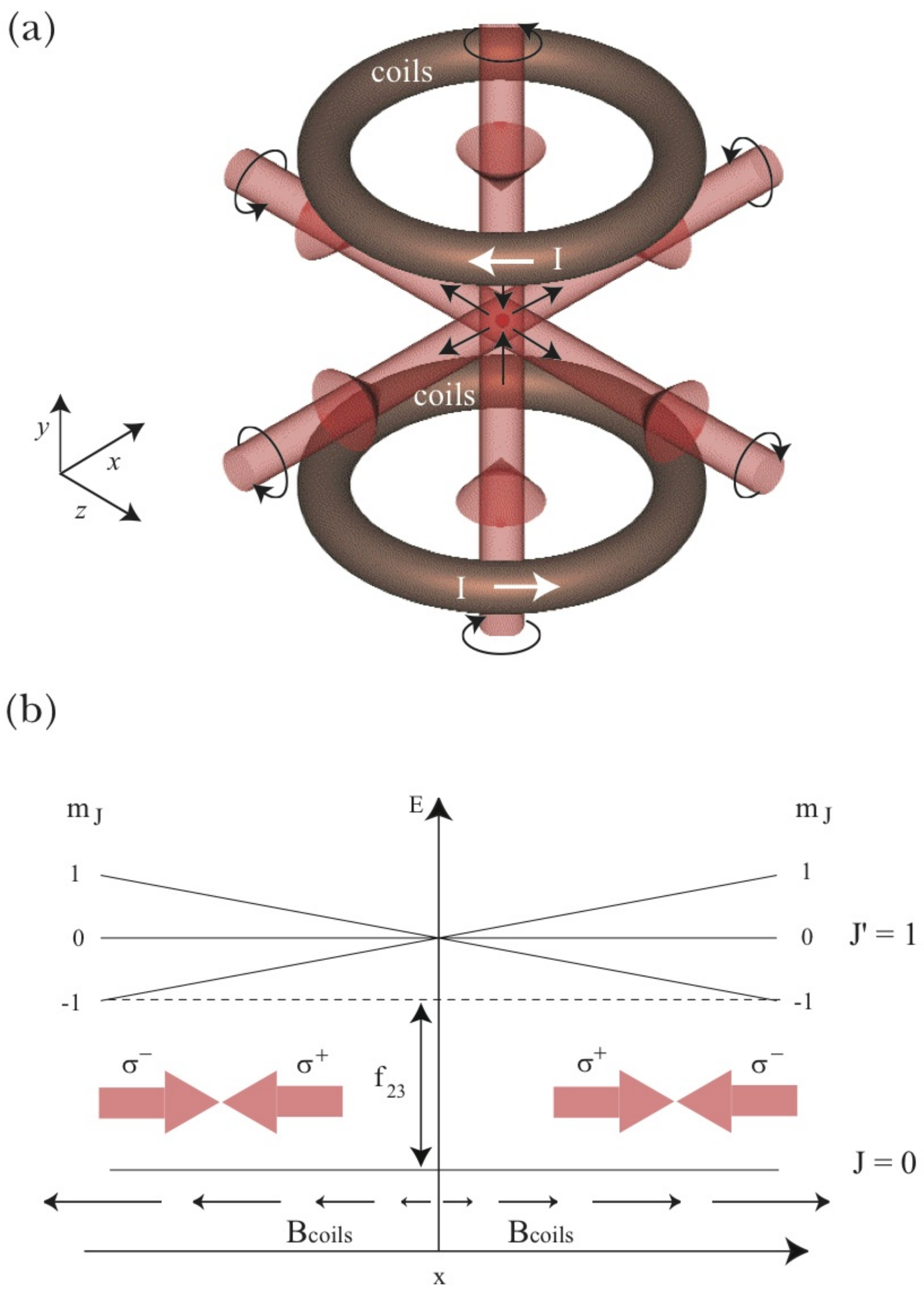

Figure 2.4: In a MOT, (a) atoms are cooled and trapped by a pair of counter propagating beams with opposite σ polarization in each of the three spatial dimensions. The reference for the polarization of light is the local magnetic field which is a spherical quadrupole provided by two anti-Heltmholtz coils. (b) is a diagram of the MOT system in the x-direction which has been arbitrarily chosen. All along x, atoms scatter preferably σ^--polarized light because the $m_F = -1$ sub-level is Zeeman shifted towards f_{23}, the trapping frequency. This produces an imbalance between the forces exerted by the lasers over the atoms, yielding an effective force pointing towards the centre everywhere.

case of a two level system of lower and upper levels with angular momentum $J = 0$ and $J' = 1$ respectively, is shown in Figure 2.4 (b). This one-dimensional diagram follows the x-direction of the MOT arrangement in Figure 2.4 (a), but the same mechanism also applies in the two other spatial dimensions. The field generated by the coils $\mathbf{B}_{\text{coils}} \propto (\frac{x}{2}, -y, \frac{z}{2})$ is zero at the centre of the arrangement, has opposite sign at each side of the quadrupole centre and varies in strength linearly with x. To achieve magneto-optical trapping, the counter propagating laser beams must have opposite circular polarization with respect the local magnetic field (the atoms' quantization axis) as schematized in Figure 2.4 (b). The light's polarization is σ^+, drives transitions to the $m_F = 1$ sub-level, if it moves anti-clockwise as one faces the vector of magnetic field. Conversely, the light is σ^--polarized and thus, populates the $m_F = -1$ sub-level if one sees the light's polarization vector rotating clockwise whilst facing the magnetic field vector. In both x and $-x$ regions of Figure 2.4 (b) the magnetic field shifts the $|0, 0\rangle \rightarrow |1, -1\rangle$ transition towards resonance with the laser frequency f_{23}, and the $|0, 0\rangle \rightarrow |1, 1\rangle$ transition is Zeeman-shifted away from it. Thus, all along the x-axis, atoms scatter preferably σ^- light which exerts a force towards the centre.

The atom-chip idea followed proposals of tight and strong magnetic traps for neutral atoms near surfaces [24, 74]. There was a consequent need for a method to provide cold atoms close to the surfaces so they could be loaded into the proposed traps. Although the MOT was a well established method for creating cold atom clouds for BEC experiments, the original design with six beams is not suitable near surfaces. In 1999, J. Reichel *et al.* [72] proposed and demonstrated the mirror MOT as a solution to form a system equivalent to the original MOT in a vicinity of a reflective surface. This requires just four laser beams to confine atoms in three dimensions, using the reflections from the surface. A diagram of the mirror MOT is displayed in Figure 2.5.

The mirror MOT is built by making a few changes to the configuration of the original MOT, shown in Figure 2.4 (a). We start by placing a mirror making a 45 ° angle with each one of two orthogonal laser beams forming the MOT, so their reflections overlap each others path as illustrated in Figure 2.5. The goal is to realise magneto-optical trapping in two dimensions with these two laser beams and their reflections. Thus the laser beams that were opposite to the (now) reflected beams in the original MOT are not longer required. Once the mirror has been located, the third trapping dimension is completed by the third pair of counter propagating beams of the MOT, parallel to the surface of the mirror and labelled as 'horizontal' beams in Figure 2.5.

In order to achieve magneto-optical trapping, the manner in which the mirror is placed must satisfy two further conditions. Firstly, the centre of the mirror has to be aligned with the centre of the '45°' beams. This is to maximize the volume in which the 45 ° beams, their reflections and the horizontal beams overlap. Secondly, the centre

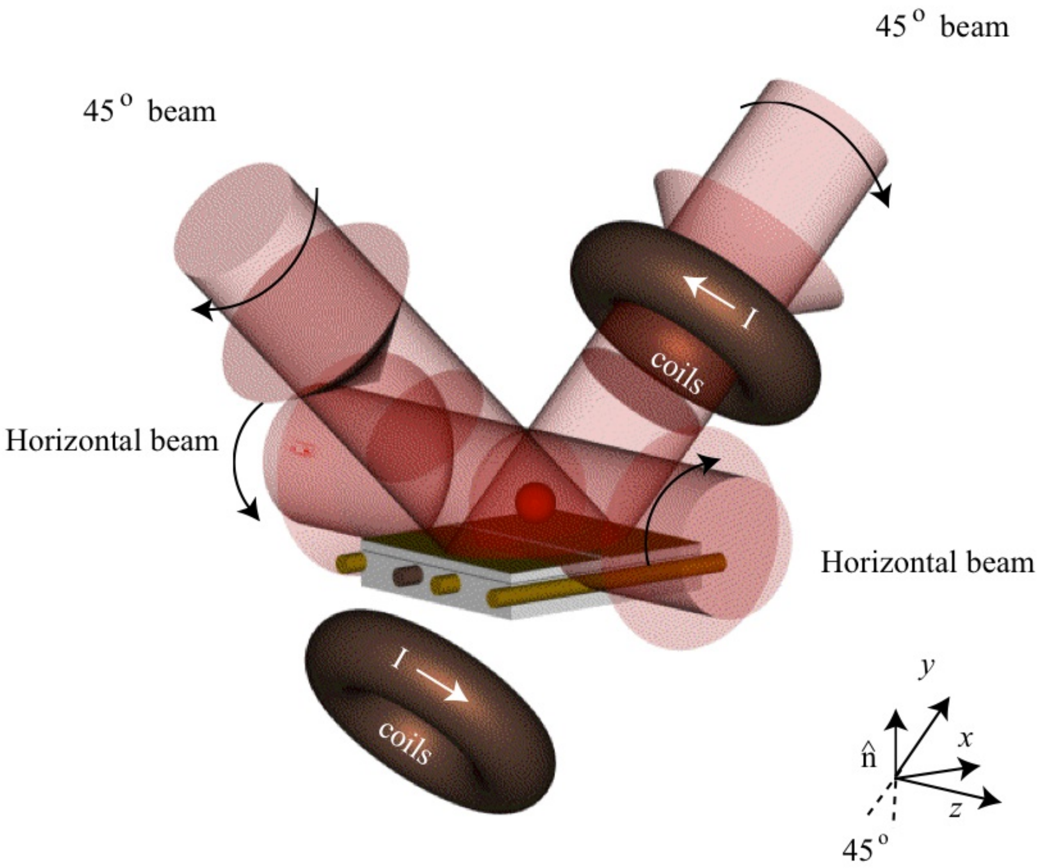

Figure 2.5: In a mirror MOT magneto-optical trapping in three dimensions is achieved with just two pairs of laser beams. Two beams of the original MOT are substituted by the reflection from a mirror of two laser beams at an incident angle of 45° to the its normal $\hat{n}$.

of the mirror must be placed at a few millimeters from the centre of the quadrupole created by the MOT coils, so the centre of the overlapping volume coincides with the centre of the MOT as illustrated in Figure 2.5.

Magneto-optical trapping is highly dependent on the orientation between the light polarization and the local magnetic field. A system equivalent to the MOT described in Figure 2.4 is achieved at a few millimeters above the mirror just if its reflecting surface reverses the helicity of the light. The reflecting surface also needs to have a high reflectance of light at the trapping frequency to prevent imbalance of the trapping forces.

The mirror MOT is a proved, efficient and simple method to cool and trap atoms from gases at high temperatures in a small volume near surfaces. Nowadays it is a magneto-optical trapping technique commonly used to load cold atoms into microtraps.

2.3.2 Our mirror MOT

A rubidium dispenser [75] located about 30 mm away from the centre of the magneto-optical trap supplies the atoms. It is kept warm by a standby current of 2 A, which is raised to 7 A for 12 s during each pulse of Rb dispensing. The base pressure of the vacuum chamber is lower than 10^{-11} torr, but increased to a maximum of 5×10^{-10} torr during the pulse. We hold the cold atoms with the MOT for 10 s before going to magnetic trapping which requires pressures of 10^{-10} torr (or below) to allow trapping times on the order of a minute. During these 22 s, the Ti:Sapphire frequency is 106 MHz red-detuned from f_{23} by the beatnote locking system, giving in this manner a detuning of -18 MHz to the MOT trapping light.

Magneto-optical trapping in three dimensions is achieved just in the region where all beams overlap and are appropriately aligned with the local magnetic field. The area in which the radiation force is acting on atoms is set by the cross-section of the laser beam. For larger cross-sections, the trapping velocity range is wider and loading of atoms into the MOT is more efficient. The maximum cross-sectional area of our trapping beams is fixed by the size of the reflecting surface which is 25 × 20 mm corresponding also to the size of the atom chip. To achieve this size on the cross section of the MOT beams, the MOT arms are expanded with 2.54 cm optics as shown in Figure 2.2. The total power of the trapping beam is 170 mW after the AOM setting the trapping light detuning. This corresponds to a total intensity of 80 mWcm^{-2} which is evenly split in the four MOT beams delivered into the experiment. Suitable circular polarization conditions for the mirror MOT geometry are set by a $\lambda/4$ waveplate placed on the path of each MOT beam just before it is delivered into the vacuum chamber.

The MOT-coil formers have internal and external diameters of 22.3 and 30.3 mm respectively and their width is 7.9 mm. This gives enough space for 81 turns of Kapton insulated wire inside the vacuum. The two MOT coils are 5 cm apart from each other, and are orientated at 45° with respect to the y-axis following an anti-Helmholtz fashion as illustrated in Figure 2.5. During experiments, we run a current of 1.5 A through the MOT coils. This current generates a field gradient of about 0.18 Tm^{-1} along the axis of the MOT coils, paralleled to y in Figure 2.5. The centre of the quadrupole is located 3.8 mm from the surface of the atom chip. This distance was adjusted for best atom-collection efficiency using the field B_{xu}.

The picture displayed in Figure 2.6 is an image of the fluorescence from atoms trapped in the MOT. Typical atom clouds have 10^8 atoms with a temperature of 50 μK. All the temperatures of magneto-optically trapped atoms reported in this Thesis are measured with ballistic expansion. This method is explained in Appendix D. The

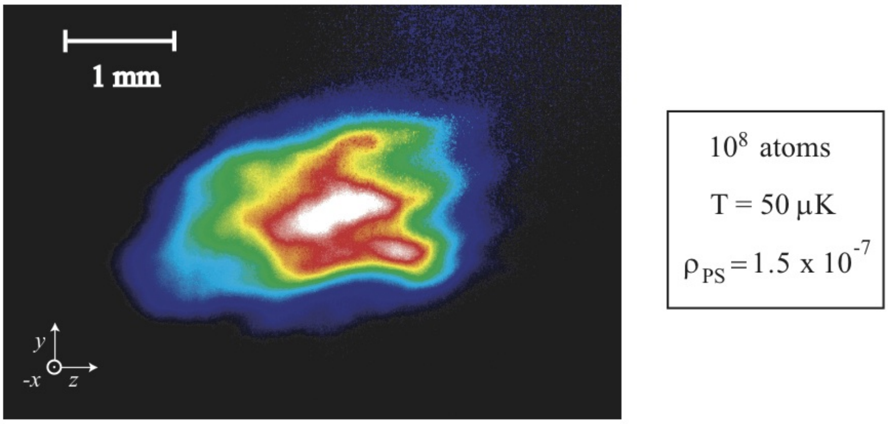

Figure 2.6: Image of the florescence from Rb atoms in the mirror MOT.

phase-space density at the centre of the MOT, calculated by using the peak density

$$n_0 = \frac{N}{(2\pi)^{3/2}\sigma_x\sigma_y\sigma_z} \tag{2.12}$$

of the Gaussian distribution in Equation (2.1), is $\rho_{\mathrm{PS}} = 1.5 \times 10^{-7}$. In Equation (2.12) N is the total atom number, and $\sigma_{x,y,z}$ is the radius of the Gaussian distribution in each spatial direction. As shown in Figure 2.6, we image atom clouds in the yz-plane. To obtain this number of ρ_{PS}, I assumed $\sigma_x = \sigma_y$ (567 μm in the case of the MOT shown in Figure 2.6, where $\sigma_z = 759$ μm).

2.3.3 Temperature in laser cooled atoms

In thermodynamics, the temperature is a quantity that characterizes the equilibrium state of an ensemble of particles in contact with a thermal bath. Atoms in a MOT are not in thermal equilibrium with a reservoir however, it still makes sense to define the temperature of laser-cooled atoms as

$$T \equiv \frac{\langle \epsilon_k \rangle}{k_B}, \tag{2.13}$$

to label a typical state with average kinetic energy $\langle \epsilon_k \rangle = \frac{1}{2} m \langle v \rangle^2$, where $\langle v \rangle$ is the average velocity of atoms in a chosen direction. This re-definition of temperature makes sense because the steady solution of the Focker-Planck equation, describing a system of laser cooled atoms has a Gaussian momentum distribution. The solution of the equation has the form of a Maxwell-Boltzmann distribution with temperature $k_B T = D/\beta$. D is a diffusion coefficient which describes the random nature of light scattering in the system and β is the damping coefficient on the velocity-dependent force acting over atoms due to the pressure of light.

Due to this result, we can label distributions of laser cooled atoms with a temperature associated to their average kinetic energy. For magnetically trapped atoms this definition of temperature is also valid with a different justification (see Section 4.2.1).

2.4 An on-chip Ioffe-Pritchard trap

The Ioffe-type magnetic trap was originally used for research on plasma physics. In 1983 it was proposed for magnetic trapping of neutral atoms by David E. Pritchard [76]. Thereafter, in the atom-optics context, this trap is known as a Ioffe-Pritchard trap. It is now widely employed in BEC experiments. The atom chip we used to investigate decoherence-surface effects was designed to create a Ioffe-Pritchard trap based on a single current carrying wire and a bias field.

2.4.1 Principles of the Ioffe-Pritchard trap

Magnetic trapping of neutral atoms is based on the interaction between their magnetic dipole moment and the local magnetic field. The energy of this interaction is given by Equation (1.2) which, for an atom with internal-energy state $\mid I\ J\ F\ m_F\rangle$, can be written as

$$U = \mu_B g_F m_F B, \tag{2.14}$$

where μ_B is the Bohr magneton, g_F is the g-factor of the total-angular momentum F, and B is the magnitude of the local magnetic field $\mathbf{B}$. Atoms having positive $g_F m_F$ are trapped in minima of the magnetic field strength. Since a static magnetic field has no maxima, [77] atoms with negative $g_F m_F$ cannot be similarly trapped. The trapping force is given by the gradient of Equation (2.14)

$$\mathbf{F}_{\text{trap}} = -\mu_B g_F m_F \boldsymbol{\nabla} B. \tag{2.15}$$

One configuration of the Ioffe-Pritchard trap is created by combining the fields of four current carrying rods and two coils, see Figure 2.7 (a). The four rods are equidistant and carry a current I in alternating order to make a long, transverse quadrupole field with zero magnetic field on the centre line. This line of zero field is suitable for guiding low field seeking atoms [78]. However, the atoms need to keep their m_F quantization if they are to remain trapped. A Majorana spin flip [79, 80] is likely to happen near the axis of the quadrupole because the atomic spins have little field to follow in this region. This would lead to relaxation of the trapped states and hence, atom loss from the trap.

In the Ioffe-Pritchard trap design, this problem is solved by adding a field along the axis [z in Figure 2.7 (a)] by means of the two coils. In Figure 2.7 (a) these have

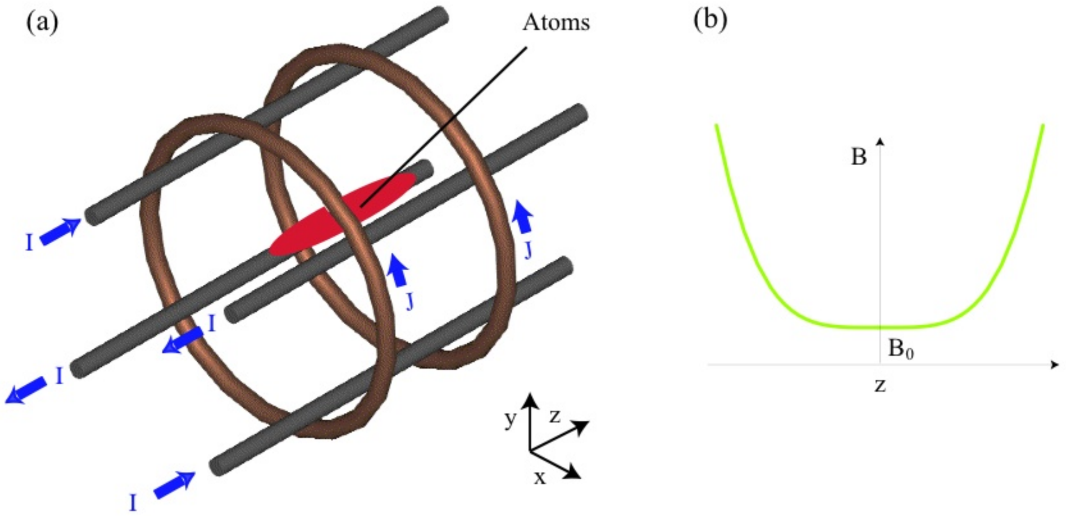

Figure 2.7: Schematic of a Ioffe-Pritchard trap (a). A long quadrupole is created by running a current I through four equidistant rods. This creates a magnetic guide with cylindrical symmetry whose axis (parallel to z) lays along the centre of the four rods. The pair of coils running a current J provide a field in the z-direction that offsets the centre of the guiding potential by B_0 and ends the guide in the axial direction (b). Thus the atom clouds confined with a Ioffe-Pritchard trap have an elongated shape, similar to a cigar.

the same radius R, their centers are separated by $2R$ along z and both coils conduct a current J that is flowing in the same direction. The generic form of the field strength given by these coils (with Helmholtz geometry) is shown by Figure 2.7 (b). Near $z = 0$, the field B_0 from the coils prevents Majorana spin flips. Additionally, the ends of the potential shown in Figure 2.7 (b), constrain the confinement of atoms in the axial direction of the elongated magnetic guide created by the current carrying rods. This gives a cigar shape to atom clouds confined in Ioffe-Pritchard traps.

2.4.2 A micro-manufacturable Ioffe-Pritchard trap

There are several different configurations of current carrying wires and bias fields [25, 29] that can produce a Ioffe-Pritchard trap. Here I explain the version in which a long magnetic guide is created by a single-guide wire plus a bias field. The waveguide is closed at its ends by two transverse current carrying wires, completing in this manner the geometry of the Ioffe-Pritchard trap. This is the microtrap design that we used for measurements of surface effects.

Radial confinement

Consider the system described in Figure 1.1 (a): a current-carrying wire whose axis is parallel to z and a bias field B_x pointing towards $-x$. With this combination of magnetic fields, a guide for atoms is created along the line in which B_x cancels out with the circular field of the wire, at x_0=0, y_0=$\frac{\mu_o I}{2\pi B_{bias}}$ in Figure 1.1 (b).

The resulting field is a long quadrupole, equivalent to the field created by the four equidistant rods mentioned in Section 2.4.1. In the frame of reference of Figure 1.1 (and 2.7), this field is given by

$$\mathbf{B}(x, y, z) = b(x\hat{\mathbf{e}}_x, -y\hat{\mathbf{e}}_y, 0) \tag{2.16}$$

near the line x_0, y_0; $b = \frac{2\mu_0 I}{\pi D^2}$, where D is the distance between rods [4]. The field magnitude, and hence the magnetic interaction potential U [in Equation (2.14)] associated to $\mathbf{B}(x, y, z)$, is proportional to its gradient b,

$$U(r) \propto |\mathbf{B}(x, y, z)| = b\sqrt{x^2 + y^2} = br. \tag{2.17}$$

Atoms with quantum numbers $g_F m_F > 0$ feel a force towards the quadrupole axis given by

$$\mathbf{F} = -\mu_B g_F m_F b\hat{\mathbf{e}}_r. \tag{2.18}$$

Thus this potential is indeed, a guide for atoms with cylindrical symmetry.

Equation (2.17) states that the magnetic interaction potential varies linearly along both x and y axes within the vicinity of x_0, y_0. This is illustrated by the green curves with sharp-V minima in Figure 2.8, plotting the radial potential through the centre of a waveguide created by 7.94 A through the guide wire and 1 mT of bias field. The green curves in (a) and (b) of Figure 2.8 correspond to the axial potential along x and y respectively. This potential was calculated with parameters that we use to create magnetic traps loaded from the mirror-MOT at about 1.3 mm from the surface of the guide wire, see Section 2.4.3.

The potential depth is the energy that an atom requires in order to be expelled from confinement. In units of magnetic field, the depth u_r of the waveguide is equal to the bias field B_x, 1 mT in our case. Referring to potential depths in units of temperature is sometimes more illustrative. The conversion is done by equating the potential energy gained by the atom due to the magnetic field to its equivalent in thermal energy, $\mu_B g_F m_F B = k_B T$. For ^{87}Rb in the state $|F = 2, m_F = 2\rangle$ ($g_F m_F$=1), 1 mT= 670μK. Hence our guide is 670 μK deep in the radial direction.

Now let us offset the waveguide centre by a field $B_0\hat{\mathbf{e}}_z$, as is done in the Ioffe-Pritchard configuration. Here B_0 also has the effect of smoothing the potential across the centre of the waveguide; the V-shape minima are changed to continuous curves. The blue-dotted curves in figures 2.8 (a) and (b) show the potential along x and y

---

[4] In the quadrupole approximation $b = \frac{2\mu_0 I}{\pi R^2}$ [26], where R is the radius of the circle containing the position of each rod's centre. Because the rods are equidistant we can make $R = D$.

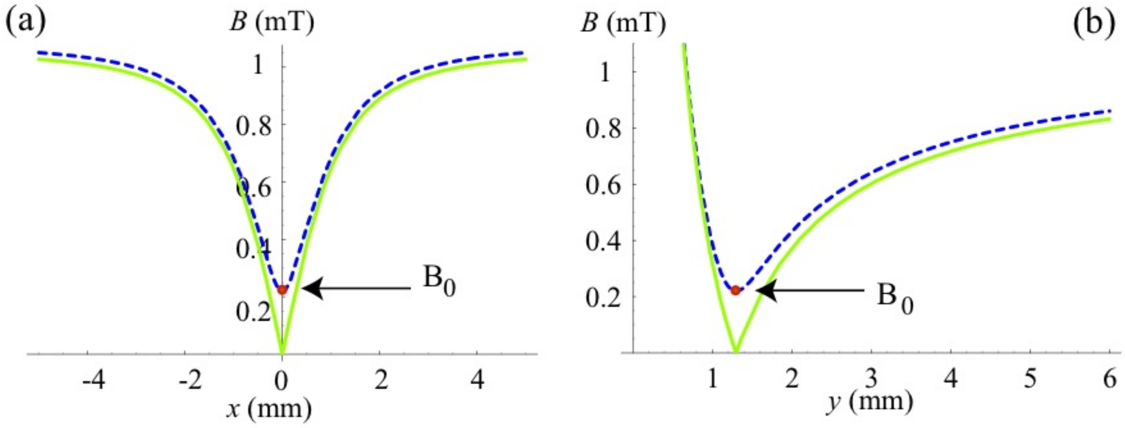

Figure 2.8: Magnetic interaction potential (times $1/\mu_B$) of a waveguide created by a guide wire and a bias field. The green curves are the cross sections of the guiding potential along x (a) and y (b) passing through the centre of the waveguide created by guiding current of 7.94 A and a bias field $B_x = 1$ mT. The blue-dotted curves represent the potential along x (a) and y (b) with the inclusion of an offset field $B_0 = 0.22$ mT along z.

including an offset field $B_0 = 0.22$ mT which is a typical experimental value in our setup, see Section 2.4.3.

With the offset field, the magnetic interaction potential is proportional to

$$|\mathbf{B}(x, y, z)| = \sqrt{(br)^2 + B_0^2} \tag{2.19}$$

which, by taking the first two terms of its binomial expansion, can be written as

$$|\mathbf{B}(x, y, z)| = \frac{(br)^2}{2B_0} + B_0. \tag{2.20}$$

Thus, according with Equation (2.14), the guiding potential is

$$U(r) = \frac{1}{2} m\omega_r^2 r^2 + U_0 \tag{2.21}$$

close to its centre. This is the potential of a harmonic oscillator with angular frequency

$$\omega_r = \sqrt{\frac{g_F \mu_B m_F b^2}{m B_0}}, \tag{2.22}$$

where m is the mass of atoms. In Equation (2.21), $U_0 = \mu_B g_F m_F B_0$ is the potential energy due to the field at the bottom of the trap. Equation (2.22) states that the frequency of the transverse oscillations in the microtrap is proportional to the field gradient, which is in turn proportional to the trapping strength given by Equation (2.15).

The adiabatic condition ensures spin flips are suppressed. It requires the magnetic field in the frame of reference of the atoms to change slowly compared with the Larmor frequency of spin precession around the magnetic field. For the transverse oscillations of atoms inside the magnetic trap, this implies that

$$\omega_r << \omega_L \tag{2.23}$$

is required. In Inequality (2.23), $\omega_L = \frac{1}{\hbar} g_F m_F \mu_B B_0$ is the Larmor frequency at the bottom of the trap. By plugging Equation (2.22) into inequality (2.23) we see that

$$B_0 > \left(\frac{\hbar^2 b^2}{\mu_B g_F m_F m} \right)^{1/3} \tag{2.24}$$

is needed in order to satisfy the adiabatic condition. From Inequality (2.24) we can estimate the minimum offset field required to preserve adiabaticity in our microtrap. Typical magnetic traps loaded from the mirror MOT have a field gradient of 0.65 T m^{-1}. Hence B_0 has to be greater than 152 nT when loading the magnetic trap.

Axial confinement

In this configuration of microtrap, axial confinement is achieved by running a current through two transverse wires lying at a distance h underneath the guide wire as illustrated in Figure 2.9. The long waveguide created by the guide wire and bias field B_x lays above the guide wire, with its axis parallel to z on Figure 2.9 (b). Both transverse (or 'end') wires carry a current J in direction -x. The current J produces a field that reaches its minimum at the midpoint between end wires and its maximum at the plane of each end wire along z. This potential is plotted in Figure 2.9 (a) for 15 A through the end wires (the current that we normally run through the end wires during experiments) at 1.3 mm from the surface of the guide wire. The difference of magnetic interaction potentials between the ends of the trap and its centre, is the axial trap depth of the microtrap: $u_a = |B_{\text{end}}^{\text{max}} - B_{\text{end}}(x_0, y_0, z_0 = 0)|$.

The potential that atoms feel at the centre of the trap is harmonic along the z-direction without the need of adding any other extra field. In the axial direction, the harmonic motion of the atoms has frequency

$$\omega_a = \sqrt{\frac{g_F \mu_B m_F}{m} \frac{d^2 B}{d^2 z}}, \tag{2.25}$$

where $\frac{d^2 B}{dz^2}$ is the axial curvature of the potential at the centre of the trap x_0, y_0, z_0.

The offset field B_0 to prevent Majorana loss is determined by the z-component of the trapping field, whose only contributor so far is the field of the end wires. If B_0 is a substantial fraction of B_x, it may cause the microtrap to be inconveniently shallow in

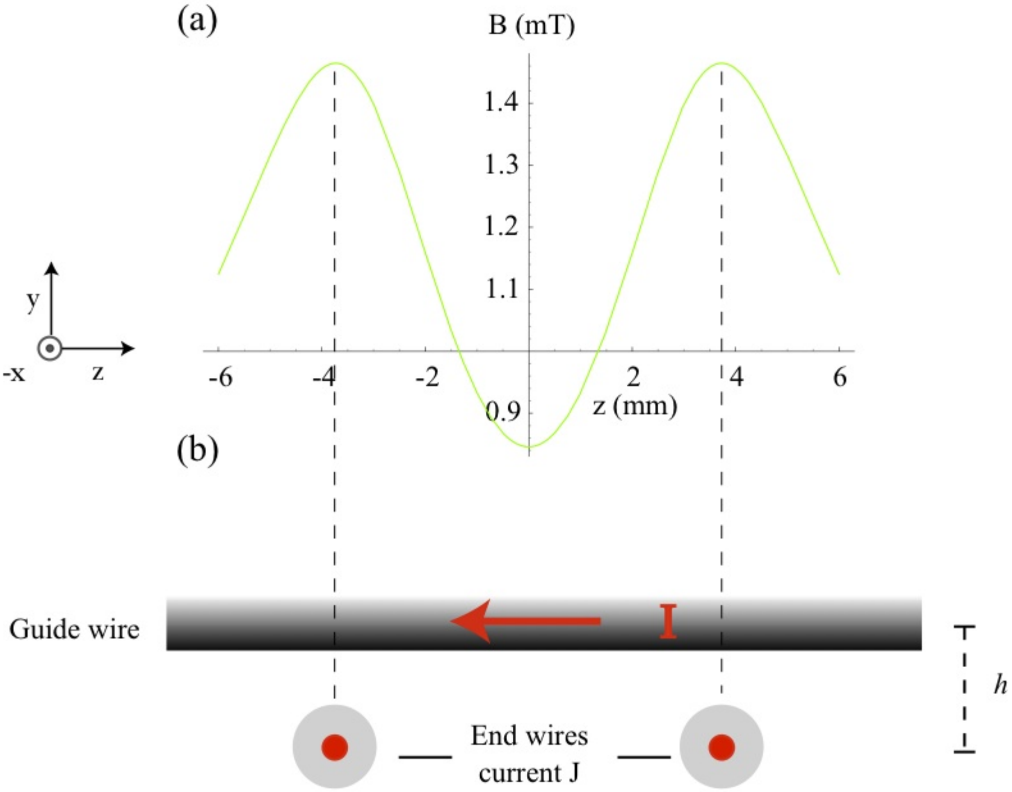

Figure 2.9: In this configuration of Ioffe-Pritchard microtrap, a waveguide created by the guide wire and bias field is closed with the field of two current carrying wires transversally located underneath the guide wire (b). (a) shows the potential produced by 15 A through the end wires at 1.3 mm from the surface of the guide wire. These parameters are chosen according with real experimental conditions, see Section 2.4.3.

the radial direction. It is possible to increase the trap depth in both radial and axial directions by partially cancelling the field of the end wires with an additional bias field in the z-direction, the z-cancelling field B_z. With this additional field, the offset field is $B_0 = |B_{\text{end}}(z = 0) - B_z|$.

To summarize, cigar-shaped atom clouds are held in a Ioffe-Pritchard microtrap formed by closing a long waveguide created by the guide wire and a bias field with the field of two transverse wires. The offset field B_0, the field of the end wires plus B_z, prevents atom loss at the centre of the trap.

2.4.3 Our microtrap

A diagram of our atom chip with a single-guide wire is shown in Figure 2.10. The guide wire of this atom chip has a diameter of 500 μm. This wire is large compared with wires fabricated with lithography techniques, see for example [81, 82] or Chapter 5, in more recent atom chips. It was not fabricated specially for atom chips. Also, its cylindrical shape contrasts with the planar geometry of wires commonly now used on other atom chips. In this atom chip, the guide wire is placed between two cover-slips, coated with 60 nm of gold to reflect 780 nm light to create a mirror MOT, see Figure 2.10. The guide wire and the cover slips sit on a glass substrate containing the four end wires that have a 800 μm diameter.

To load this Ioffe-Pritchard microtrap, we run 7.94 A through the guide wire and apply a bias field of 1 mT with a pair of external coils. This creates a cylindric waveguide for neutral atoms at a distance $d = 1.3$ mm above[5] the surface of the guide wire. As can be seen in Figure 2.10, our atom chip has four instead of two end wires. The four are connected in series, so that the current J flows in opposite directions in the inner and outer wires, as shown in Figure 2.10. The outer end wires were included in this atom chip with the intention to further increase the axial trap depth as discussed in [37]. Now we know however, that in fact running the current also through the outer end wires (as shown in Figure 2.10) does not help to increase the trap depth. The inner end wires alone, carrying 15 A, give an axial depth of 0.62 mT at $d = 1.3$ mm, see Figure 2.9. We added -0.63 mT of z-uniform field with a pair of external coils which, combined with the field of the end wires, gives a 0.22 mT offset field B_0, increasing the axial depth of the magnetic trap to 0.76 mT. With this B_0, the radial depth of our microtrap is $|B_x - B_0| = 0.78$ mT.

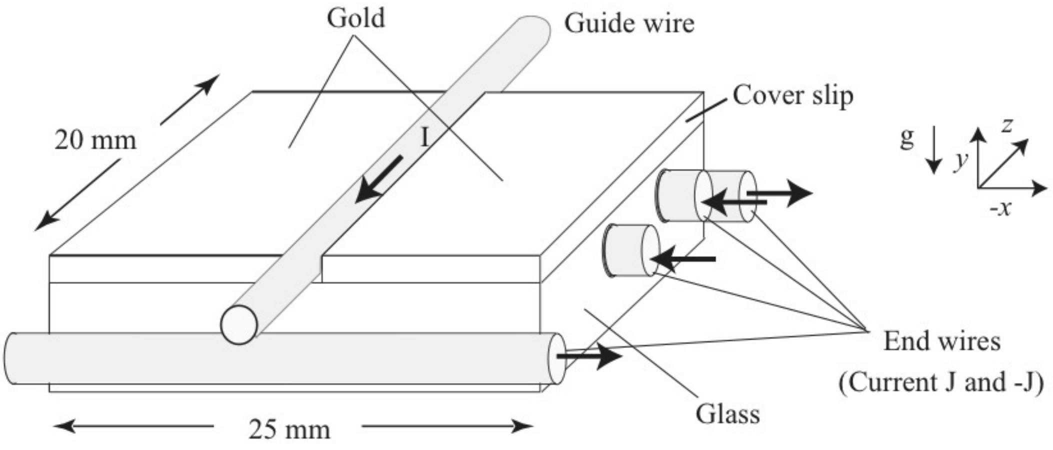

Figure 2.10: Diagram of our atom chip with a single guide wire and four end wires.

2.5 Loading the microtrap

Once atoms are laser cooled and trapped by the mirror MOT, the next step is to transfer them to the microtrap described in Section 2.4.2. To do this efficiently, the magnetic trap potential should resemble that of the MOT in shape, size and position.

---

[5] This atom chip is mounted 'upwards'– meaning that the atom-chip is orientated so gravity points towards -y as indicated in Figure 2.10.

2.5.1 The compressed MOT stage

With this in mind, we increase the aspect ratio of the mirror MOT before attempting to load the atoms into the microtrap. This is done during the last 60 ms of magneto-optical trapping by adding to the normal MOT quadrupole the long waveguide field due to the guide wire plus the bias field B_x. As described in Section 2.3.2, the mirror MOT is loaded in dispenser pulses of 12 s followed by a waiting time of 10 s for vacuum recovery. After these 22 s, the long magnetic quadrupole of the waveguide is gradually switched on, and the spherical quadrupole created by the MOT coils is weakened in a sharp step.

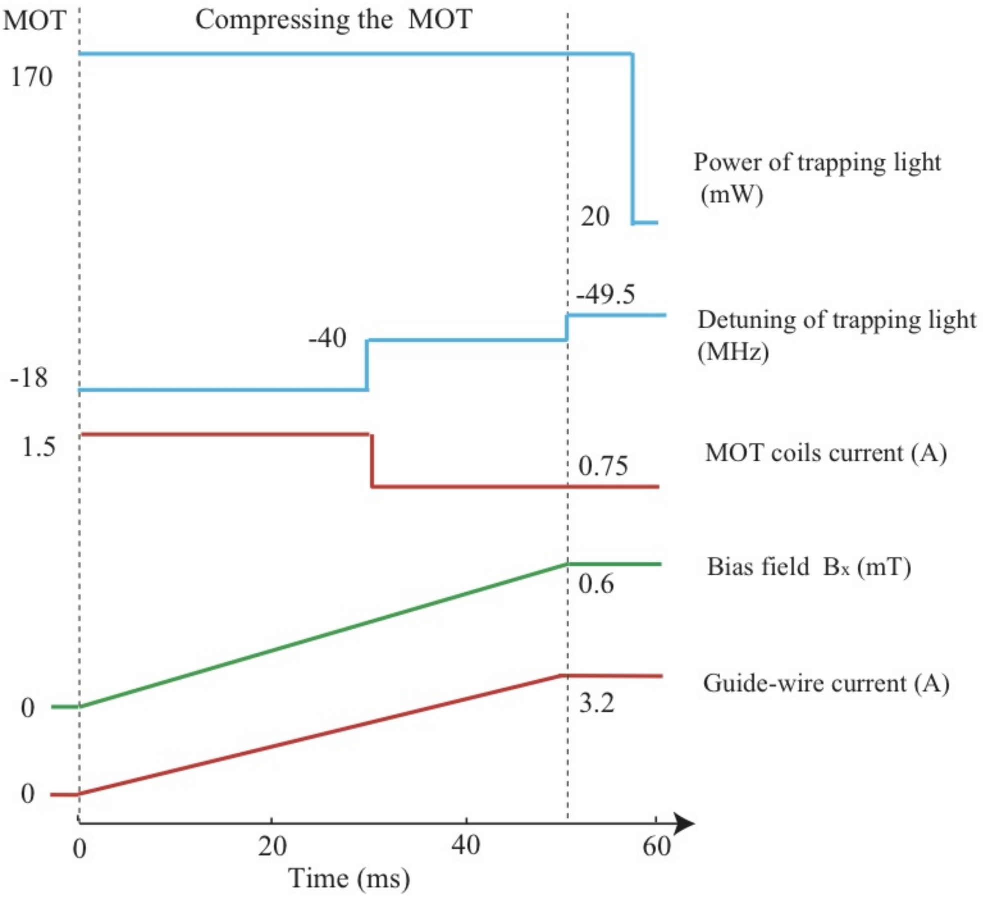

Figure 2.11: Experimental parameters changed during the compression of the MOT, process that lasts for 60 ms.

All the variations of the experimental parameters to compress the MOT are shown in Figure 2.11. The waveguide quadrupole is produced by linearly ramping both the current of the guide wire and the bias field over 50 ms. The guide-wire current is ramped from 0 to 3.3 A; while the bias field is ramped from 0 to 0.6 mT. After these 50 ms, the current of the guide wire and B_x where kept constant for 10 ms more, see Figure 2.11.

In parallel with switching on the waveguide quadrupole, during these 60 ms, several parameters of the MOT were also changed as illustrated in Figure 2.11. The field of the MOT coils is reduced to 50 % by switching the current through its coils. This is levelled from 1.5 A to 0.75 A in a sharp step after the first 30 ms of this MOT compression and then, held constant for the remaining 30 ms. The detuning of the trapping light is increased and its power decreased in the last few milliseconds of this compression to diminish multiple scattering of the trapping light by atoms. This causes atom heating as well as incompressibility of the atom cloud. The trapping-light detuning is changed twice during the compressed MOT stage. It is first stepped from -18 MHz to -40 MHz after 30 ms and to -49.5 MHz after 50 ms. The total power of the trapping light had a single change from 170 mW to 20 mW during the last 2 ms of the 60 ms of MOT, see Figure 2.11.

Once compressed the MOT is located 1.3 mm from the surface of the guide wire as shown in Figure 2.12. Compressing the MOT has the effect of slightly heating atoms up to 85 μK. There is no atom loss during this process, and the phase-space density is increased to $\rho_{\mathrm{PS}} = 1.7 \times 10^{-6}$. This is also the peak phase-space density given by equations (2.1) and (2.12). The atom cloud shown in Figure 2.12 has $\sigma_y = 302$ μm and $\sigma_z = 878$ μm.

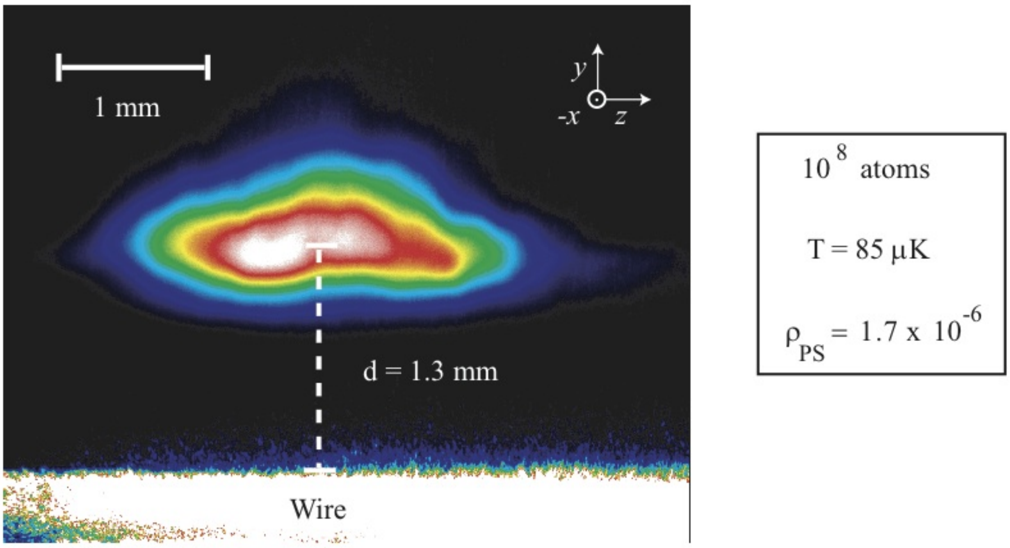

Figure 2.12: Fluorescence image of the compressed MOT. During this stage, the centre of the atom cloud is pulled to 1.3 mm from the surface of the guide wire.

2.5.2 Optical pumping and atom transfer

Once the MOT is compressed, the waveguide fields, MOT coils and the trapping light are switched off. Re-pump light is left on as required for optical pumping. Then the optical-pumping beam is pulsed on for 250 μs. This beam is directed along-z, parallel to the guide wire and is circularly polarized along $+z$. The quantization field, also along $+z$, is a combination of the field generated by the end wires running 15 A and the applied uniform field B_z.

Following optical pumping, the re-pump light is also switched off and all the fields of the magnetic trap are switched on. Now the current of the guide wire is directly stepped from 0 to 7.94 A, the bias field from 0 to 1 mT and 15 A are run through the end wires, as described in Section 2.4.3. There are 2 ms left between switching off the compressed MOT fields for optical pumping and turning on the magnetic trap. Figure 2.13 shows an absorption image of the atoms loaded in the magnetic trap. One order of magnitude is lost in atom number while loading the magnetic trap from the compressed MOT after optical pumping; typical magnetic traps confined 1.2 $\times 10^7$ atoms on this atom chip. The temperature inside the magnetic trap is close to the temperature in the compressed MOT – typically 83 μK [6] – suggesting that the atom transfer is well optimized. The atom loss is attributed to the shallowness of the magnetic trap. The peak phase-space density of the loaded magnetic trap is typically $\rho_{\mathrm{PS}} = 1.7 \times 10^{-8}$. Even after optimizing the loading process, the atom-cloud oscillates in the trap. The radial and axial trap frequencies were measured from this motion: $\omega_r = 2\pi\times$ 45 Hz and $\omega_a = 2\pi\times$ 17 Hz.

A parameter that arises here due to its importance in the final evaporative cooling stage, is the the elastic collision rate

$$k_{el} \equiv n\sigma_{\mathrm{el}}\langle v_{\mathrm{R}}\rangle, \tag{2.26}$$

where n is the atom density, $\langle v_{\mathrm{R}}\rangle$ is the mean relative velocity between atoms which is well estimated by the rms velocity $v_{\mathrm{rms}} = \sqrt{\frac{6k_BT}{m}}$, and σ_{el} is the elastic-scattering cross section assumed constant at $\sigma_{\mathrm{el}} = 8\pi a^2 = 7.7 \times 10^{-16}$ m, as appropriate for Rb^{87} in the $|2,2\rangle$ state at temperatures lower than 300 μK [65]. The scattering length is $a = (104.5 \pm 2.5)a_0$, where $a_0 = 5.3 \times 10^{-11}$ m.

Because the atom distribution is not homogeneous but rather Gaussian, k_{el} needs to be averaged:

$$\langle k_{el}\rangle = \langle n\rangle\sigma_{\mathrm{el}}\langle v_{\mathrm{R}}\rangle. \tag{2.27}$$

In Equation (2.27), $\langle n\rangle = \frac{n_0}{2\sqrt{2}}$ is the atom density averaged over the Gaussian distribution ($n_0 = 1.9 \times 10^{15}$ m^{-3} in typical magnetic traps). By plugging the peak density n_0 given by Equation (2.12) into Equation (2.27), we obtain

$$\langle k_{el}\rangle = \frac{N}{2(2\pi)^{3/2}}\sqrt{\frac{3k_BT}{m}}\frac{\sigma_{\mathrm{el}}}{\sigma_x\sigma_y\sigma_z} = \frac{3N}{2(2\pi)^{3/2}}\frac{m\omega_r^2\omega_a\sigma_{\mathrm{el}}}{k_BT}, \tag{2.28}$$

---

[6] The temperature of atoms trapped by magnetic traps is measured from a single absorption image. This is possible because we have previous knowledge of the trap frequency, see Section 4.2.1 for the detailed explanation of these measurements.

where the indices y and z are changed to r and a regarding the radial and axial directions of our trap.

Calculated with Equation (2.28), the elastic collision rate of the magnetic trap shown in Figure 2.13 is 0.95 s^{-1}. As explained in Section 2.7, evaporative cooling is more efficient with higher collision rates. This parameter has to be increased so BEC can be reached by evaporating the hottest atoms from the microtrap.

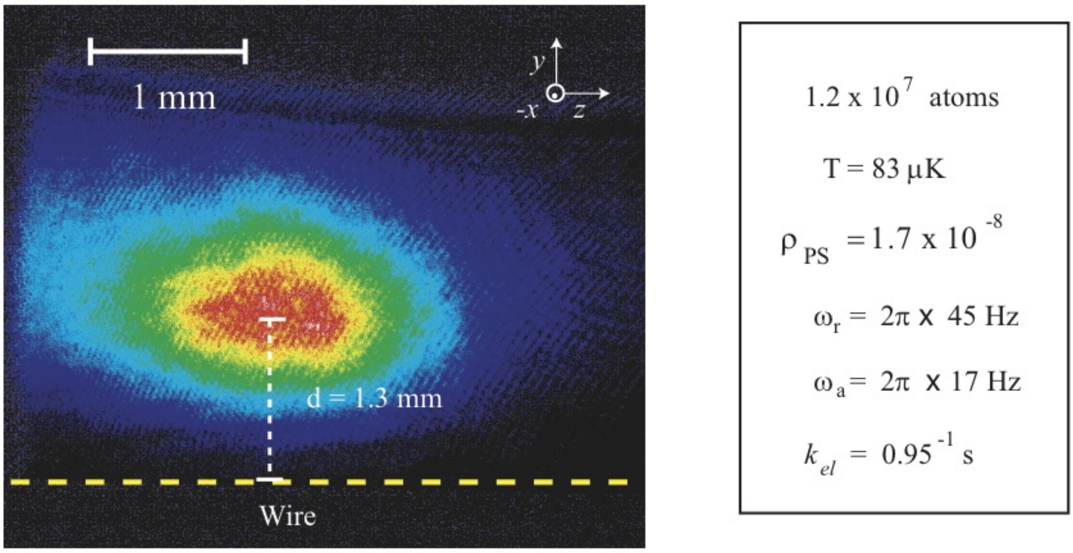

Figure 2.13: Absorption image and selected parameters of typical atom clouds loaded into the microtrap.

2.6 Compressing the magnetic trap

One manner to boost the collision rate is by increasing the peak density n_0 of the atom cloud. This can be done by raising the trapping force [Equation (2.15)] which is done with an increment of the field gradient across the centre of the magnetic trap. Among the many advantages of microtraps, one is that high field gradients are achievable without large power dissipation. In order to increase the collision rate in our microtrap, we pulled atoms towards the guide-wire surface by decreasing the guiding current and simultaneously increasing the bias field B_x.

The magnetic trap compression is carried out in 500 ms. A diagram of this process is shown in Figure 2.14. Three trapping fields are linearly ramped: the guide-wire current from 7.94 to 6.9 A, the bias field from 1.2 to 2.9 mT and z-cancelling field from 0.63 to 1.1 mT. The new guiding parameters, the guide-wire current and B_x, brought the waveguide centre to d = 225 μm from the wire's surface. Figure 2.15 shows an absorption image of atoms inside the magnetic trap once compressed.

With the final parameters of the magnetic trap compression, the offset field B_0 is

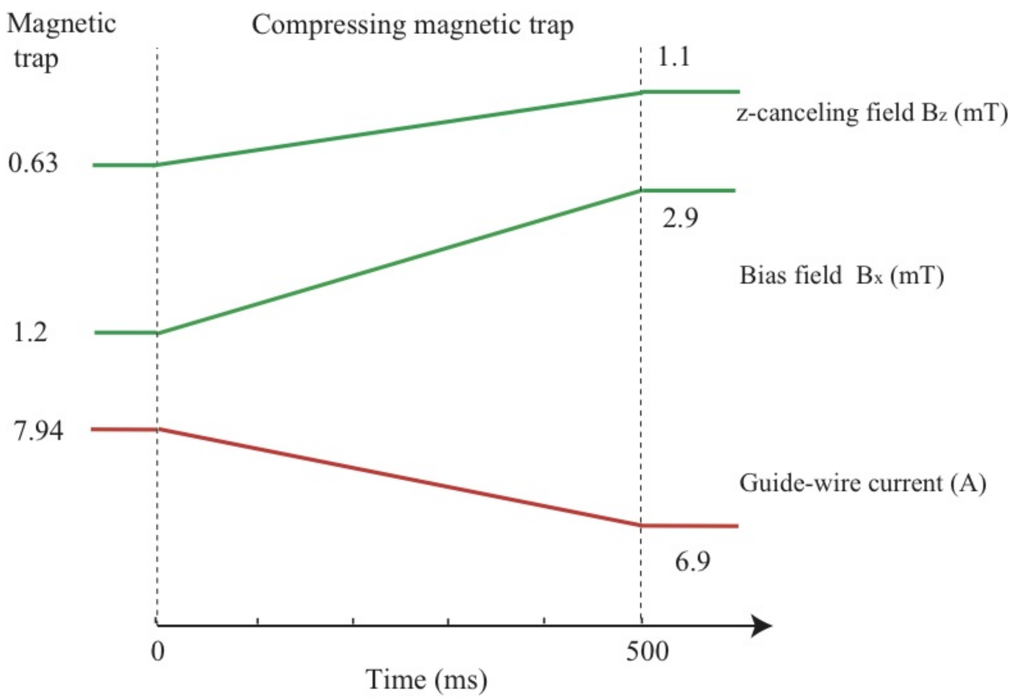

Figure 2.14: Sequence of field changes when compressing the magnetic trap.

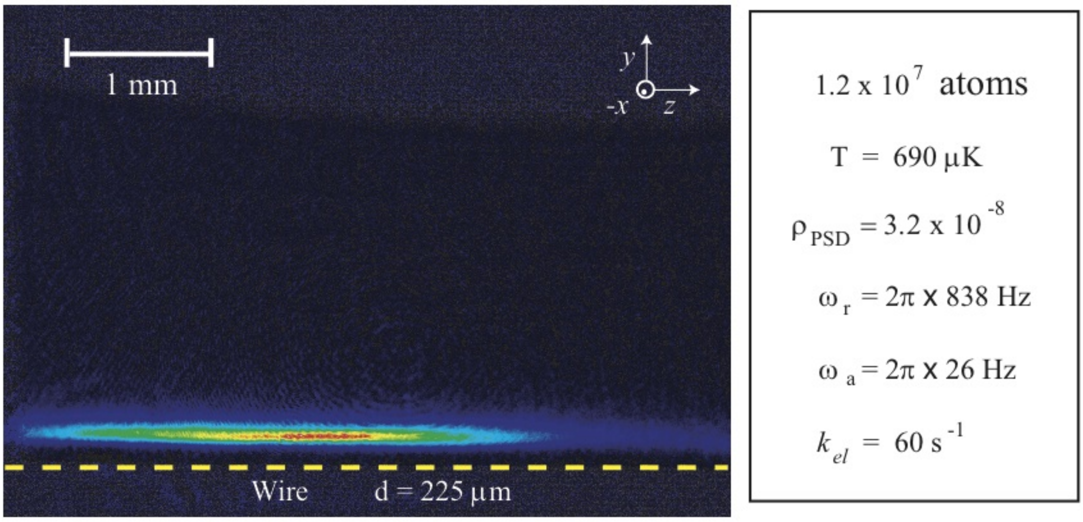

Figure 2.15: Absorbtion image and selected parameters compressed microtrap.

reduced to 0.05 mT. Consequently the trap depths were raised to 2.85 mT in the radial direction and to about 0.77 mT in the axial direction. There is no atom loss during the compression of the magnetic trap. From measurements of the residual sloshing of the atom cloud we know them both the radial and axial-angular frequencies of the compressed-magnetic trap: $\omega_r = 2\pi \times 838$ and $\omega_a = 2\pi \times 26$ Hz.

By compressing the trap, the phase-space density is increased to 1.1×10^{-7}. There is temperature rise in the atom cloud: T= 690 μK. More importantly, since there is no atom loss in this process, the peak density of atoms is increased to 3.1 $\times 10^{17}$ m^{-3} in the compressed trap. These in turn yield a considerable increment of the elastic-collision rate given by Equation (2.28): $k_{el} = 60$ s^{-1}. With this increment of the elastic collision rate, we set the initial conditions to carry out efficient evaporative cooling, opening the path to BEC.

2.7 Evaporative cooling

In evaporative cooling the average kinetic energy of the particles in an ensemble is lowered by expelling the hottest particles from the system. After evaporation, the temperature is lower, reached once the residual kinetic energy is re-distributed amongst the remaining particles through elastic collisions.

Evaporative cooling of trapped atoms was first demonstrated by cooling magnetically trapped Hydrogen [15], when it was proposed as a feasible method to reach BEC. Evaporative cooling might be the oldest technique for lowering the average velocity of an ensemble of molecules or atoms. Equipment to implement this cooling method varies from a spoon when forcing the evaporation of the hottest molecules of a cup of tea, to antennas and sophisticated wave generators when cooling alkali atoms for example. Regardless of the method of confinement, in a bowl or a magnetic potential, the principle of evaporation is the same. The most energetic atoms in the a distribution are removed by lowering the escape energy of the system with a truncation parameter

$$\eta = \frac{E_t}{k_B T}, \tag{2.29}$$

where E_t is the new escape energy – the truncation energy. Atoms whose energy is greater than E_t are evaporated from the system with probability

$$P(E \geq E_t) = \frac{E_t}{\eta} e^{-\eta}. \tag{2.30}$$

During evaporation, atoms remaining in confinement undergo elastic collisions, defining a new temperature after a thermalization time τ. This temperature is lower as the most energetic atoms leave. If the truncation energy E_t is kept constant, the truncation parameter η will grow, causing an exponential suppression of the probability $P(E \geq E_t)$ to evaporate individual atoms.

2.7.1 Forced-evaporative cooling

In order to avoid the exponential turn off, we vary E_t steadily decreasing it so the evaporation is forced to continue. Methods following this principle are known as forced-evaporative cooling. This technique led researchers to the first BECs of alkali atoms [12, 13, 14], remains today an essential step in the path to BEC.

The goal of forced-evaporative cooling is to increase the phase-space density in a cloud of confined atoms. As atoms with high kinetic energy are expelled from the trap, the atom cloud gets smaller and colder. Even though atoms are lost, the key point is that the temperature falls rapidly enough to increase the phase space density, as I now show.

Let us assume that the atoms are initially in thermal equilibrium inside a harmonic magnetic trap. Their energy follows a Boltzmann distribution

$$P(\epsilon) = A\rho(\epsilon)e^{-\epsilon} \tag{2.31}$$

where ϵ is the normalized energy $\frac{E}{k_BT}$; $\rho(\epsilon)$ is the density of states proportional to ϵ^2 in the case of a harmonic oscillator and A is a normalization constant.

Following truncation, a fraction of atoms whose energy ϵ is greater than η has been coupled out of the system. The relative change in atom number is given by

$$\frac{\Delta N}{N} = \frac{\int_\eta^\infty P(\epsilon)d\epsilon}{\int_0^\infty P(\epsilon)d\epsilon} = \frac{\Gamma(3,\eta)}{2!}, \tag{2.32}$$

where $\Gamma(a,z) = \int_z^\infty t^{a-1}e^{-t}dt$ is the incomplete Gamma function. Thermalization occurs once the remaining kinetic energy inside the trap has been distributed amongst atoms. This happens once (on average) every atom has had several elastic collisions. In this argument I assume that four collisions are enough for thermalization to occur, following the a theoretical result reported in [83]. Thus the thermalization time is $\tau_{\text{th}} = 4/k_{\text{el}}$, where k_{el} is the elastic collision rate, Equation (2.26). To predict the change in time of the atom population inside the trap, it is necessary to also account for the atom loss produced by real experimental conditions such as collisions with the molecules in the background gas or leakage of undesired resonant light into the experiment. In the following equations this loss will be described by the rate $1/\tau_{\text{back}}$ which is assumed constant in time, temperature and atom density. It is assumed to be dependent only on the pressure inside the vacuum chamber.

From these, we see that the population dynamics of the system is given by

$$\frac{1}{N}\frac{dN}{dt} = \frac{k_{el}}{4}\frac{\Gamma(3,\eta)}{2!} + \frac{1}{\tau_{\text{back}}} \tag{2.33}$$

with solution

$$N(t) = N_0 e^{-\alpha_N t/\tau_{\text{back}}}, \tag{2.34}$$

and decay rate

$$\alpha_N = \frac{k_{el}\tau_{\text{back}}}{4}\frac{\Gamma(3,\eta)}{2!} + 1. \tag{2.35}$$

Equation (2.33) demonstrates the exponential nature of the evaporation process. In fact during evaporation all the thermodynamic quantities have an exponential behaviour. Similarly to Equation (2.33), the dynamics of energy leaving the system as atoms depart is given by

$$\frac{1}{E}\frac{dE}{dt} = \frac{k_{el}}{4}\frac{\int_\eta^\infty \epsilon P(\epsilon)d\epsilon}{\int_0^\infty \epsilon P(\epsilon)d\epsilon} + \frac{1}{\tau_{\text{back}}} = \frac{k_{el}}{4}\frac{\Gamma(4,\eta)}{3!} + \frac{1}{\tau_{\text{back}}}. \tag{2.36}$$

From equations (2.33) and (2.36) it can be shown [84] that the temperature behaves as

$$T(t) = T_0 e^{-\alpha_T t/\tau_{\text{back}}}, \tag{2.37}$$

where

$$\alpha_T = \frac{k_{el}\tau_{\text{back}}}{4}\left(\frac{\Gamma(4,\eta)}{3!} - \frac{\Gamma(3,\eta)}{2!}\right). \tag{2.38}$$

during evaporation.

Solutions (2.34) and (2.37) allow us to track in time the behavior of the atom number $N(t)$ and temperature $T(t)$. The volume occupied by the trapped atoms in a three dimensional harmonic trap $V \propto T^{3/2}$ [85]. Using this result we can relate the total number of atoms and their temperature to n, ρ_{PS} and k_{el}, making it also possible to predict these quantities for every time t. It immediately follows that the atom density is proportional to $N/T^{3/2}$. The phase space density is proportional to $N/V\bar{v}_T^3 \propto N/T^3$. Finally the elastic collision rate is proportional to $n\bar{v}_T \propto N/T$. Thus the corresponding coefficients describing the exponential dependence of the elastic collision rate and the phase-space density are:

$$\begin{aligned} \alpha_k &= \alpha_N - \alpha_T \\ \alpha_\rho &= \alpha_N - 3\alpha_T. \end{aligned} \tag{2.39}$$

According to Equation (2.39) $\alpha_N < \alpha_T$ is sufficient to make the elastic collision rate grow exponentially during evaporation. This condition also makes $\alpha_\rho < 0$, ensuring an exponential increment of the phase-space density. Therefore $\alpha_k < 0$ is the condition for a self-sustained evaporation, the so called ‘runaway’ evaporation. Combining equations (2.35), (2.38) and (2.39), one can design an evaporation entering the runaway regime by setting initial conditions in the trapped atom cloud such that

$$k_{el}\tau_{\text{back}} > \frac{4!}{3!\Gamma(3,\eta) - \Gamma(4,\eta)}. \tag{2.40}$$

With Equation (2.40) we can test RF-evaporation in our experiment to find out whether it is in the runaway regime or not. Atom clouds inside the compressed magnetic trap have an elastic-collision rate $k_{el} = 60\ \mathrm{s}^{-1}$. We evaporate far from the surface of the wire ($d > 220\ \mu$m), where the atom loss of the trap is dominated by the interaction between the trapped atoms and the experimental background. Thus, it is valid to assume that at such distances τ_{back} is constant – approximately 100 s – and just dependent on the pressure inside the vacuum chamber. Hence, for our compressed magnetic trap, the term on the left in Inequality (2.40) is $k_{el}\tau_{\mathrm{back}} \approx 6000$. As explained later in Section 2.7.3, the truncation parameter in our case is kept approximately constant at $\eta = 1$. Plugging this truncation parameter into the term on the right of Inequality (2.40) gives 4.7, which is much less than 6000. Therefore our evaporative cooling is well inside the runaway regime of evaporation.

2.7.2 RF-evaporative cooling

An atom at the position r inside the trap feels a magnetic field $B(r)$ which, in the low field regime, shifts its sub-level energy by $\mu_B g_F B(r)$. Therefore an oscillating field with frequency

$$f = \frac{1}{h}\mu_B g_F B(r), \tag{2.41}$$

causes a change of the spin projection m_F in the atom which makes it to leave the trap. For magnetically trapped Rb the frequency f is normally in the RF regime. This is the reason why RF-evaporative cooling is a standard technique to cool Rb atoms down to BEC [12].

When a RF field whose frequency satisfies Equation (2.41) is applied to a magnetic trap, its depth is truncated to

$$E_t = \mu g_F m_F [B(r) - B_0]. \tag{2.42}$$

Hence atoms at the position r are likely to leave the trap. The effect of this energy truncation on a magnetic trap depends on its geometry. In a Ioffe-Pritchard trap like ours, it creates a whole ellipsoidal surface in which atoms will not be trapped. Only the atoms with energy $E > E_t$ will reach this surface and hence, be expelled from the trap.

2.7.3 RF-evaporation on our atom chip

Evaporative cooling in our microtrap is forced with RF emitted by an antenna made of copper wire that sits on the top view port of the vacuum chamber, at about 8 cm from the place where the magnetic trap is formed. The signal is provided by a Standford

Research Systems [(SRS) model DS345] wave-generator.

The truncation parameter η is determined by the trap depth and the initial atom temperature as can be seen from equations (2.29) and (2.42). In our case η is limited by the axial trap depth 0.77 mT and the atoms' temperature 690 μK, which sets the maximum value of η to 0.75, away from its ideal which is 8 [86]. We modulate the frequency of the applied RF following a logarithmic ramp, aiming to keep η approximately constant. The truncation parameter is experimentally set (close to 1) with the initial frequency of evaporation: 13 MHz. We prepare Bose-Einstein condensates with 5×10^4 atoms applying RF ramps that last for 12.5 s, whose final RF frequency is around 600 kHz.

The series of absorption images displayed in Figure 2.16 (a) illustrates RF evaporation in our experiments. These images have been taken from atom clouds cooled down to final RF frequencies progressively lower from top to bottom. Directly from the images, it can be appreciated that atom clouds become smaller and therefore colder as the final frequency is lowered. The labelling temperatures have been measured, as explained in Section 4.2.1, by fitting a Gaussian to the axial profile of each cloud.

The fitted curves along with the measured number density of atoms are shown in Figure 2.16 (b). The top graph plots the axial profile, well fitted by a Gaussian, of a compressed trap that has not been evaporated. Atom clouds in subsequent images have been RF evaporated to final frequencies between 610 and 585 kHz. In these images, the centre of the profile is sharper than Gaussian because a condensed fraction is present. The magnetic trap in the 440 nK picture contains 2.3×10^4 atoms which gives a critical temperature of 320 nK. In the last picture, with a final frequency of 555 kHz, the atom cloud is a nearly pure Bose-Einstein condensate.

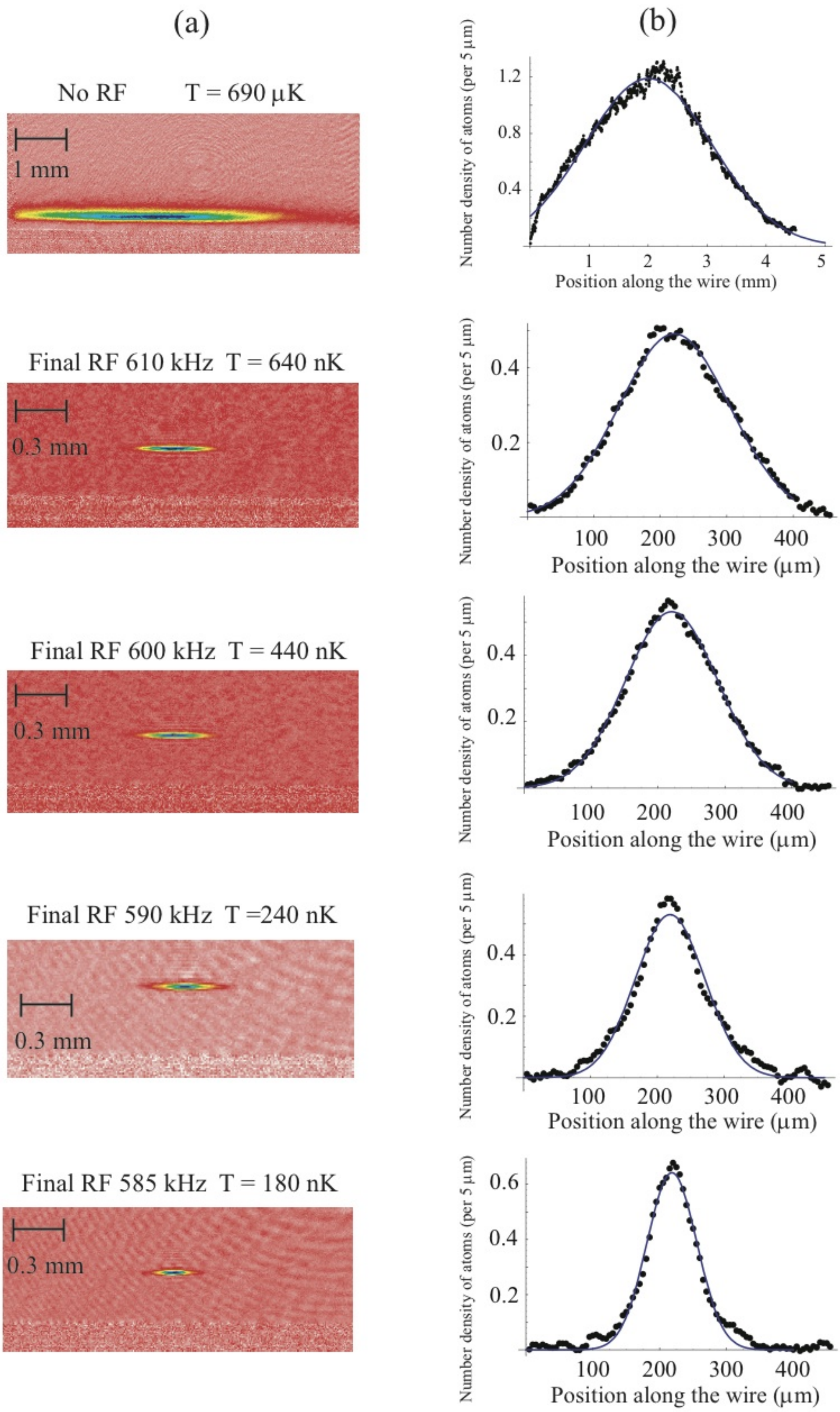

Figure 2.16: Data sequence from atom clouds at several stages of RF-evaporative cooling. From top to bottom: (a) absorption images from higher to lower final RF during evaporation (the top picture is from a cloud that has not been evaporated) and (b) atom number density along z (black dots) and Gaussian fits to these data (blue curves). The BEC transition temperature is reached at final RF frequency between 600 and 585 kHz.

Chapter 3

Thermally induced spin flips

Transitions of spin projection in the magnetic trapped states of ^{87}Rb atoms are resonant at RF frequencies, for which the wavelength λ is a few hundred meters. These transitions change the shape of the potential felt by the atoms and lead to atom loss from magnetic traps. Atom loss due to spin flips is a consequence of the relaxation of the trapped states. In an unconfined space, vacuum fluctuations yield a very small atom loss, which is not measurable on any practical time scale. Such atom loss is increased if non-zero temperature effects are considered, but remains small enough to be negligible in experiments. Near the surface of a dielectric or conductor however, the spontaneous decay rate of the trapped states is enhanced by thermal fields that originate inside the material.

This is the case in microtraps which suffer from large relaxation rates and therefore, from large atom loss as the atoms approach the surface of atom chips. The coupling of the atoms with the thermal field of these surfaces causes a dramatic increase in the spontaneous decay rate from the trapped states. This in turn leads to high atom loss rates from microtraps. Henkel *et al.* [55] predicted spin state lifetimes of trapped atoms as short as a few milliseconds for atoms trapped one micrometer from a planar slab of a conductor or a dielectric.

The work reported in this chapter was the first observation of this phenomenon, by which I mean surface thermal fields as opposed to technical noise [56]. Section 3.1 explains spontaneous spin relaxation at finite temperature. Section 3.2 describes the system of cold atoms near the surface of materials. Section 3.3 offers an overview of the theories developed by Henkel *et al.* [55] and by Rekdal et.al [57] to describe the spontaneous relaxation of trapped states in the vicinity of a dielectric or conductor. The following sections, 3.4 and 3.5, discuss the experiments we carried out to measure rates of atom loss from our microtrap.

3.1 Atom loss due to spontaneous decay

Atoms are trapped near magnetic field minima by exploiting the interaction between their magnetic dipole moment

$$\boldsymbol{\mu} = g_S\hat{\mathbf{S}} + g_L\hat{\mathbf{L}} - g_I\frac{m_e}{m_p}\hat{\mathbf{I}}, \tag{3.1}$$

and the local magnetic field, Equation (1.2). In Equation (3.1), $g_S \approx 2$, g_L and g_I are the g-factors of the operators of spin $\hat{\mathbf{S}}$, angular momentum $\hat{\mathbf{L}}$ and nuclear spin $\hat{\mathbf{I}}$ respectively. For the ground state of alkali atoms $L = 0$. The nuclear spin term in Equation (3.1) is negligible because the electron mass m_e is much smaller than the proton mass m_p. Thus Equation (1.2) reduces to

$$H_Z = -\mu_B g_S \hat{\mathbf{S}} \cdot \hat{\mathbf{B}}(\mathbf{r}), \tag{3.2}$$

where $\hat{\mathbf{S}}$ is the spin operator and $\hat{\mathbf{B}}(\mathbf{r})$ is local magnetic field operator. Equation (3.2) states that the spin of atoms is coupled to the local magnetic field. A transition of the spin projection in the atoms will modify the confining potential, making it weaker, null or repulsive, depending on the quantum numbers of the final atomic state.

A cold atom cloud is localized near the bottom of the trap where the magnetic field is B_0, where spin flip frequency is given by

$$\omega_0 \equiv \frac{1}{\hbar}\mu_B g_F B_0. \tag{3.3}$$

The transition rate between the initial state $|i\rangle$ and possible final states $|j\rangle$ is given by Fermi's Golden Rule

$$R_i = \frac{2\pi}{\hbar^2}\sum_j \mid \langle j \mid \mu_B g_S \hat{\mathbf{S}} \cdot \hat{\mathbf{B}} \mid i\rangle \mid^2 \mathcal{D}(\omega_{ij}), \tag{3.4}$$

where

$$\hat{\mathbf{B}} = \sum_k A_k \mathbf{k} \times \varepsilon_{\mathbf{k}}\left[\hat{a}_k e^{-i\omega_k t + i\mathbf{k}\cdot\mathbf{r}} + \hat{a}_k^\dagger e^{i\omega_k t - i\mathbf{k}\cdot\mathbf{r}}\right] \tag{3.5}$$

is the operator of the interacting magnetic field. Here

$$\mathcal{D}(\omega_{ij}) = \frac{V\omega_{ij}^2}{\pi^2 c^3}, \tag{3.6}$$

is the density per unit angular frequency of modes at frequency $\omega_{ij} \equiv \omega_i - \omega_j$ in a large volume V. In Equation (3.5) the field is expanded on a basis of plane waves, each one labelled by the wave vector $\mathbf{k}$; $\mathbf{r}$ is the position of the active electron; $A_k = i\sqrt{\frac{\hbar}{2\epsilon_0 V\omega_k}}$ is the field normalization, where ω_k is the angular frequency of the mode k; and ε_k is its vector polarization. Fermi's Golden Rule calculates the decay rate of the state $|i\rangle$ as a function of the amount of modes resonant to all the possible decaying transitions in the space were the atom is localized.

I will calculate the spontaneous decay rate to the specific state $|j\rangle = |f\rangle$ with resonant transition $\omega_{ij} = \omega_0$. I will first deduce the rate due to the q-polarized fields $R_{if,\mathrm{q}} \equiv R_{\mathrm{q}}$, and then add up the contribution of each spatial direction to finally obtain the complete spontaneous decay rate R_{if} from the initial state $|i\rangle$ to the final state $|f\rangle$.

Because the wavelength of the field is very long compared with the size of the atom, the dipole approximation is a good one, so the qth component of $\hat{\mathbf{B}}(\omega_0)$ is given by [87]

$$\hat{B}(\omega_0) = i\sqrt{\frac{\hbar}{2\varepsilon_0 V \omega_0}}\frac{\omega_0}{c}(\hat{a}_0 - \hat{a}_0^{\dagger}), \tag{3.7}$$

where $\hat{a}_0^{\dagger}$ and $\hat{a}_0$ are the creation and annihilation operators of photons with angular frequency ω_0.

By combining Equation (3.7) with Equation (3.4), we find that the spontaneous decay rate due to q-polarized light is given by

$$R_{\mathrm{q}} = \frac{\mu_0 \omega_0 \pi}{V\hbar}\mathcal{D}_{\mathrm{q}}(\omega_0) \mid \langle f \mid \mu_B g_S \hat{S}_{\mathrm{q}} \mid i\rangle \mid^2 . \tag{3.8}$$

The mode-density $\mathcal{D}_{\mathrm{q}}(\omega_0)$ in each of the three q-directions is one third of the total density given by Equation (3.6). Hence the total spontaneous decay rate R_{if} is

$$R_{if} = \frac{\mu_0(\mu_B g_S)^2 \omega_0^3}{3\pi\hbar c^3} S_{if}^2, \tag{3.9}$$

where the angular factor is defined as

$$S_{if}^2 \equiv \sum_{\mathrm{q}} \mid \langle f \mid \hat{S}_q \mid i\rangle \mid^2 . \tag{3.10}$$

We now focus on atoms in our microtrap and deduce the loss due to spontaneous decay in free space. Atoms are optically pumped to the $5S_{1/2}, |F = 2; m_F = 2\rangle \equiv |2\rangle$ sub-level before being loaded into the magnetic trap. Thus the confining potential is given by the corresponding trapping energy $U(r)$, Equation (2.14) with the quantum numbers of the trapped state: g_F=1/2 and $m_F = 2$,

$$U(r) = \mu_B g_F m_F B(r) = \mu_B B(r), \tag{3.11}$$

where $B(r)$ is once again the magnitude of the magnetic field of the trap at position r of the atom.

The trapped state $|2\rangle$ can decay spontaneously to the $5\mathrm{S}_{1/2}, |F=2, m_F=1\rangle \equiv |1\rangle$ sub-level with decay rate R_{12}, obtained by introducing the angular factor S_{21}^2=1/8 [1] into Equation (3.9). The quantum state $|1\rangle$ is also low field seeking, but it feels a weaker attractive potential

$$U(r) = \frac{1}{2}\mu_B B(r). \tag{3.12}$$

Atoms that were previously trapped in state $|2\rangle$ will escape from this potential if they are energetic enough. From the $|1\rangle$ sub-level, atoms can spontaneously decay to the $5\mathrm{S}_{1/2}, |F=2, m_F=0\rangle \equiv |0\rangle$ lower sub-level. The angular factor that weights this transition is S_{10}^2= 3/16; the relative decay rate is R_{10}/R_{21}=3/2. Atoms in the quantum state $|0\rangle$ are almost insensitive to magnetic fields and are all lost. Figure 3.1 illustrates the chain of decays leading to atom loss from the magnetic trap: $|2\rangle \rightarrow |1\rangle \rightarrow |0\rangle$. It shows the potential (in one dimension) felt by the atoms in the states involved during the loss process.

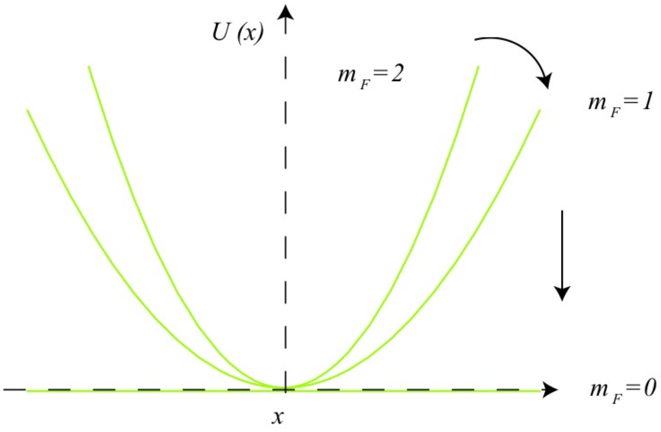

Figure 3.1: One dimensional schematic of the spontaneous decay sequence leading to atom loss from a magnetic trap. The green curves and line are the potentials felt by atoms in the different quantum states.

The loss rate $\Gamma_{sp} \equiv R_{21}$ is given by Equation (3.9). For f_0= 1 MHz, which is a typical experimental value, the lifetime of atoms trapped in free space at zero temperature is $\tau_{sp} = 1/\Gamma_{sp} = 2 \times 10^{24}$ s. This is far too long to be detectable. To include effects of non-zero temperature, it is necessary to weight the decay rate by the factor $(\bar{n}_{th}+1)$, where $\bar{n}_{th}$ is the mean number of photons per mode at frequency ω_0 in the blackbody field at temperature T [88]

$$\bar{n}_{th} = \frac{1}{e^{\hbar\omega_0/k_B T} - 1}. \tag{3.13}$$

Hence the lifetime τ of the trapped state at finite temperature is

$$\tau = \frac{1}{\Gamma_{sp}(\bar{n}_{th}+1)}. \tag{3.14}$$

---

[1] Details on the derivation of angular factors S_{ij}^2 are in Appendix A

For example, at 300 K the lifetime corresponding to R_{21} with $f_0 = 1$ MHz is reduced to $\tau_{bb} = 2 \times 10^{17}$ s. This time is still very long, being comparable to the age of the universe!

In our experiment there are two additional causes of atom loss from the magnetic trap. It is for this reason that we are able to observe atom loss from traps in the experimental time scale. We typically do experiments under pressures in the low 10^{-11} torr scale, where the density of particles is of the order of 10^5 cm^{-3}. Collisions between the cold atoms and these particles are the dominant source of atom loss from magnetic traps. In addition to these collisions, resonant photons may leak into the vacuum chamber. This is another source of atom loss as resonant photons induce transitions in the trapped quantum states. Collisions with the background gas and undesired resonant light yield an atom loss rate $1/\tau_{\text{back}} = 10^{-2}$ s^{-1}, which we determine experimentally with atoms trapped more than 200 μm away from the guide wire. This situation changes dramatically when we pull the microtrap to a few tens of micrometers from the surface of the atom chip.

3.2 Atom loss near surfaces

Section 3.1 explains how one can calculate the atom loss induced by the thermal fluctuations of the blackbody in free space. This section outline the spontaneous decay of the trapped state near surfaces, where a much larger field noise induces a greater rate of atom loss.

Close to the surface of materials, the mode density relevant for Fermi's Golden Rule is considerably increased due to the surface modes of the material. Figure 3.2 is a schematic of the system that we are considering here. An atom cooled down to about one microkelvin is confined at a distance of tens of micrometers from the surface of a dielectric or conductor at room temperature.

The charge distribution inside of the material is given by the polarization which is related in turn to the electric field $\mathbf{E}(\mathbf{r}, t)$ by

$$\mathbf{P}(\mathbf{r}, t) = \varepsilon_0 \int_0^\infty \chi(\mathbf{r}, \tau)\mathbf{E}(\mathbf{r}, t - \tau) d\tau + \mathbf{P}_N(\mathbf{r}, t), \tag{3.15}$$

where $\chi(\mathbf{r}, \tau)$ is the linear susceptibility characteristic of individual materials and $\mathbf{P}_N(\mathbf{r}, t)$ is the polarization noise, a Langevin-type of term that accounts for the fluctuations induced by the dissipation in the material. The first term in Equation (3.15) means that the charge distribution at time t depends upon the present and past values of the applied electric field. How fast the polarization reacts to the changes of

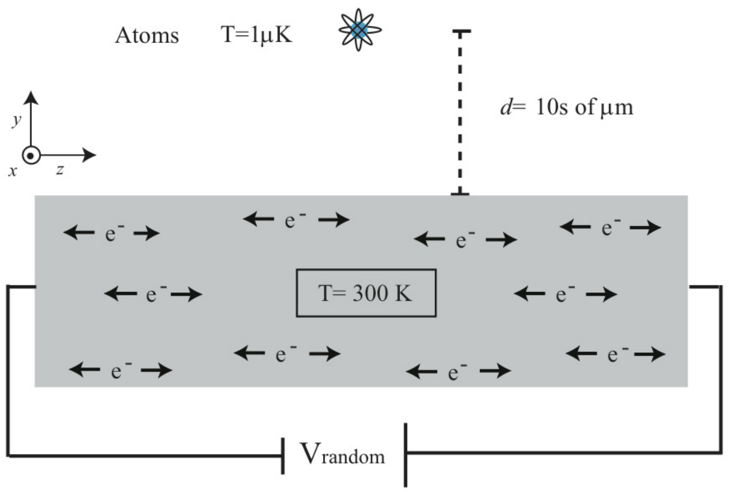

Figure 3.2: Schematic of the system in our experiment. A 1 μK atom cloud in a microtrap is coupled to the thermal field produced by a block of material (the wire) at room temperature. The fluctuations of the vacuum inside the material are enhanced with an additional set of modes in the space occupied by matter. These are transmitted through the surface and coupled to the spin of the atoms, inducing high loss rates in microtraps. Forming part of the internal modes of the material, there are oscillating charges giving rise to random fluctuations of the voltage across the block (in the case of conductors). This is the so called Johnson noise [89]

electric field depends on the properties of the material which are contained in $\chi(\mathbf{r}, t)$. In addition, the second term of Equation (3.15) states that the polarization fluctuates because there is power being dissipated in the system due to the resistivity of the material which opposes to the motion of the charges.

The oscillating charges of the modes inside the material induce a random voltage across the block, effect known as Johnson noise [89] (see Figure 3.2). The near field of a conductor is formed by the fields emitted by the oscillating charges of the vacuum modes. These fluctuating fields travel through the material and are transmitted through its surface, giving rise to a white noise within the vicinity of the media interface. Following transmission, the power of the field fluctuations is not attenuated significantly until they travel a distance λ, their wavelength. Thus the fluctuations whose frequencies are in the RF regime are not completely attenuated until a few hundreds of meters from the surface. Near the surface, the power of these thermal RF fields is stronger than the blackbody radiation, inducing in consequence higher decay rates of the trapped states of the atoms. At a few tens of micrometers from the surface of atom chips the RF spectrum of the thermal fluctuations drive spin flips at higher rates than $1/\tau_{\text{back}}$, being the dominant loss mechanism in many microtrap experiments.

In addition to spin flips, the coupling of the electric and magnetic dipole moments of atoms to the thermal field of surfaces also gives rise to another phenomenon: the Casimir Polder Force. This also leads to an increment of atom-loss rates in microtraps as a function of the atom-surface distance d. However it is dominant in a different range as explained in Section 3.5.2.

3.2.1 Spin flips near surfaces

Section 3.1 shows how the fluctuations of the vacuum induce atom loss from magnetic traps through the $|2\rangle \rightarrow |1\rangle$ transition due to their coupling with the spin of atoms. This coupling is much stronger when the fluctuations of the vacuum have been amplified by the presence of matter, leading to greater atom loss from magnetic traps. The calculation of the rate of spin flips driven by the thermal field of surfaces requires a more general mathematical treatment than the spontaneous decay rate in free space. This is because the interacting field is dependent on the geometry of the material and its conducting properties.

Equation (3.15) is the simplest relation between the electric component of the field fluctuations through a dielectric or conductor with its internal charge distribution. For spin-flip rate calculations, the magnetic component is the relevant one. It is connected to the distribution of charges through Equation (3.15) and Maxwell's equation

$$\nabla \times \hat{\mathbf{E}}(\mathbf{r}, t) = -\frac{\partial \hat{\mathbf{B}}(\mathbf{r}, t)}{\partial t}. \tag{3.16}$$

The calculation of the magnetic spin-flip rate due to the thermal field of a material already been done [55, 57], motivated by our experiment among others and, more generally by the relevance of this process in atom chips. The next section gives an overview of the mathematical methods used to approach and solve the problem.

3.3 Thermal spin flips: two theoretical approaches

The first prediction of thermal spin flips in microtraps was made by Henkel *et al.* [55] for the case of a planar slab of dielectric or conductor as the thermal surface. Published a few years later, reference [57] presents a theoretical treatment which permits us to calculate the thermal field of a dielectric or conductor with an arbitrary shape. The authors of this paper took the case of the geometry of our guide wire to show their theory and test it against our data. A more recent theoretical publication concerning the prediction of this rate is by S. Scheel *et al.* [90]. This paper presents scaling laws that apply to thin films of conductors and super conductors based on the model presented in [57].

Both theoretical approaches [55] and [57] use formulations of the fluctuation-dissipation theorem [91, 88] to account for the fluctuations of the modified vacuum interacting with atoms. This theorem shows that in a system with dissipation, the quantity that is damped must also fluctuate by more than the ordinary vacuum or thermal fluctuation. Reference [55] uses this theorem to calculate the magnetic field fluctuations near a planar slab of conductor or dielectric and hence to determine the spin flip rate of trapped atoms. The formulation used in that article achieves the fluctuations through a suitable random force. Reference [57] applies the theorem directly to a material with arbitrary geometry. In this case the authors calculate first the thermal fluctuations of the magnetic field near the material and then introduce them into the Zeeman Hamiltonian of the atom. Both approaches result in an enhancement of the thermal electromagnetic field, whose interaction with the atom increases the decay rate to the lower state.

3.3.1 Atoms near a planar slab

Atoms in our experiments are held close to a cylindrical wire. Henkel *et al.* [55] worked out the spin flip rate of atoms near a planar slab of conductor or dielectric. However their calculation qualitatively reproduces effects of atom loss due to spin flips in our microtrap.

The authors deduce a master equation in which the magnetic interaction force due to the local magnetic field is taken as a random operator. This equation is obtained by applying the time dependent Schrödinger equation to the atom's density matrix with the hamiltonian of the random force. In the Markov limit, the master equation yields a relaxation dynamics with the form of Liouville's equation

$$\dot{\rho} = -\frac{i}{\hbar}[H_Z, \rho] - \frac{1}{2}\{\Gamma, \rho\}, \tag{3.17}$$

where the term $\frac{1}{2}\{\Gamma, \rho\} = \frac{1}{2}[\Gamma\rho + \rho\Gamma]$ is added to include relaxation mechanisms amongst the different quantum states.

The decay rate $\Gamma_{i\to f}$ appears when computing the matrix elements of the operator $\dot{\rho}$ for initial and final states i and f, Equation (9) in [55]:

$$\Gamma_{i\to f} = \sum_{qp} \frac{\langle i|\mu_p|f\rangle\langle i|\mu_q|f\rangle}{\hbar^2} S_B^{qp}(d; -\omega_{fi}). \tag{3.18}$$

In Equation (3.18), $\langle i|\mu_{q,p}|f\rangle$ are matrix elements of the atom's magnetic dipole operator, as calculated for the spontaneous decay rate in Equation (3.8). Which in turn is reduced to the matrix elements $\hat{S}_{if}$ of the spin operator calculated in Appendix A.

The term $S_B^{qp}(d; -\omega_{fi})$ is the key mathematical tool used in [55]. It is called the spectral density and is defined as

$$S_B^{qp}(d; -\omega_{fi}) = \int_{\infty}^{\infty} d\tau \langle B_q(\mathbf{r}, t+\tau) B_p(\mathrm{r}, t)\rangle e^{i\omega\tau}, \tag{3.19}$$

where B_q are the spatial components of the magnetic field. The spectral density, Equation (3.19), is the Fourier transform of the correlation function of the magnetic field at time t and t + τ. Equation (3.18) is Fermi's Golden Rule for atoms close to a surface with the spectral density being evaluated at frequency ω_{fi} to conserve energy.

By applying the fluctuation-dissipation theorem to obtain the magnetic field in terms of the Green tensor h_{qp}, where q and p again denote spatial components, the spectral density is written as [55]

$$S_B^{qp}(\mathbf{r}; -\omega_{fi}) = \frac{(\bar{n}_{th}+1)\Gamma_{sp}}{c^2} h_{qp}(kz), \tag{3.20}$$

The tensor h_{qp} is diagonal with components $h_{xx} = h_{zz} \equiv h_{\parallel}$ and $h_{yy} \equiv h_{\perp}$ in the frame of reference of our atom chip. Here the guide wire defines the z-direction and y is the vertical spatial component, see Figure 3.2. The elements $h_{\parallel}$ and $h_{\perp}$ are given by (Equation 22 in [55])

$$\begin{aligned} h_{\parallel} &= \frac{3}{4}\mathrm{Re}\int_0^{\infty} \frac{u\,du}{v} e^{2ikvd}(r_\pi(u) + (u^2-1) r_\sigma(u)) \\ h_{\perp} &= \frac{3}{4}\mathrm{Re}\int_0^{\infty} \frac{u^3 du}{v} e^{2ikvd} r_\sigma(u), \end{aligned} \tag{3.21}$$

where

$$v = \begin{cases} \sqrt{1-u^2}, & 0 \le u \le 1, \\ i\sqrt{u^2-1}, & u \ge 1; \end{cases} \tag{3.22}$$

and r_π and r_σ are the Fresnel coefficients for π and σ-polarized fields

$$r_\pi = \frac{\varepsilon v - \sqrt{\varepsilon - u^2}}{\varepsilon v + \sqrt{\varepsilon - u^2}}, \tag{3.23}$$

$$r_\sigma = \frac{v - \sqrt{\varepsilon - u^2}}{v + \sqrt{\varepsilon - u^2}}. \tag{3.24}$$

The evanescent field at a distance d from the surface is related to the properties of the material by the relative dielectric function ε. In the low frequency limit, which is the case for the RF frequency ω_{fi} of the spin flip transition, ε has the form [92]

$$\varepsilon \simeq \frac{i}{\varepsilon_0 \rho \omega}. \tag{3.25}$$

The relative dielectric function determines the attenuation of the electric field whilst propagating inside a block of material. This can be seen through the definition of skin depth

$$\delta \equiv \frac{1}{k}\sqrt{2\varepsilon_o \rho \omega}, \tag{3.26}$$

which is the distance that it takes to attenuate the amplitude of an electromagnetic wave (with angular frequency ω) by a factor of e^{-1} when propagating through a material with resistivity ρ [93].

By plugging Equation (3.20) into Equation (3.18), Henkel *et al.* calculated the spin-flip rate for the particular case of a transition between projections of angular momentum -1/2 and 1/2, Equation (35) in the paper. One can obtain an expression to calculate the rate of decay between state $|i\rangle$ and $|f\rangle$ by re-scaling this expression with the corresponding angular factor S_{if}^2

$$\Gamma_{i\to f} = \frac{\mu_B^2 g_S^2 \omega_0^2 T}{6\pi\varepsilon_0 \hbar^2 c^5}\left\{(h_\parallel(kd)+1)(1+\cos^2\theta)+(h_\perp(kd)+1)\sin^2\theta\right\}\sum_q |\langle i|\hat{S}_q|f\rangle|^2, \tag{3.27}$$

where θ is the angle between the offset field and the normal to the atom chip surface, $\pi/2$ in our apparatus.

In order to calculate the decay rate $\Gamma_{2\to 1}$ near a planar slab, we integrated numerically Equation (3.21)[2] and re-weighted Equation (3.27) with the angular factors corresponding to the states $|2\rangle$ and $|1\rangle$. These are the theoretical curves that are plotted later on in this chapter in figures 3.10 and 3.11, where we compare our experimental results with theory.

Finally, I highlight two useful limits of the lifetime $\tau = 1/\Gamma_{i\to f}$, corresponding to large and small atom-surface distance d in comparison with the skin depth δ of the material [55]

$$\tau \propto \begin{cases} \omega_0^3 \delta^2 d & d << \delta \\ \frac{\omega_0^3 d^4}{\delta} & d >> \delta \end{cases} \tag{3.28}$$

The dependence on d gives a clear signature for atom loss due to thermal spin flips as opposed to other mechanisms. The frequency dependence is also quite specific. Note though that it is not simply ω_0^3 since $\delta \propto \omega^{-1/2}$.

3.3.2 Atoms near materials with arbitrary geometry

This section is an overview of the theory proposed by P. K. Rekdal *et al.*. [57] to predict thermal spin-flip rates of atoms trapped near the surface of a conductor or dielectric with arbitrary geometry.

The electric field and the polarization of the material are related through Equa-

---

[2] We are indebt to P.K. Rekdal for calculating these integrals.

tion (3.15). The polarization noise $\mathbf{P}_N(\mathbf{r},\omega)$ is defined according to the fluctuation-dissipation theorem which states that the macroscopic changes in polarization are given by the imaginary part of the dielectric function $\varepsilon(r,\omega)$,

$$\mathbf{P}_N(\mathbf{r},\omega) = i\sqrt{\frac{\hbar\epsilon_0}{\pi}\varepsilon_I(\mathbf{r},\omega)}\hat{\mathbf{f}}(\mathbf{r},\omega); \tag{3.29}$$

where the bosonic field operator $\hat{\mathbf{f}}(\mathbf{r},\omega)$ has been introduced to account for excitations of the system induced by the interaction between the field and the absorbing material.

Now, the displacement field

$$\mathbf{D}(\mathbf{r},t) = \varepsilon_0\mathbf{E}(\mathbf{r},t) + \mathbf{P}(\mathbf{r},t) \tag{3.30}$$

can be transformed into the Fourier space by integrating Equation (3.15). Once $\mathbf{D}(\mathbf{r},\omega)$ has been found, Maxwell's equations show that the electric field $\mathbf{E}(\mathbf{r},\omega)$ satisfies the Helmholtz equation

$$\nabla\times\nabla\times\mathbf{E}(\mathbf{r},\omega) - \frac{\omega^2}{c^2}\varepsilon(\mathbf{r},\omega)\mathbf{E}(\mathbf{r},\omega) = \omega^2\mu_o\mathbf{P}_N(\mathbf{r},\omega), \tag{3.31}$$

The solution for Equation (3.31) is

$$\mathbf{E}(\mathbf{r},\omega) = \omega^2\mu_0\int d^3r' G(\mathbf{r},\mathbf{r}',\omega)\cdot\mathbf{P}_N(\mathbf{r}',\omega) \tag{3.32}$$

where $\mathbf{G}(\mathbf{r},\mathbf{r}',\omega)$ is the same Green tensor as Equation (3.20) of Henkel's theory. It is defined by

$$\nabla\times\nabla\times\mathbf{G}(\mathbf{r},\mathbf{r}',\omega) - \frac{\omega^2}{c^2}\varepsilon(\mathbf{r},\omega)\mathbf{G}(\mathbf{r},\mathbf{r}',\omega) = \delta(\mathbf{r}-\mathbf{r}')\mathbf{U}, \tag{3.33}$$

$\mathbf{U}$ being the unit dyad. A dyad is a matrix defined by the product of two matrices of the same rank.

The magnetic component is then obtained by the relevant Maxwell equation in Fourier space

$$\mathbf{B}(\mathbf{r},\omega) = \frac{1}{i\omega}\nabla\times\mathbf{E}(\mathbf{r},\omega). \tag{3.34}$$

The magnetic field operator in the Schrödinger picture

$$\hat{\mathbf{B}}(\mathbf{r}) = \hat{\mathbf{B}}^{(+)}(\mathbf{r}) + \hat{\mathbf{B}}^{(-)}(\mathbf{r});\quad \hat{\mathbf{B}}^{(+)}(\mathbf{r}) = [\hat{\mathbf{B}}^{(-)}(\mathbf{r})]^\dagger \tag{3.35}$$

is obtained by integrating $\mathbf{B}(\mathbf{r},\omega)$ with respect to frequency

$$\hat{\mathbf{B}}^{(+)}(\mathbf{r}) = \int_0^\infty \mathbf{B}(\mathbf{r},\omega)d\omega. \tag{3.36}$$

Then the magnetic field of Equation (3.36), in combination with Equation (3.2), yields a Heisenberg equation of motion with the form of Equation (3.17) for the density matrix of atomic states $|i\rangle$ and $|f\rangle$. The decay rate $\Gamma_{i\to f}$ appears when calculating the corresponding matrix element with a magnetic field of frequency ω_0

$$\Gamma_{i\to f} = \mu_0\mu_B g_S \langle f|\hat{S}_p|i\rangle\langle f|\hat{S}_q|i\rangle \times \mathrm{Im}[\nabla\times\nabla\times\mathbf{G}(\mathbf{r}_A,\mathbf{r}_A,\omega_0)]_{pq}, \tag{3.37}$$

where $\mathbf{r}_A$ is the position of the atom. Equation (3.37) is the analog of Equation (3.18) by Henkel *et al.*: both are generalizations of Fermi's Golden Rule. In equation (3.37), all the information about the field and the geometry of its source is contained in the factor $\mathrm{Im}[\nabla\times\nabla\times\mathbf{G}(\mathbf{r}_A,\mathbf{r}_A,\omega_0)]$ and it is straightforward to identify the rest of the factors as the spin part of the Zeeman Hamiltonian of the interaction.

In order to discuss the spin-flip rate when atoms are near the wire of our experiment, the authors separated it into the contribution made by the free space field fluctuations $\Gamma^{\mathrm{free}}_{i\to f}$ and the correction to this due to the presence of the wire $\Gamma^{\mathrm{wire}}_{i\to f}$. This is possible because the Helmholtz equation and hence, the Green tensor in Equation (3.33) of the field can be separated into two parts $\mathbf{G}(\mathbf{r},\mathbf{r}',\omega_0) = \mathbf{G}^{\mathrm{vac}}(\mathbf{r},\mathbf{r}',\omega_0) + \mathbf{G}^{\mathrm{wire}}(\mathbf{r},\mathbf{r}',\omega_0)$. The vacuum part is diagonal

$$\mathrm{Im}[\nabla\times\nabla\times\mathbf{G}(\mathbf{r}_A,\mathbf{r}_A,\omega_0)]_{pq} = \frac{k^3}{6\pi}\delta_{pq}, \tag{3.38}$$

and together with Equation (3.37), it yields the result we know from Section (3.1): $\Gamma^{\mathrm{vac}}_{2\to 1} = \Gamma^{\mathrm{sp}}$.

The rate $\Gamma^{\mathrm{wire}}_{1\to 2}$ is derived by combining the result for $\mathbf{G}^{\mathrm{wire}}(\mathbf{r},\mathbf{r}',\omega_0)$, Equation (29) in [57], and Equation (3.37)

$$\Gamma^{\mathrm{wire}}_{2\to 1} = \frac{3}{8}\Gamma^{\mathrm{sp}}\sum_{n=0}^{\infty}(2-\delta_{0n})\mathrm{Re}[(I^{\mathrm{lim}}_n)_{yy} + (I^{\mathrm{lim}}_n)_{yy}]). \tag{3.39}$$

Here the $(I^{\mathrm{lim}}_n)_{qq}$ are integrals defined in [57] containing information about the field close to the surface. The theoretical curves for the lifetime near a cylindrical wire shown in figures 3.10 and 3.11 were calculated with Equation (3.39).

Finally the authors extended the theory to the case of thin films of conductors and superconductors [90]. They found general scaling rules for the lifetime of the trapped state τ not just in terms of d and δ but also in terms of the thickness h of the films

$$\tau \propto \begin{cases} \omega_0^3\delta^2 d & d << \delta, h \\ \frac{\omega_0^3 d^4}{\delta} & d, h >> \delta \\ \frac{\omega^3\delta^2 d^2}{h} & \delta >> d >> h \end{cases}. \tag{3.40}$$

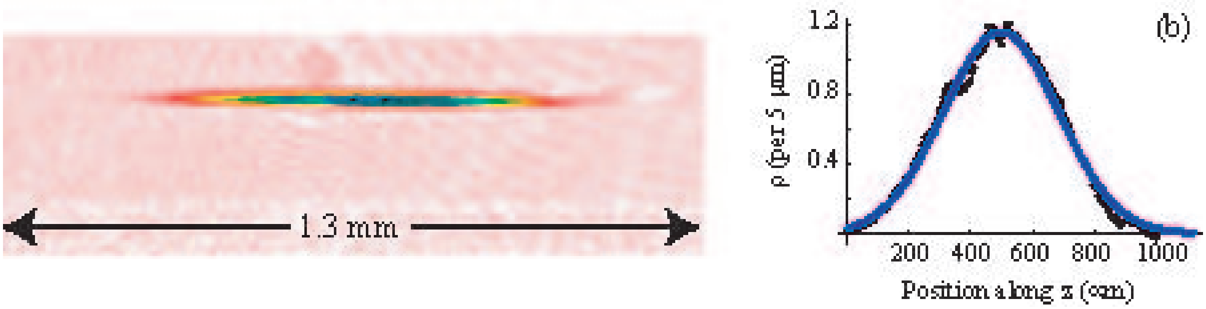

Figure 3.3: Typical sample of cold atoms prepared for lifetime measurements. (a) absorption image of atoms cooled down to 5.6 μK with a RF ramp from 13 to 1 MHz. The temperature was measured by fitting a Gaussian to its axial profile (b) as explained in Section 4.2.1.

The two first scaling rules in Equation (3.40), recover the limits obtained by Henkel *et al.* for the infinite slab. The third one is a new and very useful result. It shows that the spin flip lifetime can be made long close to an atom chip by making the film thickness small enough.

3.4 Experiments

3.4.1 Our system: cold atoms near a cylindrical wire

Although we were able to prepare Bose-Einstein condensates they were not required for our experiments, which were carried out using clouds of atoms at a few microkelvin near the surface of our guide wire, see Figure 3.3. This made the experiment easier.

One of the problems with BEC experiments using atom chips is running high density currents inside the vacuum chamber. The dissipation of power through the wires in UHV can heat the chip and degrade the vacuum if the current is running for a long enough time. The wires of our atom chip are no exception: they outgas enormously if the magnetic trap is switched-on for longer than around 15 s. After this time, the pressure inside the vacuum chamber is typically increased to around 1×10^{-9} torr. Decreasing in consequence, the background limited lifetime of our magnetic trap from more than one hundred to about twenty seconds.

The RF-evaporation routine that we normally use to prepare Bose-Einstein condensates is 12.5 s long. This evaporation time leaves just 5 s for us to observe atom loss from our magnetic trap. Because of this, we shorten the RF-evaporative cooling stage from 12.5 s to 6 s. With this change in the evaporation time, we do not make a BEC but we are able to observe atom loss from the microtrap for 9 s.

The initial RF frequency for evaporation is 13 MHz, the same as in the typical preparation of condensates. The final frequency however, was normally between 2 and

0.7 MHz in this case, yielding temperatures of a few microkelvin. Figure 3.3 (a) shows an absorption image of a typical cloud of cold atoms prepared for spin-flip experiments. This atom cloud was cooled with a RF sweep from 13 to 1 MHz giving a 5.6 μK axial temperature. It was left in the evaporation position, corresponding to 6.9 A through the guide wire and 2.9 mT of bias field.

The cross section of our guide wire is shown in Figure 3.4. This wire has a 500 μm diameter (much larger than micro-fabricated wires now used in atom chips) and has three layers. The core is made of copper, with 190 μm radius. It is surrounded by a 50 μm thick layer of aluminium which in turn is insulated by 10 μm of ceramic (Al_2O_2).

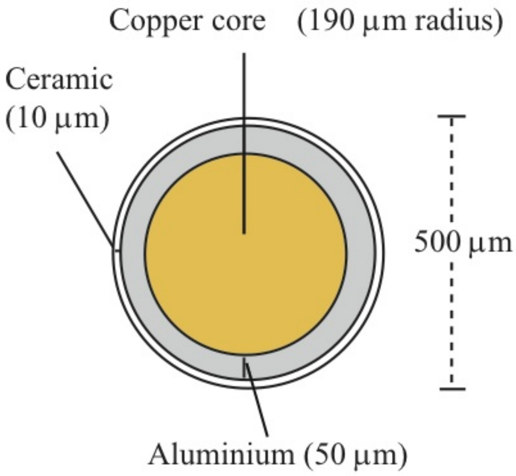

Figure 3.4: Cross section of our cylindrical guide wire. It has two conducting layers, copper and aluminium and an insulating layer of ceramic.

A crucial parameter for the experiments on spin flips is the distance d from the atoms to the conducting surface of the wire, the aluminium layer. In order to be accurate with this parameter, we need to find a reference in the images from which d can be measured. For this, we find the current that brings the atom cloud to the position of the ceramic surface of the wire. In these experiments, we first count the atoms in an atom cloud far from the surface, with 6.9 A through the wire and 2.9 mT bias field, as the atom cloud shown in Figure 3.3. Then we pull the atoms towards the surface by linearly ramping the current through the guide wire to a smaller value while leaving the bias field constant. This was done over the last second of evaporation as shown in Figure 3.5. The atoms were left at this position for 100 ms, brought far from the wire again by ramping current back to 6.9 A and then counted as illustrated by the red dashed lines in Figure 3.5. We repeated this procedure until we had images with no atoms left in the trap. The blue circles in Figure 3.6 plot the atom number counted far from the surface versus the current $I(y)$ holding atoms near the surface. With these experiments we associate the position of the ceramic surface to 4.05 A, the current for which approximately half of the atoms are lost (see Figure 3.6).

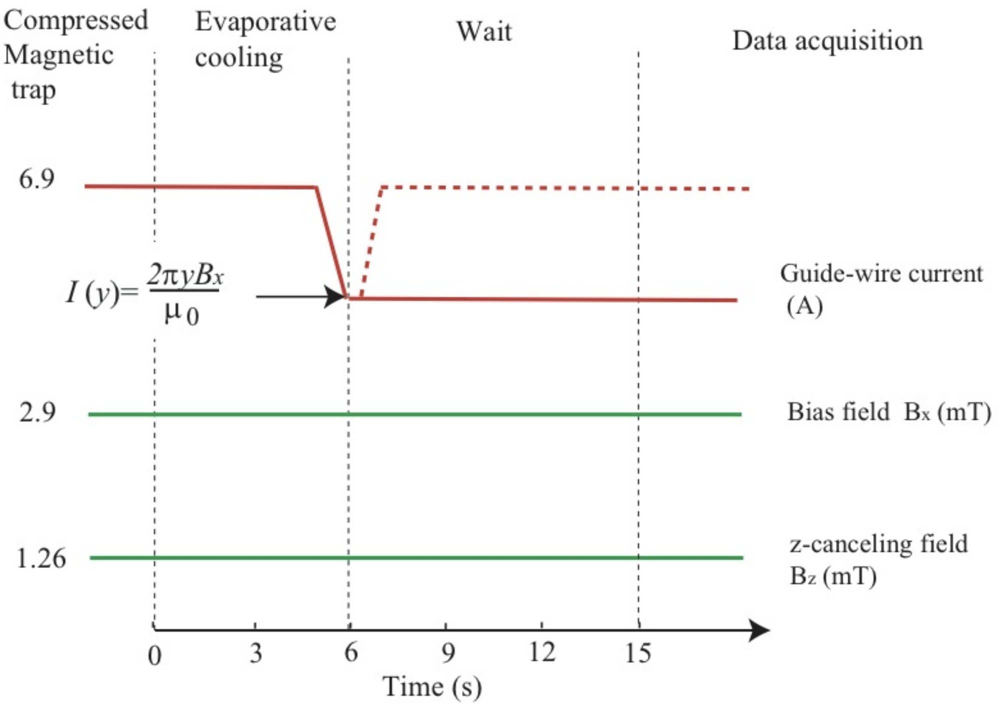

Figure 3.5: Variation of the microtrap fields during evaporative cooling, before counting atoms for a lifetime measurement. The distance from the wire d is set by linearly ramping the current through the guide wire during the last second of RF evaporation while both uniform fields, B_x and B_z, are kept constant.

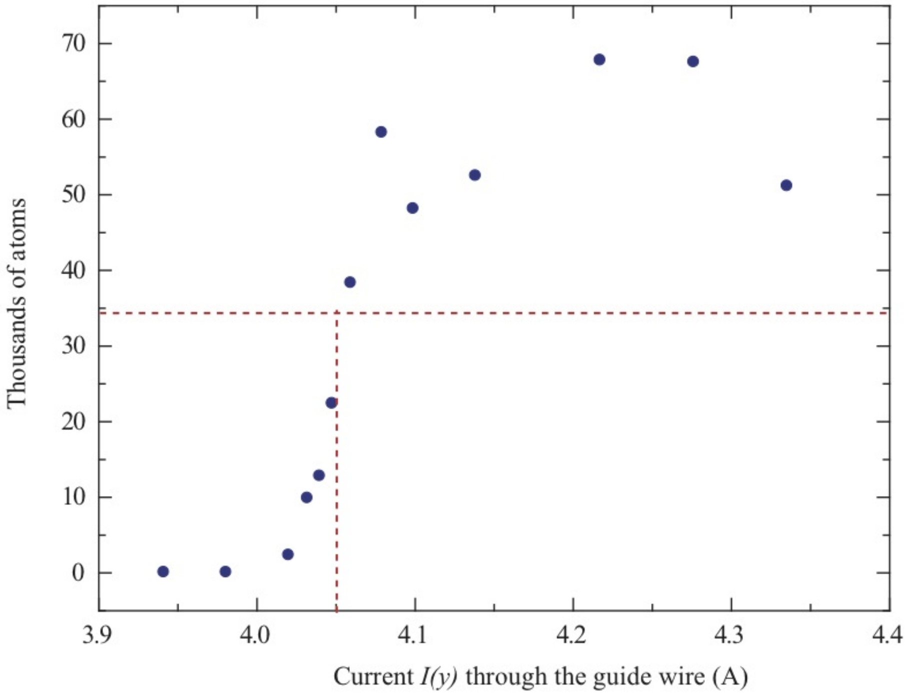

Figure 3.6: Number of atoms versus current through the wire. The blue circles are the number of atoms left inside the magnetic trap after it was pulled towards the wire and then returned to its original position by running 6.9 A again through the guide wire.

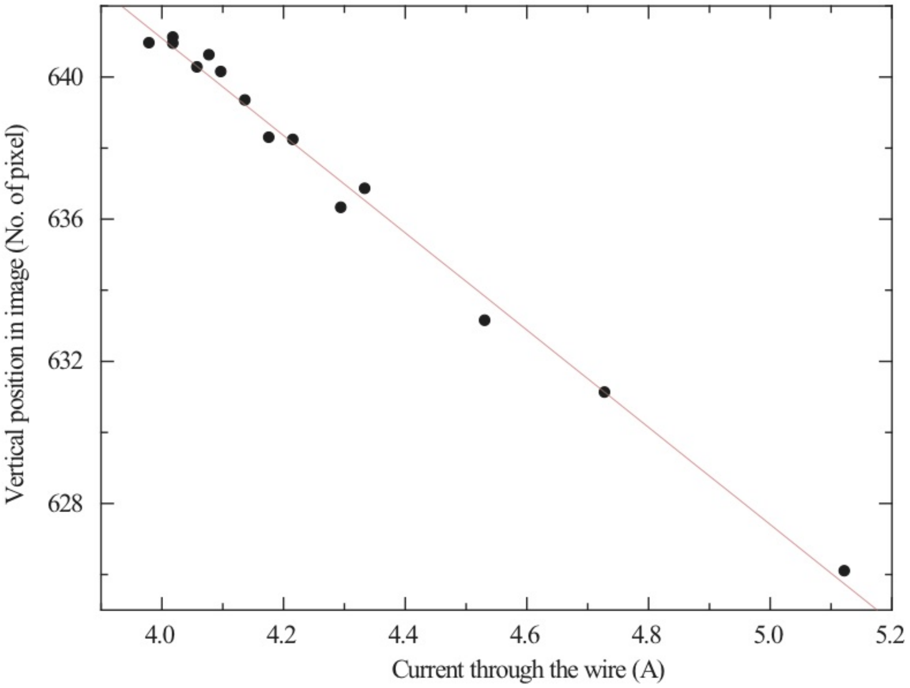

Figure 3.7: The black circles are the vertical position in the images of atom clouds trapped whilst running several currents (lower than 6.9 A) through the wire.

Once a current $I(y)$ is associated to the position of the surface, we look for a reference in the images. To do this, we study the dependence of the position of the atoms with the current through the wire. For these experiments the current was left at $I(y)$ until the atom clouds were imaged, as illustrated in Figure 3.5. In each case, the position of the atom cloud in the image is determined by fitting a Gaussian to the radial (vertical) profile of the atom cloud. Then we can link each current to a position in pixels of the images, finding the linear dependency shown in Figure 3.7, where the position of atoms is plotted against the current through the wire. The pixel along y in which the center of atom clouds for 4.05 A was found is taken as the position of the ceramic surface on the pictures. Measuring the distance from the insulating layer of the wire to the atoms in this manner, gives us an uncertainty of ± 1.4 μm. The distance d from the atoms to the aluminium layer, which is the relevant parameter for our experiments in this chapter and Chapter 4, is this distance plus 10μm, the thickness of the ceramic layer. For example, the atom cloud displayed on Figure 3.3 (a), for which $I = 6.9$ A and $B_x = 2.9$ mT, was trapped at (225 ± 1.4) μm from the conducting surface of the guide wire.

3.4.2 Measuring the spin-flip frequency

Investigating the atom loss rate due to spin flips requires an accurate knowledge and control of the spin-flip frequency. Here I present the method we used to measure this

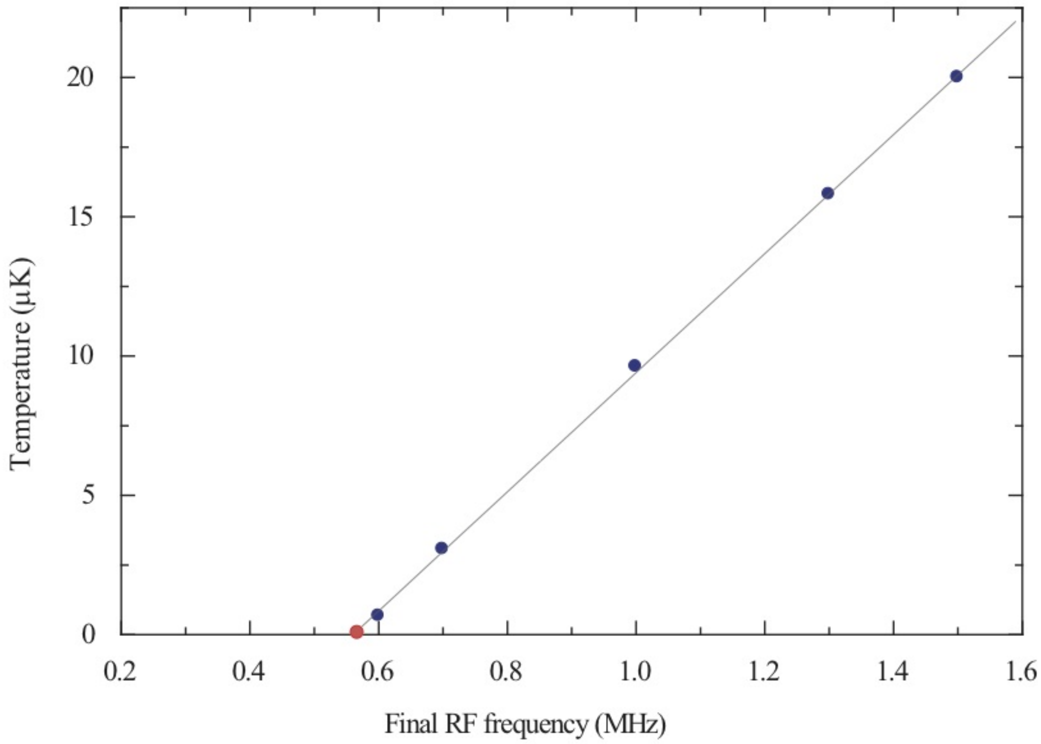

Figure 3.8: One example of the method that we used to measure the spin-flip frequency f_0 of our magnetic trap. The blue circles are temperatures measured for different final RF frequencies on the evaporative cooling ramp and the line is a least squares fit to these data. The red circle is the final frequency extrapolated from the fit, corresponding to f_0= 548 kHz (or B_0=0.077 mT).

frequency.

During RF evaporation, the truncation energy is related to the field B_0 at the centre of the magnetic trap by

$$E_t = \mu_B g_F m_F (B - B_0). \tag{3.41}$$

By substituting the RF-resonant condition given by Equation (2.41) into Equation (3.41), we find that the final RF frequency is related to E_t through

$$E_t = h m_F (f - f_0), \tag{3.42}$$

where the final RF frequency is $f = \frac{1}{h}\mu_B g_F B$ and $f_0 = \frac{1}{h}\mu_B g_F B_0$ is the frequency resonant to spin flip transitions for atoms close to the centre of the magnetic trap. Matching the final RF frequency f with f_0 means zero truncation energy, leading to the expulsion of all atoms from the microtrap. Also, because at low temperatures the field that atoms feel is B_0, we call f_0 the 'spin-flip' frequency.

We measure the spin-flip frequency of magnetic traps by observing experimentally the temperature dependence on the final RF frequency f of evaporative cooling. Final

RF frequency equal to f_0 corresponds to zero energy inside the trap or equivalently, zero temperature. At temperatures around 30 μK and lower, we find that this dependency is linear, as can be seing from the example shown in Figure 3.8. For this measurement, the atoms are confined 225 μm away from the guide wire. The blue circles in Figure 3.8 are the temperatures of atom clouds cooled down to different final RF frequencies. These data are well fitted by least squares fit, the line shown in Figure 3.8. An extrapolation of this fit for the final frequency corresponding to $T = 0$ gives a spin-flip frequency of 548 kHz. In some cases we found that the temperature measured with the lowest possible number of atoms already gives a good estimation of f_0.

3.4.3 Measuring lifetime

To measure the lifetime of the magnetic trap, the atom cloud was transported to the desired distance d from the wire during the last second of evaporation by ramping $I(y)$ and leaving constant the bias field B_x as illustrated by the red line in Figure 3.5. Once cooled at a suitable temperature and desired position, the atom cloud was held for a time between 0 and 9 s as shown in Figure 3.5. This waiting time was limited by the heat dissipation through the wires in the vacuum chamber. To ensure that we measured the mechanism of interest and not collisional loss, we normally waited no longer than 9 s before counting atoms with our absorption imaging system. For each run we took a picture of the atom cloud, followed by an image 500 ms later under exactly the same conditions but without the atoms.

Here we count the atoms as described in Section 2.2.3. We first divide the image of the atoms by the background picture. This division is expected to be one on pixels belonging to regions of the picture with no atoms. It is however, normally ± 5 % off presumably due to variations on the intensity of the imaging beam from picture to picture. To fix this, we re-normalize the image by the average number over pixels in a region with no atoms but close to the magnetic trap. Next, we take the natural logarithm for each pixel in the image to obtain a map of the column density of the atoms in the clouds. Finally, we integrate over the region where the atom cloud appears in the image to determine the total number of atoms.

A measurement of lifetime was completed by counting atoms in identical magnetic traps for several different waiting times. The decay shown by Figure 3.9 is an example of these measurements. For this measurement, the atom clouds were held 29 μm from the guide wire and evaporated by a RF ramp from 13 to 1.7 MHz. The line on the Figure 3.9 is a least squares fit to decay of atom number; the loss rate is given by its slope and the lifetime is τ= 5.1 ± 0.4 s. The uncertainty of our lifetime measurements is given by the error of the slope in the least squares fit.

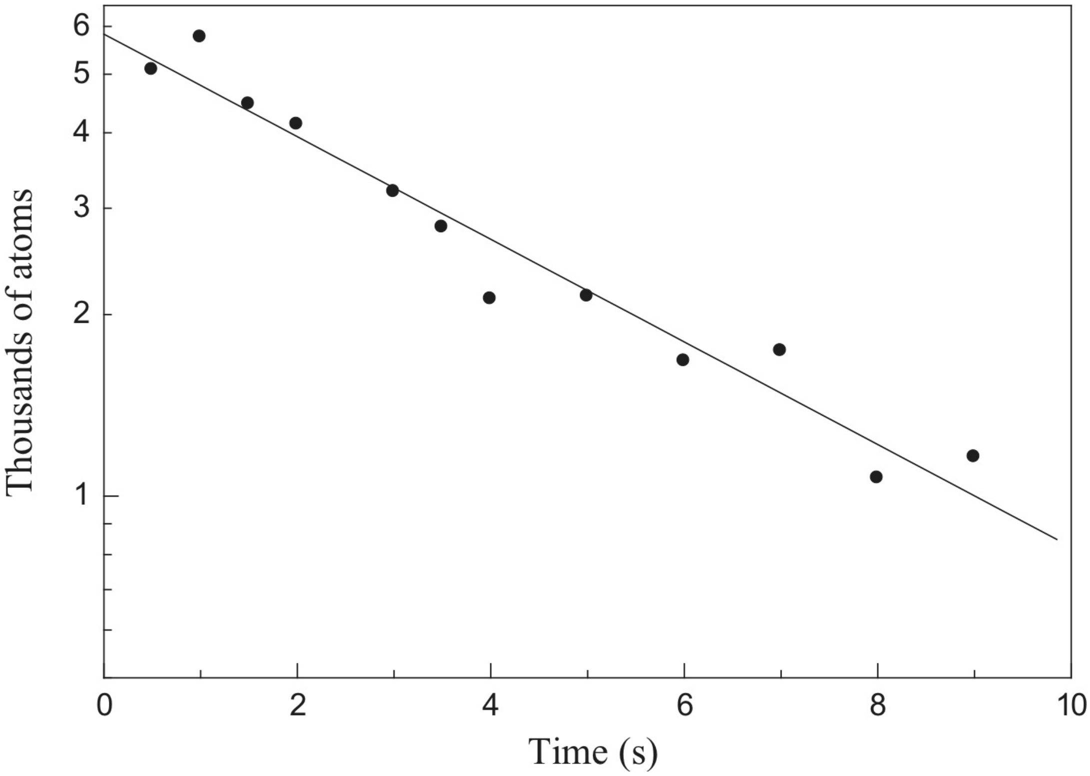

Figure 3.9: Atom number in the microtrap at 29 μm counted after diverse times. Atoms were initially cooled down to 1 μm.

3.4.4 Lifetime dependence on d

We measured the lifetime of the magnetic trap in this way at a variety of atom-surface distances d. We measured lifetimes for two different spin-flip frequencies: 1.8 MHz and 560 kHz. Table 3.1 is a summary of these data, and Appendix B shows in more detail the experimental results. Note that, as predicted by the theoretical limits given by equations (3.28) and (3.40), the lifetimes we measured for 1.8 MHz are longer that those measured for 560 kHz within the same range of d.

f_0 (MHz)	d (μm)	τ (s)	σ_τ (s)	f_0 (MHz)	d (μm)	τ (s)	σ_τ (s)
1.8	27	2.2	0.2	0.56	27	2.5	0.2
	29.4	5.1	0.4		27	2.4	0.1
	35	10.5	0.2		35	5.3	0.2
	54	38.7	2		54	8.6	0.6
	77	73.6	21		54	8.2	0.4
					71	15.1	2
					88	29.4	7

Table 3.1: Measured lifetimes of the magnetic trap for various distances d from the wire and two different spin-flip frequencies. The uncertainty σ_τ is determined by the least squares fit in each case.

Our experimental data for $f_0 = 1.8$ MHz are the green circles in Figure 3.10. For comparison, the black curve plots the lifetime $\tau(d)$ predicted by Equation (3.27) for atoms with spin flip frequency of 1.8 MHz near a planar slab of aluminium at 297 K. It is not expected to fit to our data because our wire is a cylinder, not a slab. The experimental lifetimes could be reasonably expected to be longer than those for a slab because there is more material in a infinite slab than in our guide wire. With our data however, this effect is not evident because the discrepancy between experiment and Henkel's theory is smaller that two error bars in the whole range of d that was investigated. Another comparison between experiment and theory is possible with the full calculation for a cylindrical wire [57]. The blue curve in Figure 3.10 displays this calculation for a 297 K temperature. It is immediate to note that longer lifetimes are predicted for a wire than for an infinite slab of aluminium. This is a sign of the difference in the amount of material included in the two geometries. From Figure 3.10 one can note that our experimental data are closer to the theory for a slab at short distances ($d < 30$ μm), and closer to the wire's theory for distances longer than about 55 μm. These are not significant differences because the discrepancy between our data and either theory is smaller than three error bars in the full range of d that was investigated. From this comparison between our data for $f_0 = 1.8$ MHz and theory, we can conclude that indeed, the atom loss investigated as a function of d is dominated by thermal spin flips. However, these data do not evidently distinguish between the two different theories.

Let us now focus on Figure 3.11, showing our data (red circles) for $f_0 = 560$ kHz as well as the curves corresponding to various theoretical predictions for this spin-flip frequency. The blue dashed curve is the lifetime calculated for a cylinder with the dimensions of our guide wire at 297 K. It predicts lifetimes consistently long compared with our data in the full range of explored distances d. This systematic discrepancy suggests that the wire was heated up by dissipating power whilst running experiments, as we subsequently showed. Section 3.5.5 explains a few measurements that we carried out to find the temperature of the wire during experiments which indicate a rise of 64 K above room temperature. The blue solid curve shown in Figure 3.11 is the calculated lifetime of atoms trapped near a cylindrical wire at 361 K, and the black curve is the calculation for a planar slab at the same temperature. By comparison between our data and the two curves for the two different theories at $T = 361$ K in Figure 3.11 for $f_0 = 560$ kHz, we recover the conclusion made for $f_0 = 1.8$ MHz: our experiments were not sensitive enough to distinguish between a planar and a cylindrical geometry of the thermal body.

Our data lay consistently underneath the curve for the wire at 361 K, suggesting that the wire temperature rose by more than our estimation of 64 K from the temperature response tests. Also, the experimental lifetimes are consistently longer than

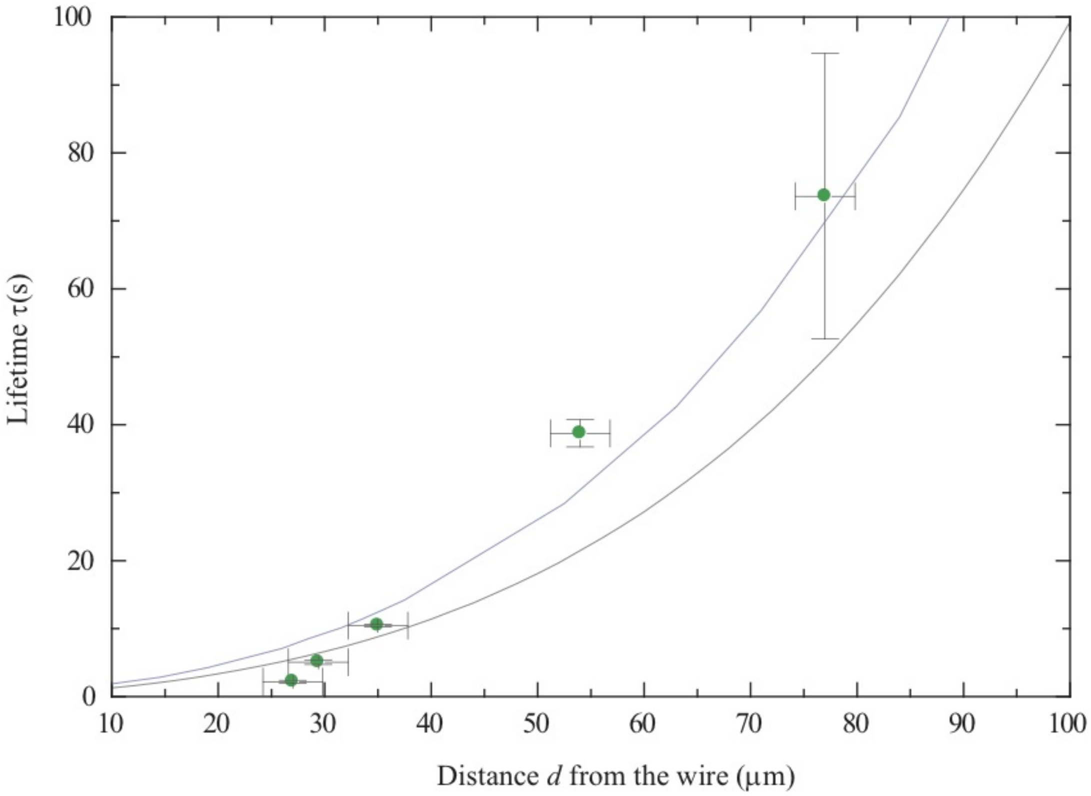

Figure 3.10: Lifetime of the magnetic trap as a function of d. Green circles: lifetimes measured with spin-flip frequency f_0= 1.8 MHz. Black curve: theory by Henkel *et al.* [55] predicting the lifetime of cold atoms coupled to a planar slab of aluminium at 297 K. The blue curve is the by Rekdal *et al.* [57] for a cylindrical wire at 297 K.

those calculated close to a planar slab for the same temperature. However again, given the size of the error bars of our data, we conclude that the experimental data is not accurate enough to reproduce the temperature dependence predicted for the thermal spin flips.

Our experimental data were the first demonstration of the coupling between the spin of cold atoms and the thermal field of a surface as opposed to technical noise. In Section 3.5.4 it is described how we took care of technical noise in both the AF and RF regimes. The AF noise that remained in our magnetic trap produced some residual heating, but did not affect the number of atoms and hence was not a problem for these measurements. RF noise in the currents of the wire would create an atom loss rate proportional to $1/d^2$ and therefore, lifetime proportional to d^2 [94]. The dotted curve in Figure 3.11 shows the expected behavior of the lifetime of atoms as if it was limited by this mechanism. This curve is chosen to pass through an arbitrary experimental point to show the clear discrepancy between what is predicted from spin-flips driven by RF technical noise and what has been observed.

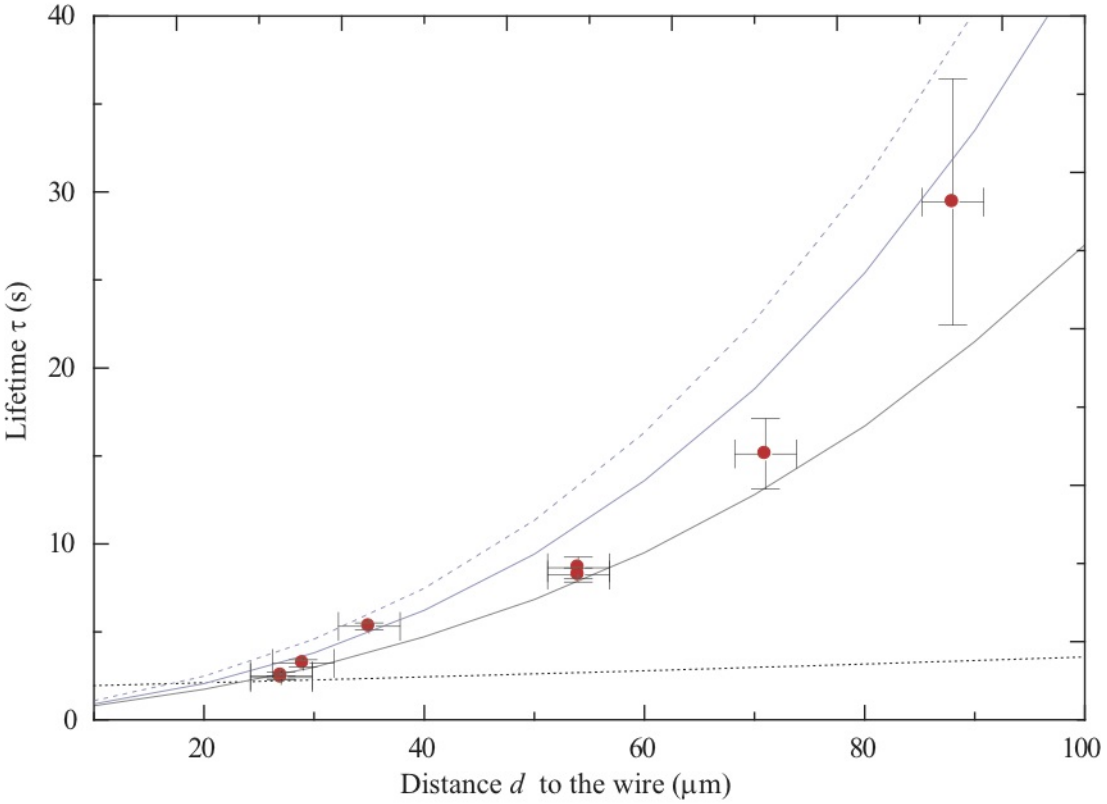

Figure 3.11: Comparison of our results for f_0= 560 kHz with two theoretical models. The red dots are the measured lifetimes of atom clouds at various distances from the surface of the wire. The solid and dashed (blue) curves are lifetimes calculated for atoms near a doubly-layered wire at 297 and 361 K calculated using the theory of reference [57] by P. K. Rekdal *et al.*. The black curve corresponds to the lifetime of the trapped quantum state near a planar slab of aluminium at 361 K. The dotted curve is the lifetime behavior $\propto d^2$ expected from RF technical noise.

3.5 A few experimental considerations

3.5.1 Region of interest

At the time of our experiment, the theory by Henkel *et al.* [55] was already available. This theory provided two useful scaling laws [Equation (3.28)] for atom loss near a planar slab of material in terms of the spin-flip frequency ω_0, the skin depth of the material δ and the distance to its surface d. These scaling laws gave us guidance for our experiments. We expected to observe a change in the dependence of the lifetime by scanning d in a range including the skin depth of the conducting layers of the wire, copper and aluminium, at the measured spin-flip frequencies 1.8 MHz and 560 kHz. These lengths, shown in Table 3.2, fixed the range of d over which we focused our investigations: 27 - 100 μm.

f_0 (MHz)	B_0 (mT)	Material	δ (μm)
1.8	0.26	Cu	49
		Al	61
0.56	0.08	Cu	88
		Al	110

Table 3.2: Skin-depth of copper and aluminium at 300 K for the chosen spin-flip frequencies.

3.5.2 The Casimir-Polder potential in our microtrap

The Van der Waals force attracts atoms to the surface and can be a cause of atom loss by pulling atoms out of their trap. This happens at distances of a few hundreds of nanometers, which is much closer than the distances studied in this thesis.

A neutral atom interacts with the thermal field of surfaces according to the electric dipole Hamiltonian

$$H_e = -\hat{\mathbf{D}} \cdot \hat{\mathbf{E}}(\omega_\kappa), \tag{3.43}$$

where $\hat{\mathbf{D}}$ is its electric dipole moment and $\hat{\mathbf{E}}(\omega_\kappa)$ is the electric field. When the atom is close to the surface compared with $\lambda_0/4\pi$, where λ_0 is the wavelength of its strongest dipole transitions, this interaction is just the Van der Waals force [95]. For Rb this length scale is of nanometers. Further away, the interaction is retarded and follows a different power law from the Van der Waals force. It is called the Casimir-Polder force following the two authors who first calculated it [96]. The first experimental evidence of this potential was obtained by C.I. Sukenik *et al.* [97], who measured the force acting on atoms while travelling across a cavity built with two parallel plates.

For an atom at distance d from a plane surface, the Casimir Polder potential takes the simple approximate form

$$V_{CP} = -\frac{C_4}{d^4}, \tag{3.44}$$

where

$$C_4 = \psi(\epsilon)\frac{3\hbar c\alpha}{32\pi^2\epsilon_0}. \tag{3.45}$$

In Equation (3.45) α is the static electric polarizability of the atoms and c is the velocity of light. $\psi(\epsilon)$ is a numerical factor that is dependent on the dielectric constant ϵ of the material, equal to one for a metallic surface.

The nearest conductive material to atoms in our microtrap is the the aluminium layer of the guide wire. The Casimir-Polder potential of this surface modifies the radial potential of the trap. Figure 3.12 is the potential that the atoms feel in a trap at 27 μm from the aluminium surface, the nearest distance where we measured atom loss rates for this Thesis. Magnetic traps at this distance are formed by running 3.9 A though the guide wire and bias field $B_x = 2.9$ mT. The Casimir Polder potential is the

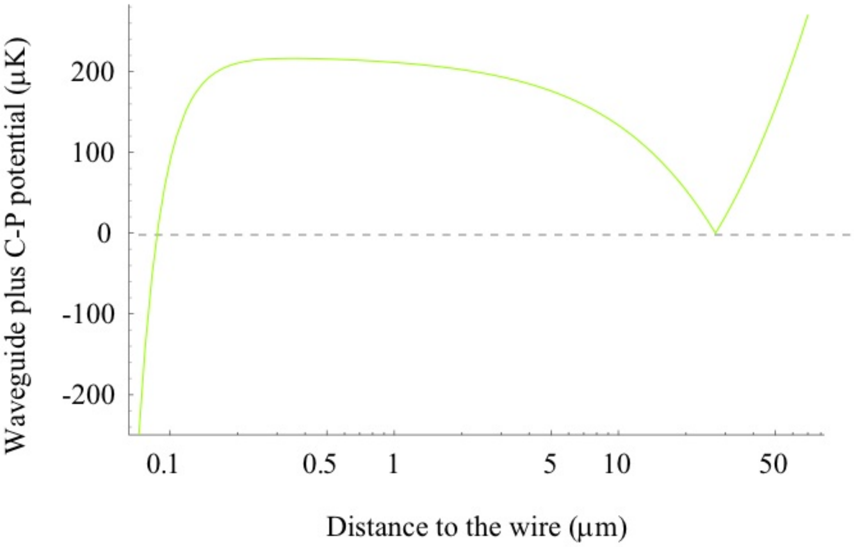

Figure 3.12: Cross section of our microtrap in the radial direction plus the Casimir-Polder potential of a conducting surface. The potential of the microtrap was calculated with a current of 3.9 A through the guide wire and a bias field of 2.9 mT. These parameters bring the microtrap to 27 μm from the aluminium layer of the wire – the shortest distance in which we measured rates of atom loss.

dominant interaction when it cancels with the radial potential of the trap that acts in the same direction but with opposite sign. As can be seen in Figure 3.12, this happens at about 0.1 μm from the conducting surface. The Casimir Polder potential causes atom loss when making the radial trap depth shallower than the temperature the trapped atoms. In the case of the microtrap considered in Figure 3.12, the radial trap depth is reduced from 1273 μK to 220 μK. Because the atoms for these experiments were typically cooled to 6 μK, we can rule out the Casimir Polder potential as an atom loss mechanism in the measurements reported in this thesis.

3.5.3 Adjusting f_0

In Chapter 2 it was mentioned that the offset field B_0 at the center of the trap has two contributions: the uniform field B_z and the field of the end wires at $z = 0$. The latter field is a function of the trap height:

$$B_{\text{end}}(d) = \frac{\mu_0 I}{2\pi}\left(\frac{d - y_i}{A_i^2 + (d - y_i)^2} - \frac{d - y_o}{A_o^2 + (d - y_o)^2}\right), \tag{3.46}$$

where $y_{i(o)}$ is the position of the inner (outer) end wires along y and $A_{i(o)}$ is half of the distance between the end wires with corresponding subindex, see schematic of the atom chip in Figure 2.10.

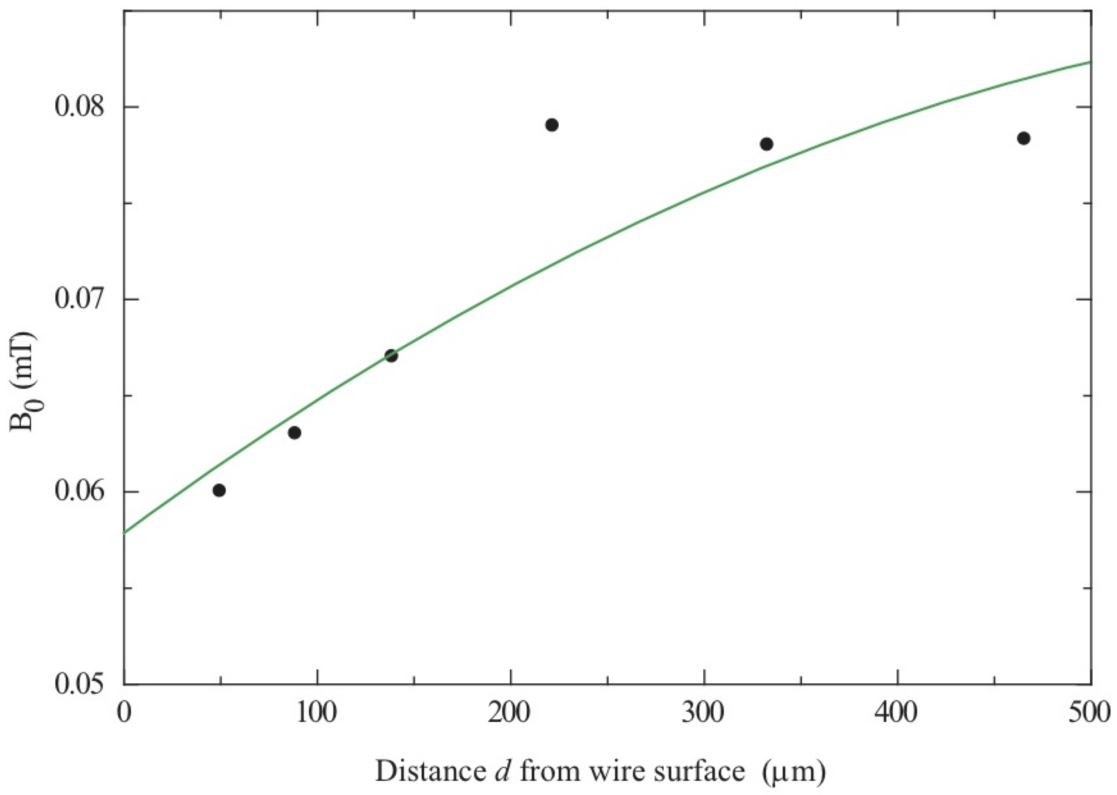

Figure 3.13: Variation of the offset field B_0 as a function of d. The filled circles are values of this field measured for various distances d from the surface of the wire, and the green line is the curve predicted by Equation (3.46).

Now, $B_0(d) = |B_{end}(d) + B_z|$, this dependency is shown in Figure 3.13. The black circles in Figure 3.13 are the experimental values of $B_0(d)$, measured as explained in Section 3.4.2, with 15 A through the end wires and B_z= 0.344 mT. For these points the distance d was varied by changing just the current through the guide wire, whose field has no component along z. The curve is $B_0(d)$ calculated with Equation (3.46).

In order to measure the spin-flip rates versus trap height d with fixed frequency f_0, we compensate for the variation of B_{end} by adjusting the current through the z-coils guided with the theoretical behaviour of $B_0(d)$. Finally f_0 is determined experimentally as described in Section 3.4.2.

3.5.4 Technical noise

Before measuring the spin-flip rates we detected and controlled the technical noise that our experimental was producing. We found sources of atom-decoherence in both the audio frequency (AF) and RF ranges that were generated by mechanical and electronic oscillations in different parts of the experiment.

Magnetic fields tuned to multiples of the trap frequency generate trap shaking that excites atoms from one trap mode to a higher one, finally causing a heating rate of the whole cloud [98, 99]. This heating rate can give atoms energy greater than the trap depth, inducing atom loss in consequence. Our compressed magnetic trap has radial and axial frequencies of 838 Hz and 30 Hz respectively, both in the AF range. We originally found the magnetic trap had a heating rate of about 2 $\mu\mathrm{Ks}^{-1}$, which was traced to two sources of AF noise in our experiment. One of them, the biggest source, was mechanical oscillations which in turn were originated in two different ways. Firstly, we found that by attaching the RF antenna to the top of the vacuum chamber through small pieces of the sorbathane (a foam rubber used for mechanical damping), helped to decrease the heating rate. Which means that this antenna had been oscillating. Secondly, the wire of the ion gauge was oscillating in an obvious manner and part of it was sitting on the optical table. We also solved this problem with sorbathane, by making a damping base that supports this wire at the part in contact with the optical table. With these precautions, the heating rate was reduced to 1 - 0.5 $\mu\mathrm{Ks}^{-1}$.

The second source of AF noise, causing the residual heating rate in the microtrap, are oscillating magnetic fields produced by AC noise in the field sources. Our current driving circuits have an inherent rms noise of 0.01 mV or lower, equivalent to less than one part in 10^5 of their output signal. However, this is amplified by the quality of the input signal. The poorest case is the guide wire, whose source is a Thurlby Thandar Intruments (TGA 1230) waveform generator that produces a slow drift (in the bandwidth 20 Hz - 300 kHz) with 0.53 mV rms, one part in 10^3 of its DC signal. After passing through the corresponding current driving circuit, this noise is injected into the experiment as an oscillation with 20 μA rms, one part per 10^6 of the current through the guide wire. Our magnetic trap is typically switched on for no longer than 15 s and hence, this heating rate can heat up atoms up to about 11.3 μK during one run. This means no atom-loss contribution due to the heating rate since in the (shallowest) radial direction our compressed trap is typically 516 μK deep.

In order to check for technical noise in the RF range, we scanned the spin-flip frequency measuring it as explained in Section 3.4.2. Close to 1 MHz, we found a dramatic drop in the lifetime of atom clouds even at large distances from the wire ($d \geq 200$ μm). In order to search for the source of this noise, we used the RF antenna connected to a spectrum analyzer as a detector and found a parasitic oscillation with a 1-1.5 MHz, varying frequency in one of the circuits of the optical shutters. We removed these circuits from their rack, which was shared with other electronics of the experiment. Additionally, we filtered the noise by adding a capacitor to the problematic circuit. After these changes, the parasitic signal was too small to be detected with the antenna. Nevertheless, the atoms seemed to be a better detector. The decay rate was still surprisingly big when f_0 was in the noise frequency range. Therefore we decided to measure the lifetime of traps with spin-flip frequency far from resonance with these oscillations: 560 kHz and 1.8 MHz.

3.5.5 Temperature of the guide wire

A complete comparison between our results and the theory presented in references [55, 57, 90] would demand knowledge of the temperature of the guide wire during experiments, so we can calculate the correct scaling factor $(n_{th}+1)$ required to account the blackbody radiation into the decoherence rates.

The temperature of the guide wire was not monitored during the measurements of lifetime. However, after that we attached a thermocouple type K (Chromel/Alumel junction) to the surface of the guide wire once we broke vacuum for the inclusion of a new chip into the vacuum chamber. The head of the thermocouple was weighted down with a block of Poly Tetra Fluoro Ethylene (PTFE) with a piece of Macor resting on it. Its wires were glued with vacuum compatible epoxy (Bylapox 7285) to a Macor block sitting on one side of the atom chip as shown in Figure 3.14 (a).

Under vacuum, we monitored the temperature response of the guide wire while applying continuous currents with typical experimental values. Figure 3.14 (b) shows curves of the temperature change ΔT as a function of time for 4, 5, 6 and 8 A. The base temperature at zero current was 297 K, the room temperature. The guide wire was burned before we could take more precise measurements, such as reproducing the ramp sequences run during spin-flip experiments. Fortunately the curves displayed in Figure 3.14 (b) produce an adequate estimate of the temperature reached by the guide wire during experiments. Figures 2.14 and 3.5 show the typical sequence followed by the current through the guide wire. When the magnetic trap was switched on, the guide-wire current was stepped from 0 to 8 A. Then the current was linearly ramped down to 6.9 A during 500 ms for the compressed trap stage. Evaporation typically lasted for 6 s; during the last second the current was ramped to $I \simeq \frac{2\pi B d}{\mu_0}$. This current was maintained for a waiting time of between 0 and 9 s until data acquisition.

A good estimation of the current versus time is therefore given the 7 A points displayed in Figure 3.14 (b), interpolated from the response curves as detailed in Appendix C. The red circle in Figure 3.14 (b) is the temperature rise after 15 s of running at 7 A: $\Delta\mathrm{T} = 64$ K. This represents the highest temperature to be read when considering the factor $(n_{th}+1)$ to include the blackbody radiation into the theoretical rates.

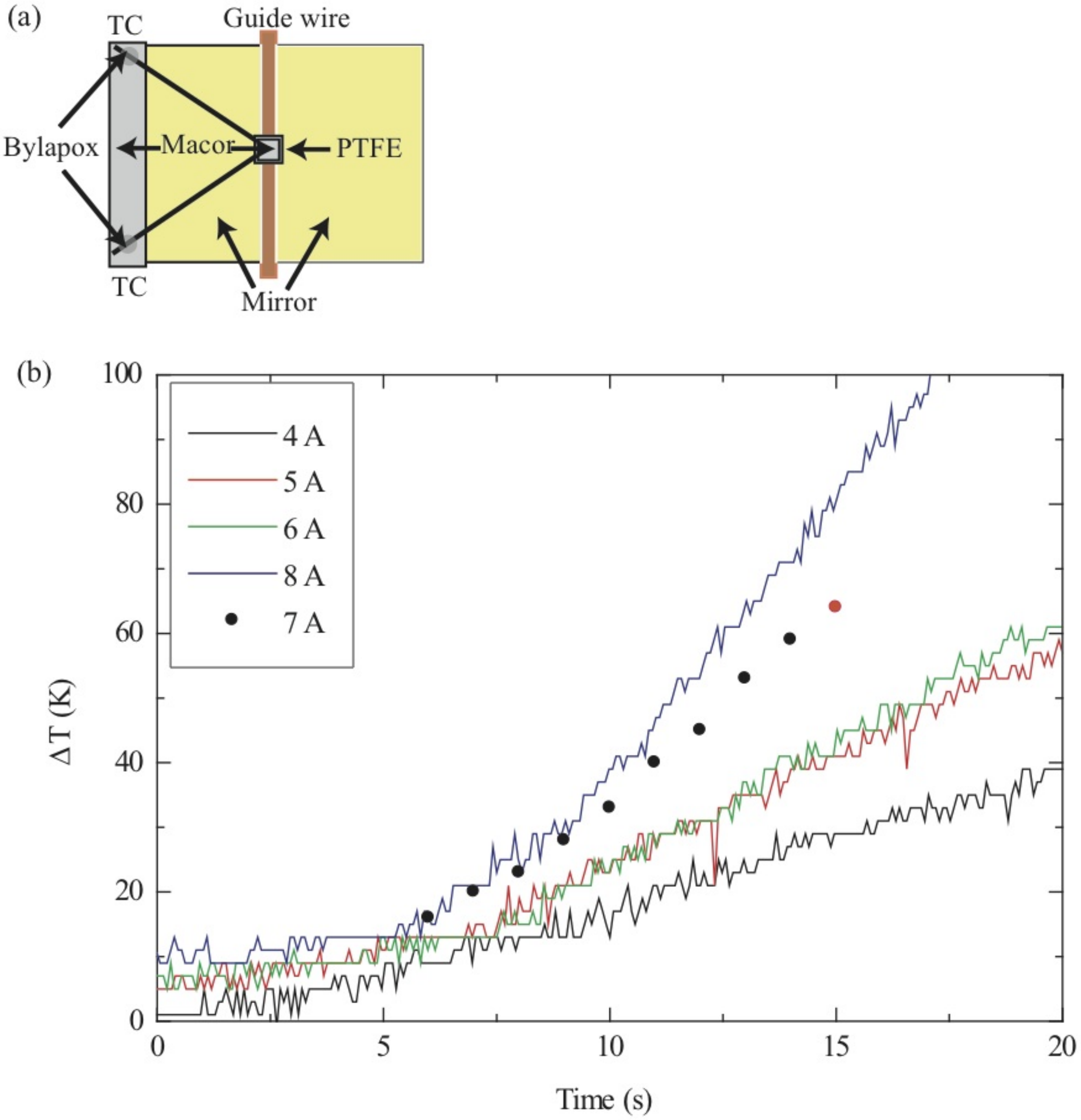

Figure 3.14: Temperature response of the guide wire to several currents. The figure shows (a) the method in which the thermocouple was attached to the guide wire, and (b) the wire temperature as a function of time. Colored curves are experimental measurements; solid circles are interpolations from these data.

3.6 Conclusion and outlook

The data presented in this chapter were the first evidence of the atom loss mechanism through thermally driven spin flips near the surfaces of atom chips [56]. We provided an experimental test for the calculations made by Rekdal *et al.* [57] for thermal spin flips near a cylindrical wire.

This theory was extended to include spin flips near thin films of conducting and superconducting surfaces [90], leading to important theoretical results to guide us towards a better design of future atom chips. The theory has recently extended to atoms trapped near thick superconductors [100], predicting lifetimes several orders of magnitude longer than the lifetime of the trapped states near thin wires of conductors.

Chapter 4

Lumps

A real wire has imperfections of shape and composition. Both of these cause the current density to depart from the ideal of uniform flow along the length of the current carrying wire. Consequently, in addition to the circular field created by the ideal current, the real current also generates field components parallel to the direction of the wire. The spectrum of these components is governed by the order and size of the imperfections in the wire. These anomalous, axial fields create corrugations at the bottom of the guiding potential whose amplitude is typically between one part in 10^3 and 10^4 of the wire's circular field.

In microtraps, atoms are trapped at tens of micrometers from current carrying wires. Depending on the structural purity of the wire, at these distances the corrugations of the guiding potential can be sufficient to break clouds of cold atoms or condensates into lumps as shown in Figure 4.1. This makes it difficult to achieve well defined condensates near the surface of an atom chip and can compromise a number of desirable applications. The series of images displayed in Figure 4.1 is taken of atom clouds cooled to the same temperature but localized at different distances d from the aluminium surface of the guide wire. It illustrates the fragmentation of atom clouds in our microtrap. From Figure 4.1, it is clear how at the long distances (around 100 μm) corresponding to the higher images, the magnetic trap holds a single atom cloud. This is changed as the microtrap is pulled towards the wire, to finally break the cloud into three smaller lumps in the image for 16 μm, the lowest in Figure 4.1.

The atom-chip community has recently put a considerable effort into understanding and solving this problem for future experiments. The atom chip group of Tübingen [99, 101], the MIT-Harvard group [102] and our group [58] initiated the study of the fragmentation in microtraps near wires. The first publication with evidence of atom cloud fragmentation was published by Leanhard *et al.* [102], although it was not clearly reported until [99, 58]. The origin of the anomalous potential was tracked down using

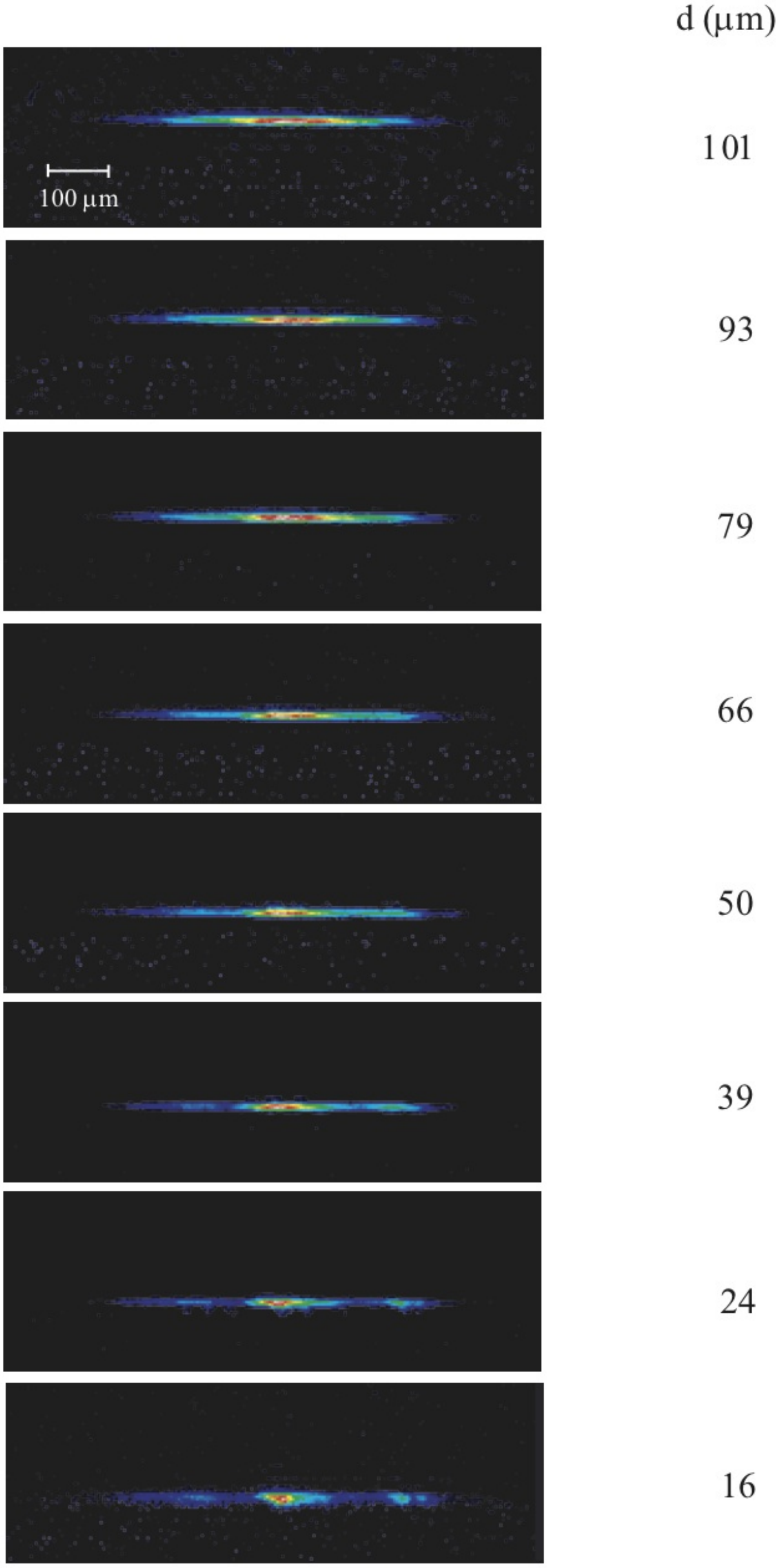

Figure 4.1: Absorption images illustrating the fragmentation of atom clouds when pulled towards the surface of our guide wire. Here d is the distance from the aluminium surface of the wire.

different tests. One was conducted by probing the surface of the same wire with atoms confined by magnetic traps and dipole traps; atom clouds inside the magnetic traps were fragmented while atom clouds inside dipole traps were not fragmented in the same location [103]. Another test was to reverse the direction of the bias field, which had the effect of turning the minima of the corrugations into maxima and viceversa. This proved that the field causing the potential corrugations has alternating sign [101]. Our work, which is subject of this chapter, showed that the anomalous field that is responsible for fragmentation decays with the distance from our guide wire as a modified Bessel function of the second kind $\mathrm{K}_1(2\pi y/\lambda)$ [58]. This decay is expected from the field created by a meandering current flowing along the axis of the wire. Although we do not have enough evidence to make a definitive statement, we think that the origin of these deviations of the current are imperfections in the internal structure of the guide wire.

Further experimental and theoretical investigations carried out in Orsay, France [104] showed that the current deviations can be caused by the imperfections in the surface and edges of the wire. Their work demonstrated that the corrugations in the trapping potential are diminished by improving the quality of the wires, which is directly related to the techniques used to manufacture them [81]. The atom chip group of Heidelberg, Germany probed the D.C. magnetic field near a wire fabricated with lithography [82]. They verified that, as previously shown by the Orsay group, the method of construction of the wires is of fundamental relevance to the quality of the resulting field. In a more recent publication [105], this group combined the techniques used for detection of the anomalous field together with the micron-scale manipulation of cold atoms on atom chips to design a magnetic field detector whose compromise between spatial and field resolution overtakes any previous technological accuracy.

4.1 Fragmentation in our microtrap

To study the fragmentation of our magnetic trap, we observed atom clouds held at several distances d from the wire, in the range 16 - 100 μm which is suitable for a number of applications.

The atom clouds displayed shown in Figure 4.1 were prepared similarly to the samples of atoms cooled for the spin-flip experiments. This is by using the same cooling and trapping sequence described in Chapter 2 but with a modification in the RF-evaporative stage. Here, I summarize from the start of magnetic trapping. About 10^7 atoms in the $5S_{1/2}, |F=2, m_F=2\rangle$ state of ^{87} Rb are loaded to a Ioffe-Pritchard microtrap. The magnetic trap is initially created at 1.3 mm from the guide wire by running 8 A through the guide wire, applying 1.0 mT of bias field in the x-direction and driving 15 A through the four end wires. The field due to the end wires at the center of the trap is partially cancelled by a uniform field of 0.6 mT along z. Next, the magnetic trap is compressed by linearly ramping the current down to 6.9 A and increasing B_x and B_z to 2.9 mT and 1.1 mT respectively over 500 ms. This brings atoms down to 225 μm from the surface of the guide wire with radial and axial frequencies 840 and 26 Hz. The collision rate at this point is 55 s^{-1}, appropriate for efficient evaporative cooling. Evaporation is then carried out over 6 s, from 13 MHz to around 2.8 MHz. This sequence cools atoms down close to 7 μK, a suitable temperature for our experiments because the anomalous potential of our wire is between 0.5 and 12 μK within the studied range of d.

The atom density profiles plotted in Figure 4.2 have been extracted from the atom clouds trapped at eight different distances from the wire whose images appear in Figure 4.1. Each profile was normalized by the total count number along the integrated region. The top (green) curve shown in Figure 4.2 is the axial profile of an atom cloud trapped at 101 μm from the surface of the wire, this distribution is well approximated by a Gaussian. Additional structure appears progressively in curves corresponding to the profiles of atom clouds trapped at shorter distances from the wire. The lower (black) curve in Figure 4.2 is the axial atom density distribution of an atom cloud 16 μm away from the wire. In this curve, the Gaussian distribution is almost completely screened by three peaks corresponding to three minima in the potential induced by the anomalous field ΔB_z. These peaks remained at the same position throughout several months of measurements.

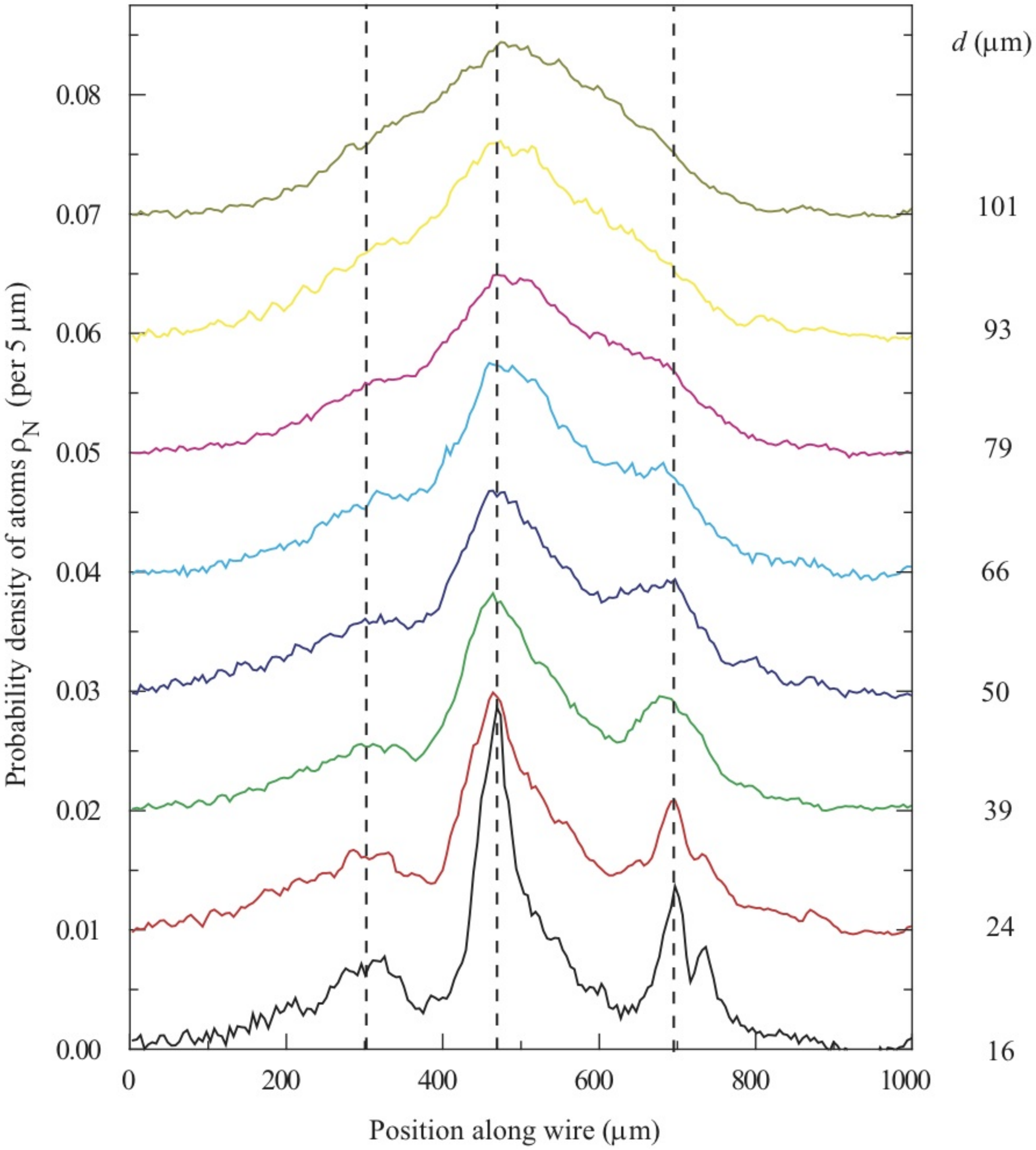

Figure 4.2: Axial profiles of atom clouds trapped in the range $d = 16 - 101$ μm. An offset of 0.01 was included between subsequent curves for clearness of the graph.

4.2 Extracting potentials from absorption images

Originally the fragmentation of atom clouds near wires was thought to be caused by stray magnetic fields parallel to the axis of the wire [99]. To investigate the origin of these fields, we extracted the potential holding the atom clouds directly from their images.

4.2.1 Cold atoms trapped in a harmonic potential

It is still useful to define a temperature for magnetically trapped ensembles of atoms because they reach a steady state through oscillations and elastic collisions. Equilibrium is reached after the thermalization time. Once thermalization is reached, one can assume that the probability of finding an atom with energy ϵ is given by the Gibbs distribution [88]

$$w = Ae^{-\epsilon/k_BT} = Ae^{-k/k_BT}e^{-u(z)/k_BT} \tag{4.1}$$

where A is a normalization constant, $k = \frac{1}{2}k_BT$ is the average kinetic energy per atom and T is the temperature of the atoms, appropriately defined in the next few paragraphs. Here, $u(z)$ is the potential that is confining the atoms along z, the axial direction of our Ioffe-Pritchard trap.

Because the kinetic energy k is constant, the atom density is proportional to the Boltzmann factor,

$$\rho(z) \propto e^{-u(z)/k_BT}. \tag{4.2}$$

If the trapping potential $u(z)$ is a harmonic oscillator, $\rho(z)$ follows the Gaussian distribution

$$\rho(z) = \frac{1}{\sigma\sqrt{2\pi}}e^{-\frac{u(z)}{k_BT}} = \frac{1}{\sigma\sqrt{2\pi}}e^{-\frac{z^2}{2\sigma^2}}, \tag{4.3}$$

with variance

$$\sigma^2 = \langle z^2 \rangle = \frac{1}{\omega^2}\frac{k_BT}{m}. \tag{4.4}$$

Our absorption imaging system enables us to measure the atom density in the Ioffe-Pritchard trap, integrated along the x-direction as function of y and z, the column density $\rho_x(y, z)$ with the frame of reference shown in Figure 4.3 (a). Together with Equations (4.3) and (4.4), the imaging system provides us with a method to measure the temperature of atoms on the imaging plane from a single picture of the magnetic trap in situ. This requires just one absorption image of the atom cloud while the magnetic trap is switched on, together with a previous knowledge of the trap frequency, which we have.

Because we are in search of small magnetic fields along the axis of the trap, we

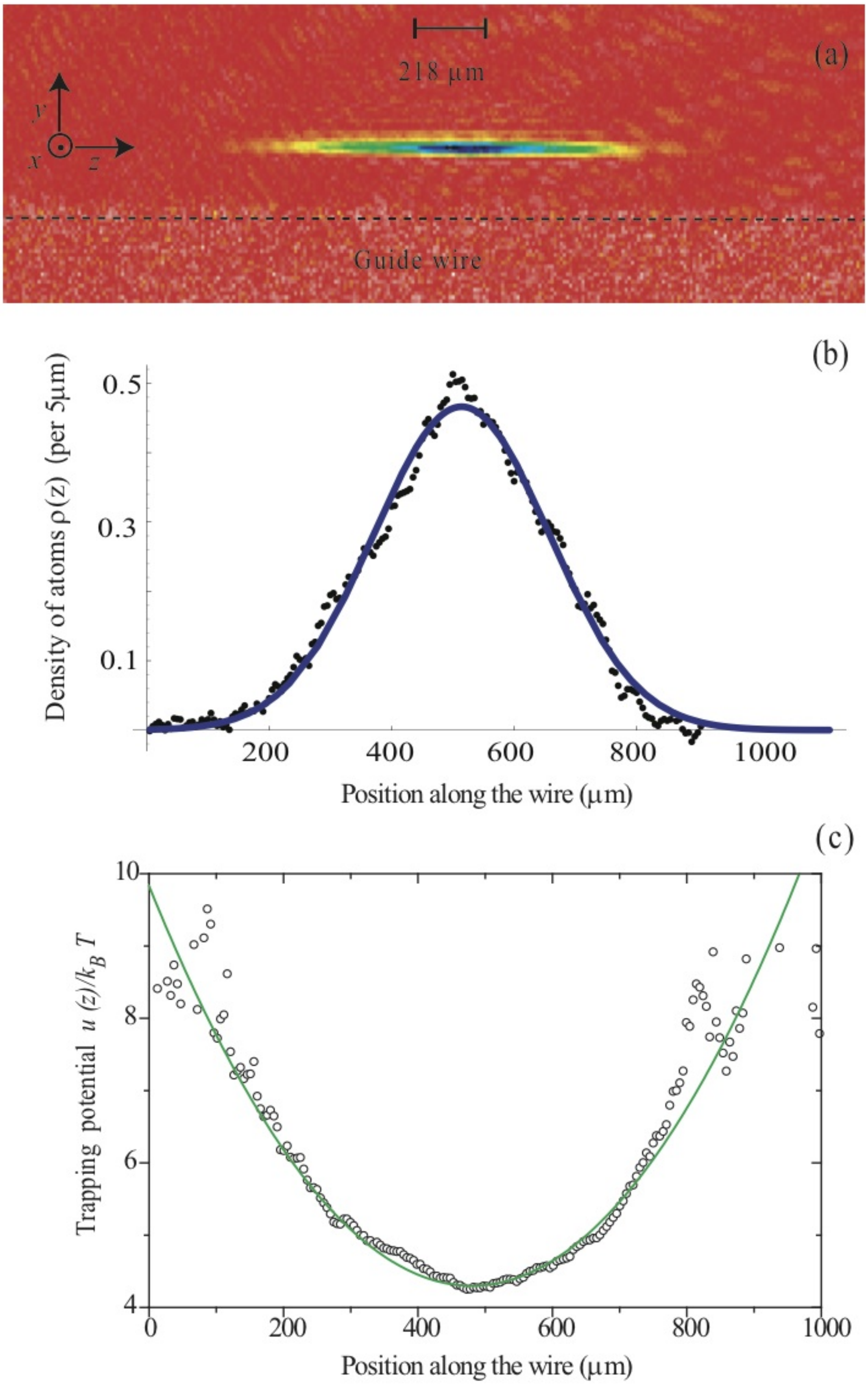

Figure 4.3: Extraction of the relative potential u(z)/k_BT from an absorption image of atoms in the magnetic trap. (a) is an absorption image of an atom cloud cooled down to 5.8 μK and placed at 101 μm from the surface of the wire. (b) shows its axial profile (solid circles) and a Gaussian fit (blue curve) which enabled us to determine the temperature of atoms. (c) shows the logarithm of the profile in (b) after being normalized (open circles) and a quadratic function (green curve) fitted to these data points. We take this curve as the axial potential u(z)/k_BT.

focus on the column density at fixed height: $\rho_x(d, z) \equiv \rho(z)$, where d is chosen to coincide with the center of the cloud. With the image processing described in Section 2.2.3, we obtain $\rho(z)$ per pixel, where the pixel size along z is 4.95 μm, see Figure 4.3 (b). For each z, $\rho(z)$ is related to the trapping potential through Equation (4.3). Thus the trapping potential is inferred by applying the logarithm to both sides of Equation (4.3),

$$\frac{u(z)}{k_B T} = -\log\left[\rho_N(z)\right], \tag{4.5}$$

where $\rho_N(z)$ is the atom density normalized to the total number of atoms counted along z. Therefore, in order to extract the trapping potential $\frac{u(z)}{k_B T}$, we need to normalize the density extracted in each pixel of the absorption image and then apply the logarithm function to it.

Figure 4.3 illustrates the extraction of the trapping potential $\frac{u(z)}{k_B T}$ with an example. The image in Figure 4.3 (a) shows an atom cloud trapped at 101 μm from the surface of the wire. This distance is set by keeping the bias field constant at 2.9 mT and linearly decreasing the current of the guide wire from 6.9 to 5 A during the last second of evaporation (from 13 to 2 MHz) as illustrated in Figure 3.5. The black dots shown in Figure 4.3 (b) are the density of atoms in the cloud along its axis, taken directly from the absorption image. By fitting a Gaussian [blue curve in Figure 4.3(b)] to $\rho(z)$ and inserting the axial trap frequency $f_\text{a} = 26$ Hz into Equation (4.4), the temperature of atoms in this cloud is measured to be 5.8 μK.

The trapping potential $\frac{u(z)}{k_B T}$ is obtained by applying the logarithm function to each density plotted in Figure 4.3(b), after being normalized to the total number of atoms counted along the whole profile. These are the open circles shown in Figure 4.3 (c). The green curve is a parabola fitted to these data. One can see that this harmonic oscillator potential is appropriate to describe the trapping potential $\frac{u(z)}{k_B T}$ because the temperature of atoms should be confirmed by using the relation

$$u(z) = \frac{m\omega z^2}{2k_B T}, \tag{4.6}$$

that must hold for every position z along the wire. We see that this is indeed the case as the temperature of this atom cloud obtained with Equation (4.6) is 5.8 μK, the same as the temperature measured with the Gaussian.

Note that, in order to determine the temperature of atoms with a single absorption image, the magnetic trap is required to be switched on during the imaging exposure time. Our absorption imaging system is designed to picture atoms whose quantization axis is aligned with a uniform magnetic field in direction $-x$ as explained in Section 2.2.3. If atoms are imaged whilst confined by the magnetic trap, their quantization

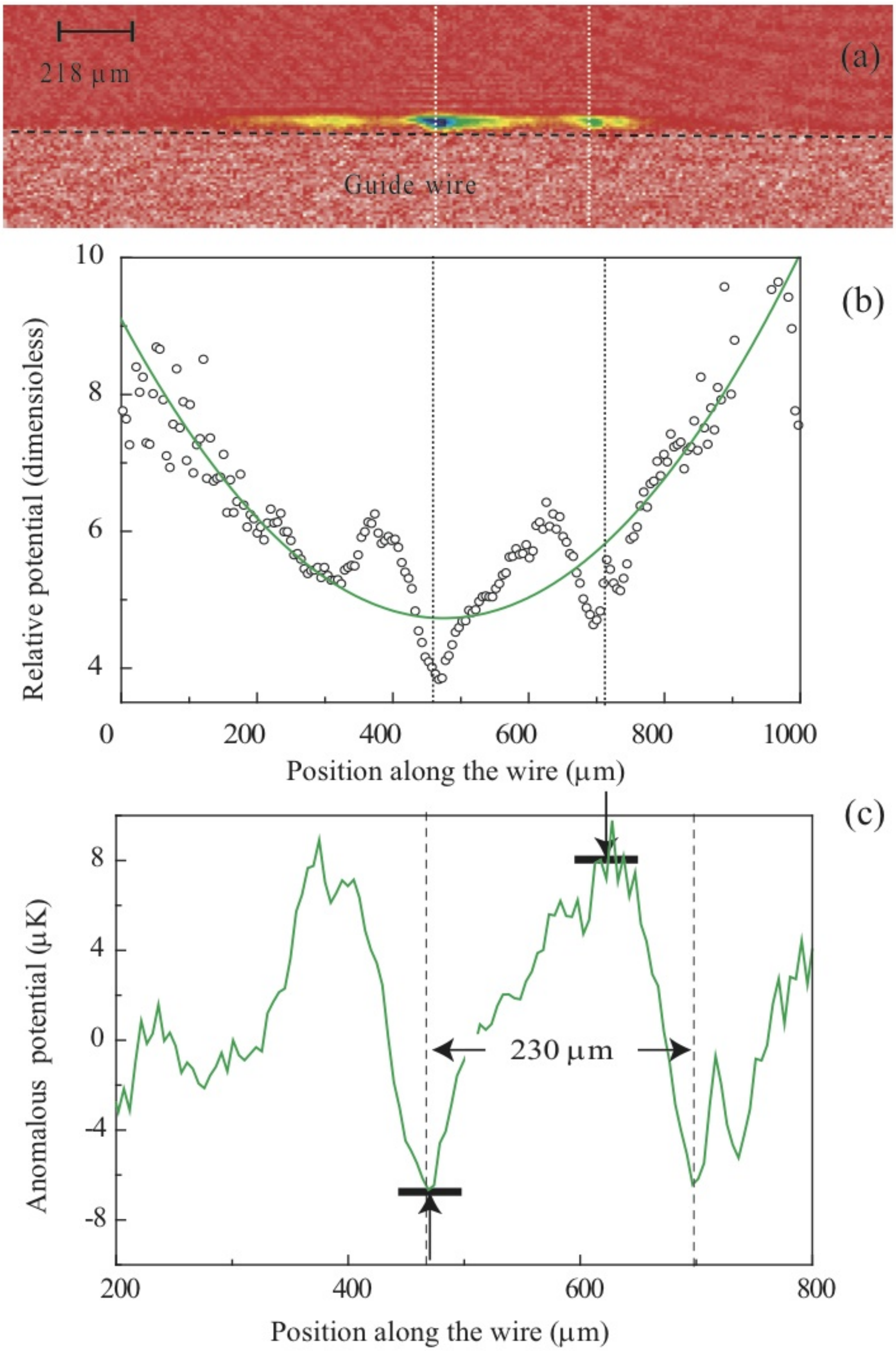

Figure 4.4: Data analysis to extract $u_A(z)$ from the absorption images. (a) absorption image of an atom cloud in a microtrap at 16 μm from the wire's surface. The open circles in (b) are the potential $u(z)$, measured in each pixel along the main axis of the trap and the green curve is the best fitted, harmonic oscillator potential. (c) shows $u_A(z) = u(z) - \frac{1}{2}m\omega^2 z^2$ once subtracted from the trapping potential in (b).

axis has components in the three spatial directions. This makes it hard to interpret absorption images to obtain the absolute atom density because the transition matrix elements depend on the field direction. In order to calibrate the atom number read in images with the magnetic trap switched on, we took several images of atom clouds 15 ms after being released from the magnetic trap. These images were alternated with pictures of atom clouds inside the magnetic trap. The ratio of atom number counted with the magnetic trap on and off remained approximately constant in all cases at 0.56. Besides the information for temperature measurements is fully contained in relative changes of the probability density of atoms. Thus there was no need to correct the atom number for the data analysis.

4.2.2 Corrugations in the harmonic potential

We detected the anomalous potential $u_A(z)$ when atom clouds were at distances shorter than 101 μm from the surface of the wire. Figure 4.4 (a) shows an absorption image of an atom cloud at $d = 16$ μm. This is the shortest distance from the aluminium layer for which we could image atoms without crashing the cloud onto the wire. The presence of the anomalous potential is evident in this picture because, instead of displaying a single atom cloud as expected if $u(z)$ was harmonic, the atom cloud on Figure 4.4 (a) is distributed among three lumps along the axis of the magnetic trap.

The trapping potential holding this atom cloud is given by the open circles in Figure 4.4 (b). In addition to the harmonic trap, we see a large oscillatory potential, which is due to ΔB_z, an unexpected magnetic field added to the axial component of the trap. Most of the anomalous potential is observed in the range z = 200-800 μm along the wire. The apparent structure at the edges in Figure 4.4 (b) results from applying the logarithm to the background signal of the absorption image. The green curve shown in Figure 4.4 (b) is the parabola that best fits the experimental data. This curve was chosen to pass through center of the potential oscillations. The fitted parabola gives a temperature of 7.8 μK. The anomalous potential $u_A(z)$ created by ΔB_z was inferred by subtracting this parabola from the potential $u(z)$,

$$u_A(z) = u(z) - \frac{1}{2} m\omega^2 z^2. \tag{4.7}$$

The anomalous potential we measured at 16 μm from the wire is displayed in Figure 4.4(c). From this graph, we were able to directly measure the distance between the two main lumps $\lambda = 230 \pm 10$ μm, the characteristic length of the corrugations in the potential. We also were able to measure the peak-to-peak amplitude U_A= 13 μK from Figure 4.4 (c) as indicated by the arrows on the graph. This amplitude is equivalent to an alternating axial magnetic field of 97×10^{-7} T. The measured anomalous field is about 5×10^3 smaller than the radial magnetic field of the wire at this distance.

4.3 Dependency of ΔB_z on the distance from the wire

We repeated the measurement of the amplitude $U_A(d)$ for atom clouds trapped at the eight distances from the wire shown in figures 4.1 and 4.2 to investigate the dependency of the anomalous field ΔB_z with d. The experimental results are summarized in Table 4.1.

Height (μm)	Temperature (μK)	$U_A(d)$ (μK)	$U_A(d)$ ($\times 10^{-7}$ T)	$U_{3.7}(d)$ ($\times 10^{-7}$ T)
16	7.8	13	97	97
24	7.8	10	75	72
39	7.8	7.5	56	51
50	7.8	4.1	41	36
66	7.0	3.3	25	21
79	6.4	2	15	12
93	6.1	1.5	11	9
101	5.8	0.5	4	3

Table 4.1: Summary of experimental results probing the D.C. field near our guide wire. The temperatures were measured by fitting a parabola to the harmonic part of the potentials and using Equation (4.6). The uncertainty in the distance to the wire is ± 1.4 μm, the same as in spin flip experiments. For the peak-to-peak amplitude $U_A(d)$, we chose the error to be equal to ± 1.5 μK, the amplitude of the potential at $d = 93$ μm.

To obtain the data shown in Table 4.1, we deduce the anomalous potential $u_A(z)$ from the absorption images as described in Section 4.2.2 for each one of the eight investigated distances. The curves resulting from this analysis are displayed in Figure 4.5. These potentials are regularly spaced. We were able to observe two full oscillations along the major axis of the trap in all cases. The spacing $\lambda = 230 \pm 10$ μm, showed no significant variation with d. The peak-to-peak amplitude $U_A(d)$ of these oscillations decreased with increasing d as can be noted from values tabulated on Table 4.1. Its uncertainty was taken as ± 1.5 μK, the amplitude measured for $d = 93$ μm.

In order to see how $u_A(z)$ varies with distance d from the wire alone, we arbitrarily chose a current of 3.7 A, corresponding to atom-wire distance $d_{3.7}$ =16 μm and scaled all the $u_A(z)$ to it. This was carried out by multiplying each $u_A(z)$ by the factor 3.7/I. Figure 4.6 shows how $u_A(z)$ depends on the position of the atoms along the wire and their distance to its surface. This plot used Mathematica to interpolate $u_A(z)$ between the eight heights where we measured it.

To investigate the origin of ΔB_z, we now focus on the decay of the peak-to-peak amplitude $U_A(d)$ and search for a model to explain its behaviour.

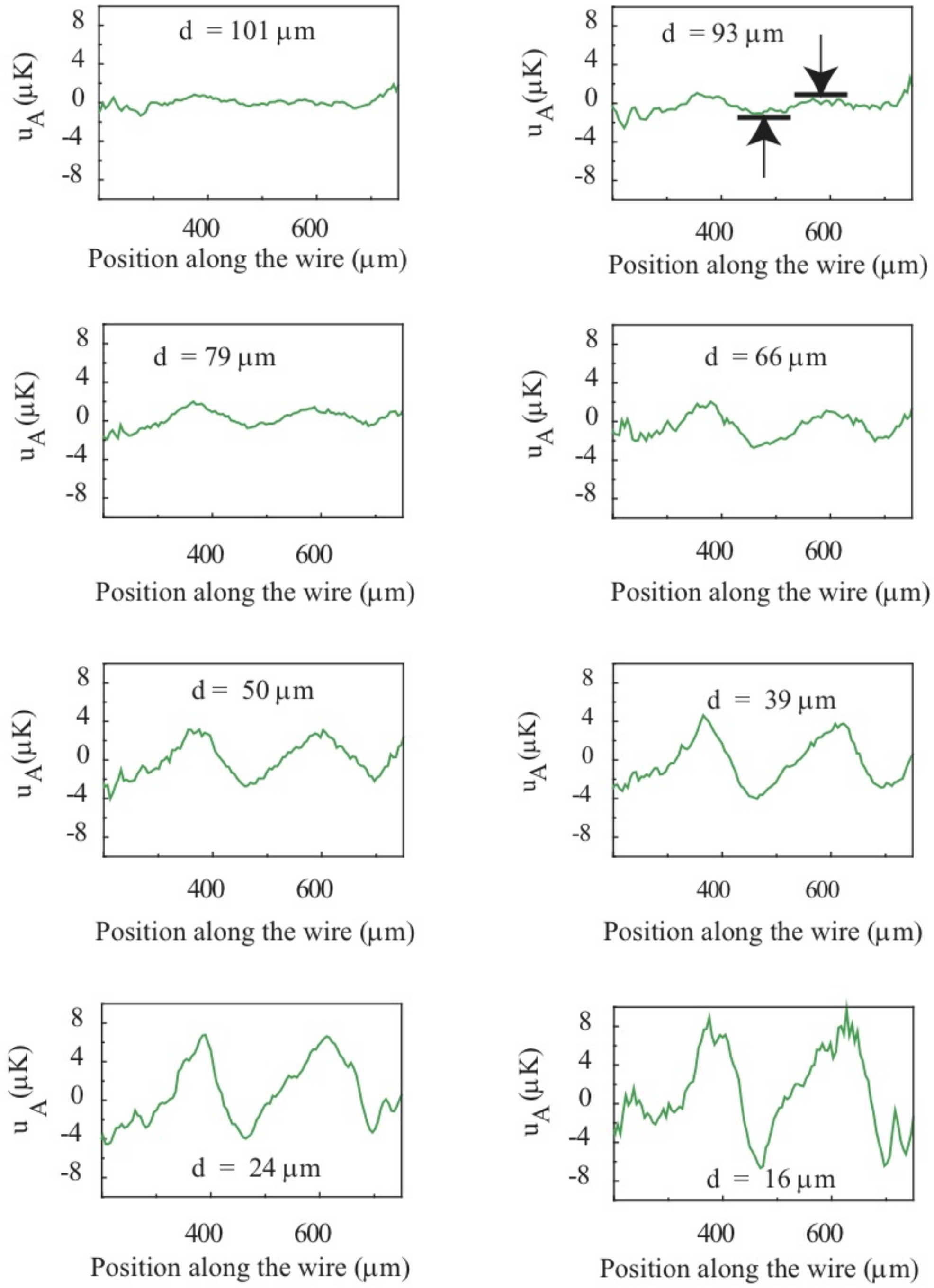

Figure 4.5: The anomalous potential u_A(z) extracted from the images for the eight studied distances d. The arrows in the $d = 93$ μm graph indicate the peak-to-peak amplitude chosen as the error bar in our measurements of $U_A(d)$.

4.3.1 Fitting to a power-law model

The data labelled as $U_{3.7}(d)$ in Table 4.1, $U_A(d)$ for the eight heights fixed to 3.7 A, are represented by the blue circles in Figure 4.7. It is obvious that a power law, which would be a straight line in this graph, could not describe this data.

The red curve in Figure 4.7 shows a power-law function $U_A(d) = Cd^{-q}$ fitted by

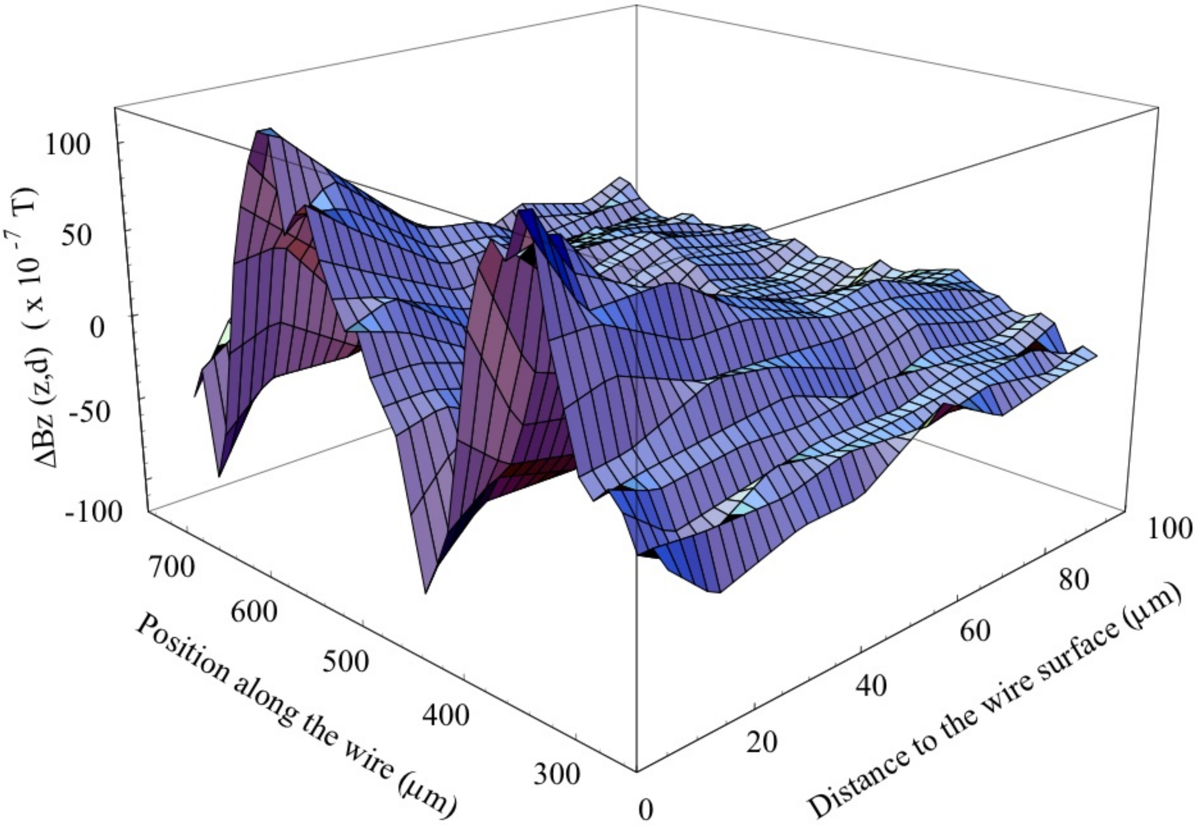

Figure 4.6: Map of the anomalous field for a constant current of 3.7 A through the guide wire.

least squares to our data for in the range d = 66-101 μm, leaving the constants C and q as fitting parameters. For this fit, the optimum values are $C = 2$ T and $q = 3.3$, with a $\chi^2 = 4.2$ and 2 degrees of freedom. The story becomes different if we fit a power-law to our data obtained for the entire range of d in which we did experiments. This is shown by black curve in Figure 4.7, which has $C = 0.2$ mT and $A = 1.07$, with $\chi^2 = 54.3$ and 6 degrees of freedom. We found that adding an offset δ to d, so the fitted function has the form $U_A(d) = C(d + \delta)^{-q}$, as an additional fitting parameter of the power law helped to minimize χ^2. In which case $C = 20$ mT and $q = 2.08$ for an offset $\delta = 30$ μm, giving $\chi^2 = 15.12$ with 5 degrees of freedom. This fitting corresponds to the dotted curve in Figure 4.7.

Note that the same decay was studied by Kraft *et al.* [101], whose data were reasonably fitted by a power law for the range restricted to d=80-109 μm. Our data, over a more extended range of d, makes it clear that a power law does not describe very well the decay of the anomalous field. Moreover, the curve that best fits our data, represented by the dotted curve in Figure 4.7, suggests that the amplitude $U_A(d)$ and hence ΔB_z, is governed by the distance from a point inside the wire and not from its surface.

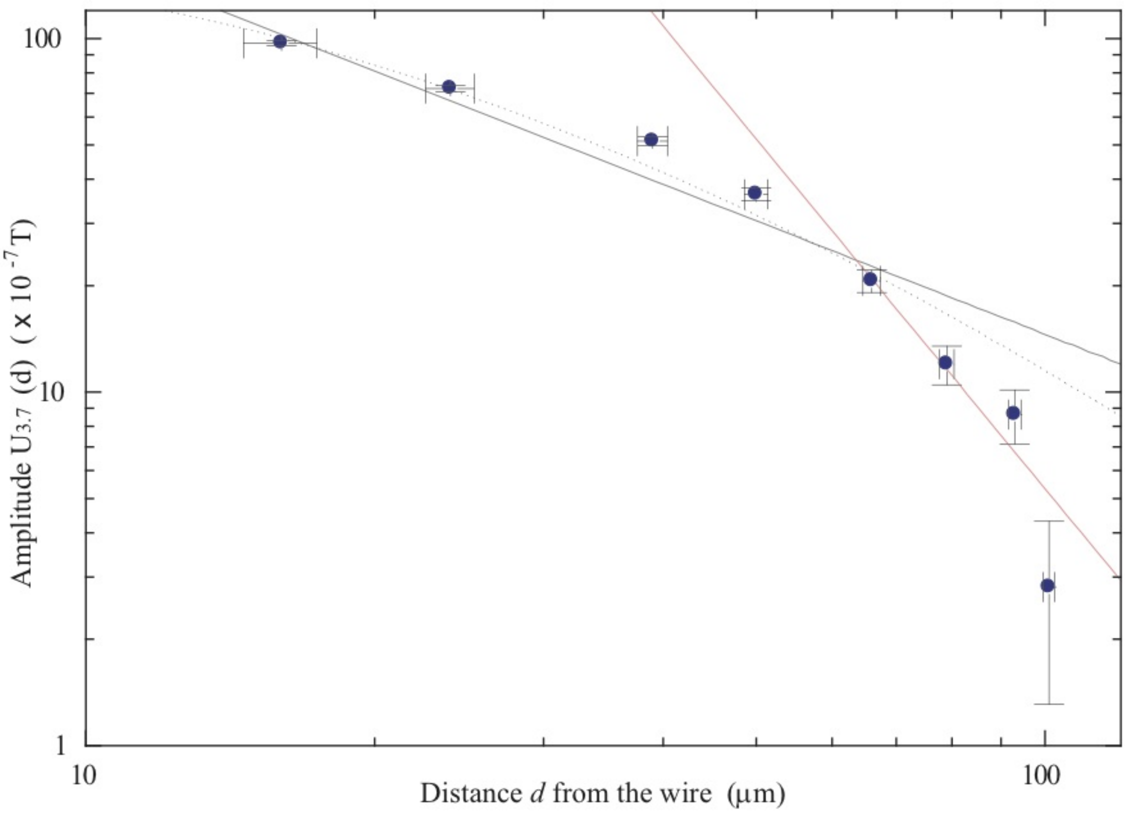

Figure 4.7: Our experimental data $U_{3.7}(d)$ (blue circles) in comparison with a power law. The red curve is a least squares fit to the experimental data within the range d= 66-101 μm with a power law function. The black curve is the same fit but in the full experimental range, d= 16-101 μm. The dotted line is a fit including an offset $\delta = 30$ μm in the power-law fit.

4.3.2 Exponential decay

At first thought, one might expect the anomalous field to decay exponentially with the distance to the wire. Consider a magnetostatic potential oscillating along the wire (along z) with amplitude a and wave number k_0,

$$\varphi = a \cos k_0 z. \tag{4.8}$$

Let us consider a planar wire as illustrated in Figure 4.8, forgetting for a moment that our guide wire is a cylinder. Outside the wire, the potential φ is required to satisfy Laplace's equation $\nabla^2\varphi(x, y, z) = 0$ with the boundary condition (4.8) at the surface ($y = 0$). Both are satisfied if $\varphi = a \cos k_0 z e^{-k_0 y}$ meaning that, outside the wire, the field φ decays exponentially with y. This potential produces the anomalous magnetic field,

$$\Delta B_z = -\frac{\partial \varphi}{\partial z} = a k_0 \sin k_0 e^{-k_0 y}. \tag{4.9}$$

With this simple analysis in mind, we fitted to our experimental data the exponential function $U_A(d) = Ce^{-kd}$, where C and $k = \frac{2\pi}{\lambda}$ are constants. In Figure 4.9,

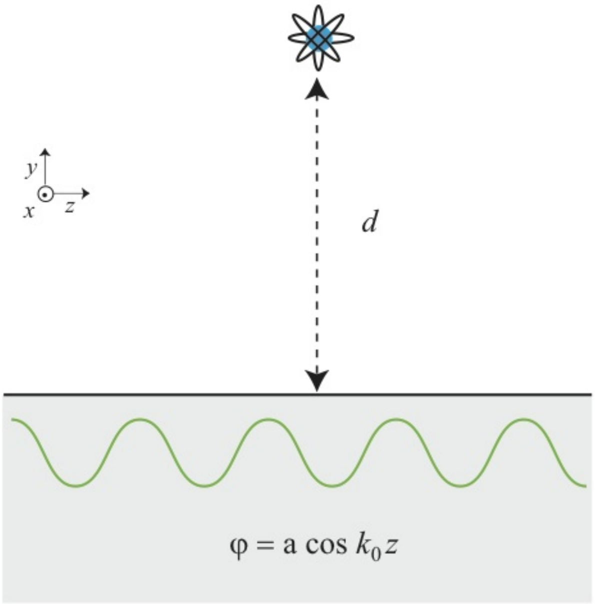

Figure 4.8: Hypothetic system that would yield exponential decay of the anomalous field ΔB_z of the Ioffe-Pritchard trap.

the blue circles are the eight measured $U_A(d)$ (scaled to 3.7 A) and the line is an exponential function, fitted to these data using C and λ as fitting parameters. The best fit gives $C = 177$ nT and a decay distance of $\lambda = 190\ \mu$m. The χ^2 parameter of this fitting is 3.2 with 6 degrees of freedom, which is close to the characteristic distance observed between lumps. However, a better theory should take into account the cylindrical structure of the wire, which we do in the next section. Then, we find that the decay of ΔB_z is not quite exponential, but rather behaves as a Bessel function.

4.3.3 A meandering current

In this section I show that a sinusoidal current with period λ produces a field proportional to $K_1(2\pi y/\lambda)$, a modified Bessel function of the second kind. I also show that this model accurately reproduces the behavior of the anomalous potential we measured with cold atoms.

Consider a steady current I flowing along the axis of the wire and following a path given by the vector

$$\mathbf{s}(x', y', z') = (a \cos kz', 0, z'), \tag{4.10}$$

where a is a constant and $k = 2\pi/\lambda$. According to the Biot-Savart law, the differential field element created by this current is

$$d\mathbf{B}(x, y, z) = \frac{\mu_0}{4\pi} \frac{I d\mathbf{s} \times \mathbf{R}}{R^3}, \tag{4.11}$$

where I is the current through the wire, $d\mathbf{s}$ is the differential path element and $\mathbf{R} =$

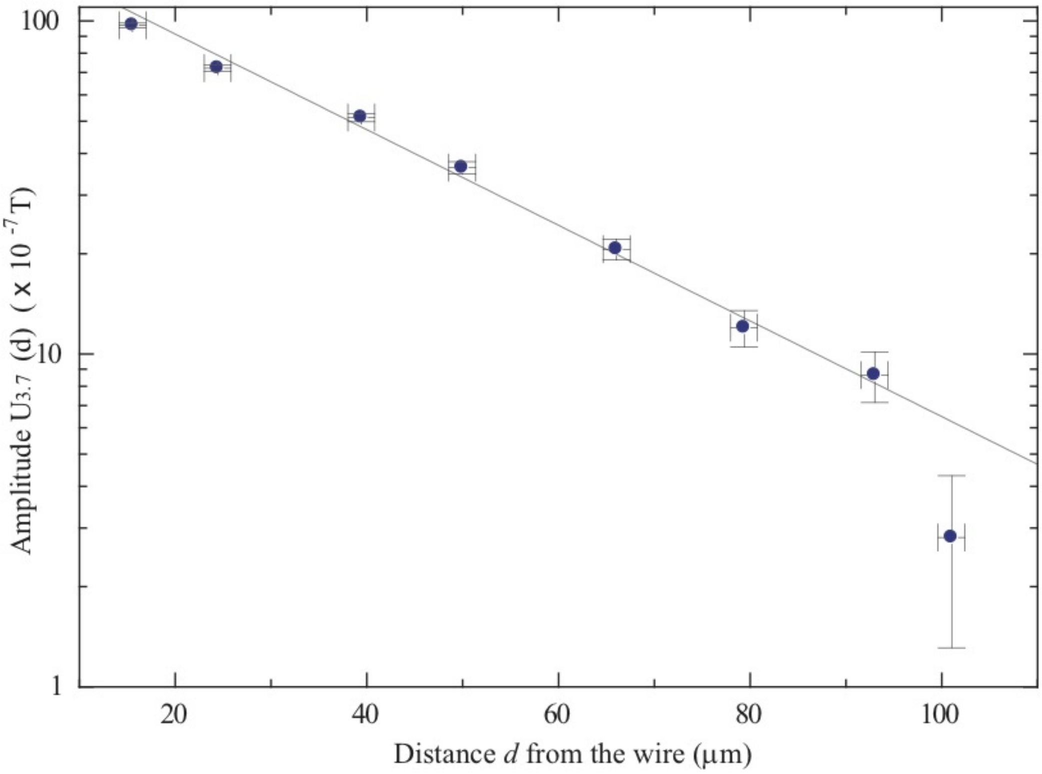

Figure 4.9: The anomalous field for fixed 3.7 A current (blue circles) in semilog scale are well fitted by a straight (black) line, suggesting an exponential decay.

$\mathbf{r} - \mathbf{s}(x', y', z')$ with $\mathbf{r} = (x, y, z)$ being the position of the atoms. Figure 4.10 displays a schematic of the model. The z-component of this field at the position (x_0, d, z_0) is

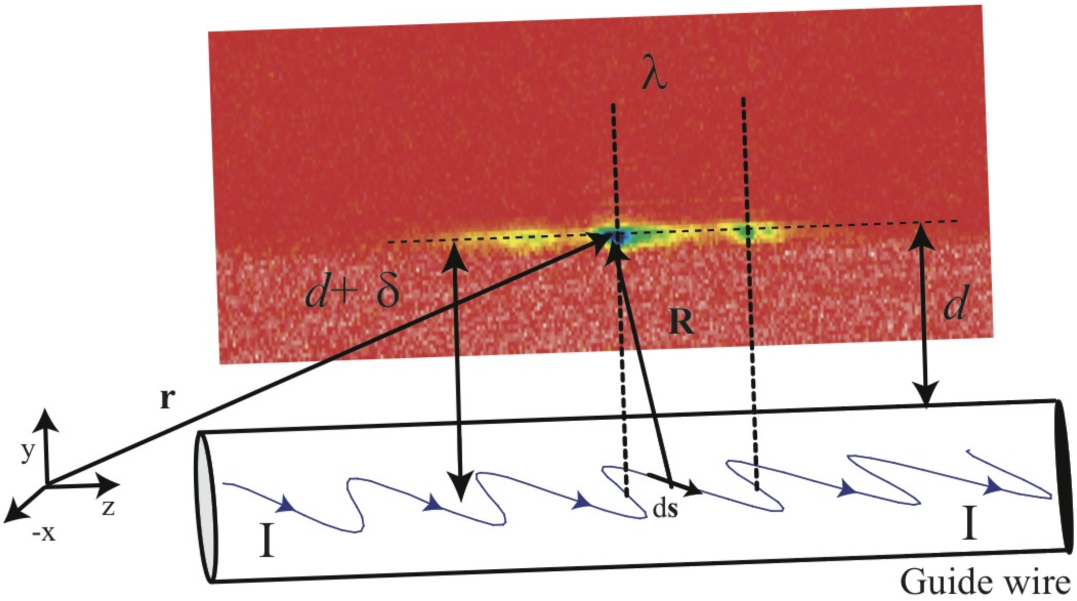

Figure 4.10: Model in which a current with a sinusoidal path gives origin to the anomalous field $\Delta\mathbf{B}_z$

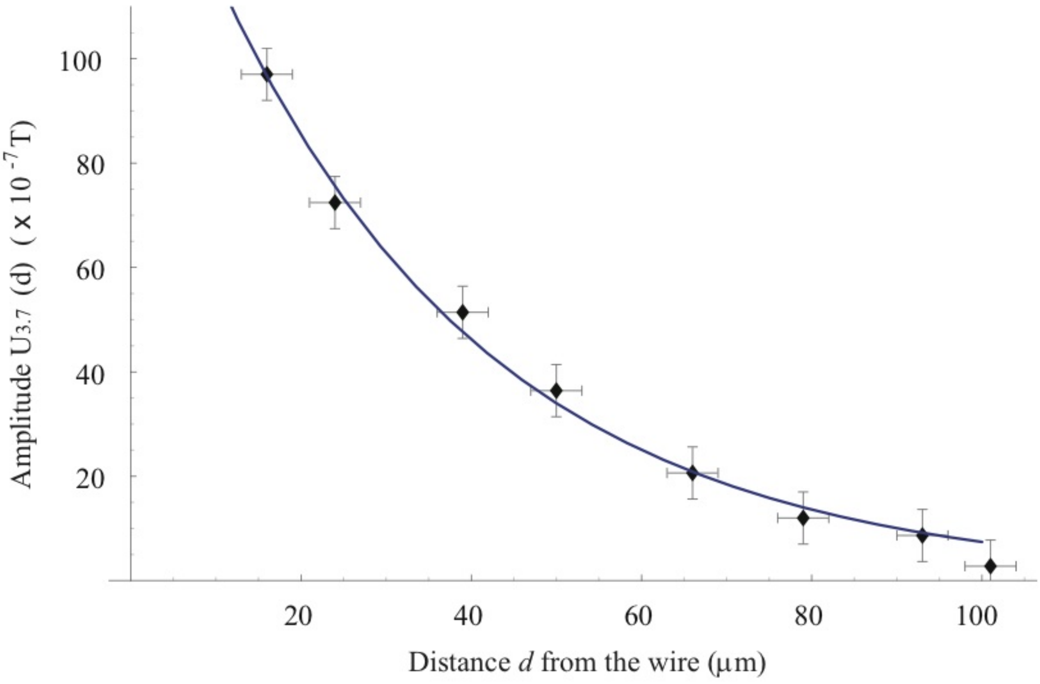

Figure 4.11: Amplitude of the anomalous field along the range d=16-101 μm. The filled circles are experimental points and the curve is a Bessel function fitted to these data.

given by

$$B_z = \frac{\mu_0 Iyak}{4\pi}\int_{-\infty}^{\infty}\frac{\sin kz'dz'}{[(a\cos kz' - x_0)^2 + d^2 + (z'-z_0)^2]^{3/2}}. \tag{4.12}$$

Let us place the atoms directly above the wire, where $x_0 = 0$ and let $a << d$. Then Equation (4.12) becomes

$$B_z = \frac{\mu_0 Idak}{4\pi}\int_{-\infty}^{\infty}\frac{\sin kz'dz'}{[d^2 + (z'-z_0)^2]^{3/2}}. \tag{4.13}$$

By making the change of variable $\eta = z' - z_0$ in Equation (4.13), the z-component of the field created by the meandering current can be written as [1]

$$B_z = \frac{\mu_0 Idak}{4\pi}\int_{-\infty}^{\infty}\frac{(\sin k\eta\cos kz_0 + \sin kz_0\cos k\eta)d\eta}{[d^2+\eta^2]^{3/2}}. \tag{4.14}$$

The integral in Equation (4.14) can be done analytically, yielding [106](formula 9.6.25)

$$B_z = \frac{\mu_0 Iak^2}{2\pi}\mathrm{sin}z_0 K_1(kd), \tag{4.15}$$

where $K_1(kd)$ is a modified Bessel function of the second kind.

The filled circles in Figure 4.11, are again the amplitudes $U_{3.7}(d)$ plotted versus

---

[1] Using the trigonometric identity: $\sin(s+t) = \sin s\cos t + \cos s\sin t$.

distance to the surface of the wire. The blue curve is a fitted function with the form

$$AK_1(2\pi(d+\delta)/\lambda). \tag{4.16}$$

Here, the fitting parameters are the constant A, the periodicity λ and δ. An offset δ has been inserted in the fitting, giving the freedom for the modelled current to flow at any vertical position in the wire. The best fit to our data gives an amplitude $A = 45 \pm 2.8$ mT, meaning that the amplitude a of the modelled current is 45 ± 3 μm. The characteristic length of the fitting is $\lambda = 217 \pm 10$ μm, close to 230 ± 10 μm, the observed spacing between the potential wells. The offset δ given by the fit is 251 $\pm$ 12 μm, equal to the radius of the wire: 250 μm. The χ^2 parameter here is 4.8 with 4 degrees of freedom.

Our data are evidence of small transverse currents inside the wire in addition to the ideal current. In our search for possible causes for the charges to flow in this manner, we inspected the microscopic structure of the wire by polishing and edging a longitudinal section of the wire. This revealed to us that the grains of the copper core in our wire have a typical length of 10 μm and the defects of the aluminium layer are typically spaced by 5 μm. These imperfections have characteristic lengths of at least one order of magnitude shorter than the spacing between the lumps of atoms in the magnetic trap and the periodicity λ of the Bessel function that fits our data and hence, do not provide an explanation for the current of our proposed model. We remain unable to state the exact origin of the current meanders in our guide wire. We think however, that the cause is a long range defect like a big grain in the copper core underneath the place were the magnetic trap is formed, for example.

4.4 Conclusion and outlook

Our result demonstrates that the field causing corrugations on the long axis of our microtrap decays with the distance from the center of the wire as a Bessel function of the second kind. This potential is equivalent to the potential created by a sinusoidal current flowing through the axis of the guide wire. We rule out surface defects as a possible cause for this effect because the typical spacing between the defects on the aluminium layer is too short compared with the spacing between the observed potential wells. Also, our model tells us that the current oscillates with an amplitude of 45 μm around the wires's axis, inside of its copper core.

Although we cannot provide sufficient evidence supporting the internal defects of the wire as cause of the current meanders, we were the first group to discuss in the literature the wire's morphology as a possible origin of the anomalous potential trap-

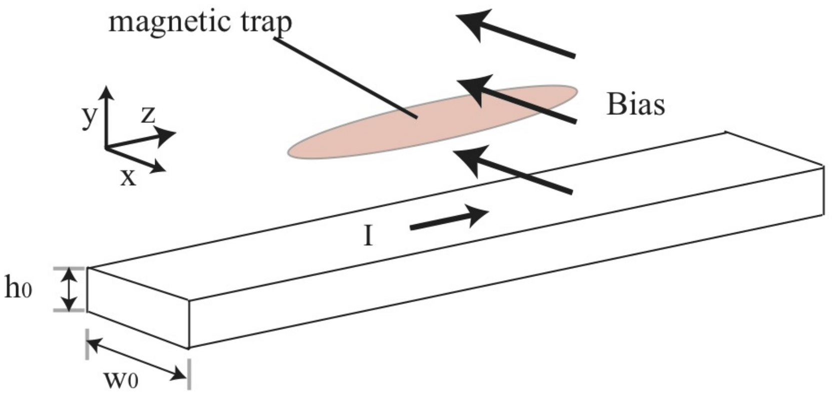

Figure 4.12: Geometry of the wire format used in recently-designed atom chips.

ping atoms [58]. A theoretical approach to this was discussed later on, assuming the fabrication defects of the wire as white noise [107]. The problem was also discussed by the BEC group of Orsay, France with extensive experimental and theoretical research [104, 81]. They tested and compared the DC field near wires fabricated by i) electroplating and ii) electron beam lithography and evaporation. Both were gold, planar wires as shown in Figure 4.12, a geometry adopted for wires in new atom chips. In the two cases, the authors recovered to a good approximation the spectral density of the potential probed with cold atoms by using a model similar to the one proposed in [107]. The computed potentials were based on measurements of the correlation lengths between the defects in the top and side surfaces of the wires, variations around their average height h_0 and width w_0 (see Figure 4.12). Their results demonstrate that the edges of wires patterned by electron-beam lithography are more suitable for building atom chips as they are smoother than the edges of electroplated wires.

Chapter 5

Towards an atom-chip interferometer

This thesis is the first part of a larger research project to perform matter-wave interferometry on an atom chip. The idea is to prepare cold atoms in a Ioffe-Pritchard microtrap that can be dynamically split into a double well. After being split, each part of the condensate would take the role of an interferometer arm [108]. The design and construction of this atom-chip were carried out in collaboration with the Nanoscale Systems Integration group in the School of Electronics and Computer Science, University of Southampton [109]. The atom chip described in this chapter belongs to the first generation of atom chips with this design. This chapter provides an introduction to one of the schemes which can be used to realise atom interferometry. The chapter also describes the modifications done to the BEC setup – which is described in Chapter 2 – to introduce the new atom chip and our first steps using this atom-chip design.

5.1 The double well scheme

Figure 5.1 illustrates the double well scheme. In which the idea is to split a trapping potential into two wells with accurate control of the height of the potential barrier u_0 and the distance d between the two wells. The double well scheme, in combination with the availability of standard methods for the creation of Bose-Einstein condensates, offers a scenario for interesting applications: matter-wave interferometry, basic research on BEC physics and the possibility to realise quantum information processing. Dynamic splitting and recombining of a potential well already provides coherent spatial manipulation of condensates with an accuracy in the nanometer length scale [110]. The first demonstration of the Josephson junction and self-trapping phenomena with Bose-Einstein condensates was achieved by preparing a BEC in an optical poten-

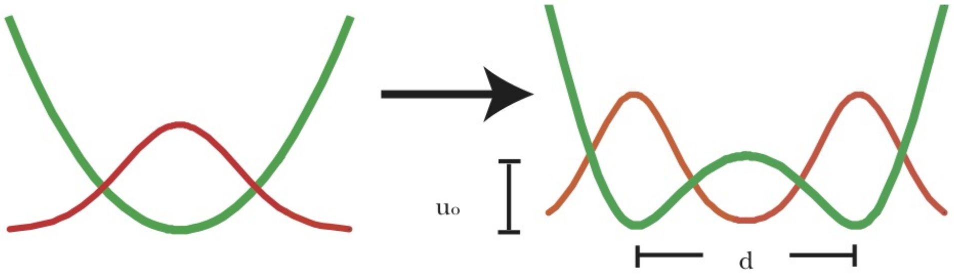

Figure 5.1: Double well scheme for atom optics applications. A matterwave is trapped in a harmonic potential which can be symmetrically split.

tial whose parameters u_0 and d can access both the quantum tunnelling and isolated regimes [111]. Researchers have prepared two condensates and combined them to investigate ultra-cold atom collisions [112]. The double well potential scheme has already been useful to observe matter-wave interference between two condensates. This has been achieved with optical potentials [113, 38], a combination of RF and DC magnetic fields [40] and pure magnetic DC fields [39].

Atom chips are playing a mayor role in the pursuit of quantum control of matter-waves. So far, two experiments with atom chips have produced interference patterns between two Bose-Einstein condensates [40, 39]. Both were direct applications of the double well scheme. In the Heidelberg experiment [40], a Ioffe-Pritchard microtrap was split by dressing the trapped states with adiabatic RF fields. In this experiment, researchers were able to reach both the quantum tunnelling and isolated regimes of the double well scheme. The MIT-Harvard group was the first one that split a BEC on an atom chip with pure DC magnetic fields. The trap design employed in this experiment was based on the field created by two current carrying wires and a bias field – an implementation of the double well scheme that was proposed by E. A. Hinds *et al.* [108].

5.2 A double guide for matter waves

The design of magnetic fields for atom interferometry proposed in [108] consists of two atom guides created with the field of two straight current-carrying wires and a bias field. Figure 5.2 shows a schematic of the system. Two wires are separated by a distance $2D$ on the x-axis. They are parallel to z, and the current I is flowing out of the page. Figure 5.2 also shows a bias field B_x parallel to x. This system is suitable for atom guiding if a bias field of a few hundreds of nT is added in the z-direction, so that the guiding potential has an offset from zero to prevent Majorana loss. It is natural to define D as the unit of length, $B_0 \equiv \frac{\mu_0 I}{2\pi D}$ as the unit of field and $\beta \equiv B_x/B_0$

as a dimensionless bias field.

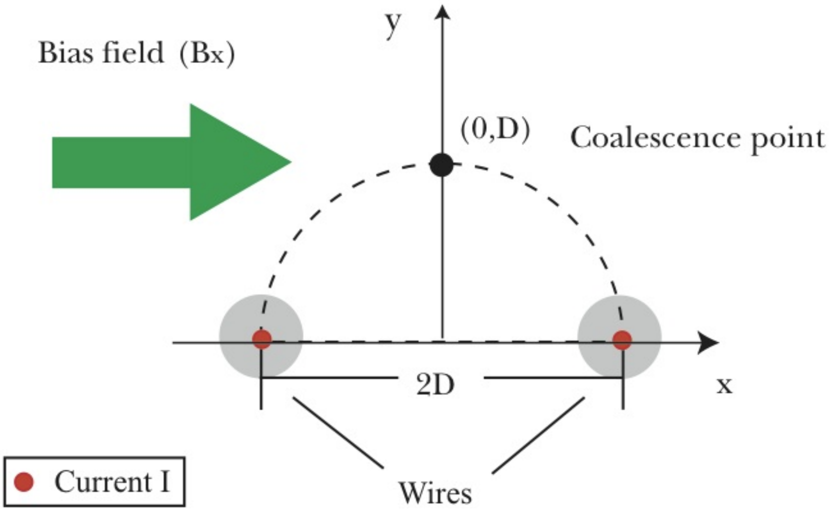

Figure 5.2: Double atom guide proposed in [108] for atom interferometry. The field of two wires carrying a static current I and a bias field can create one or two zero-field lines suitable for guiding cold atoms or Bose-Einstein Condensates .

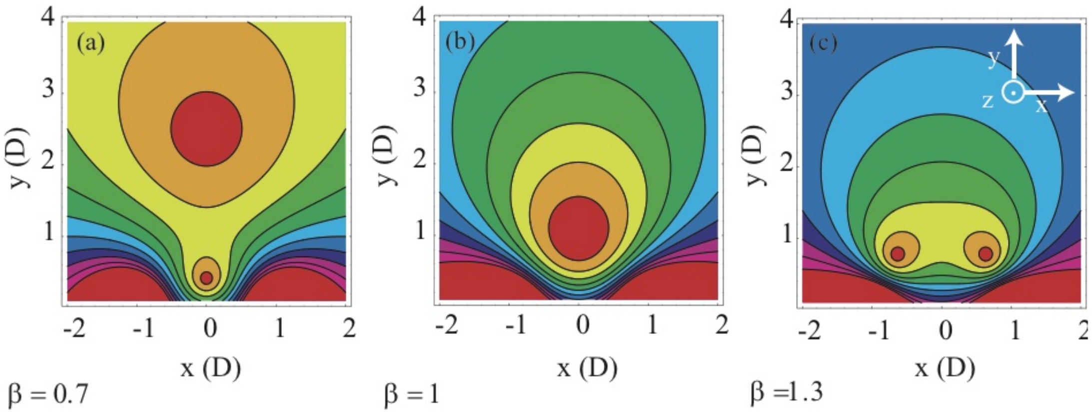

Figure 5.3: Contours of magnetic field magnitude of the field created by two wires and the bias field for the three regimes of β.

When $\beta < 1$ the magnetic field has two minima, both of quadrupole symmetry in the xy plane. Their centers are aligned along y as shown in Figure 5.3 (a). These approach each other as β is increased until they coalesce at $\beta = 1$, as shown in Figure 5.3 (b). Here the magnetic field has hexapole symmetry centered on $(x, y) = (0, D)$. With a further increment to $\beta > 1$, the magnetic hexapole of the coalescence point splits back into two quadrupoles that follow the unit circle $x^2+y^2 = 1$ (in units of D) as β is increased. Reference [108] provides simple analytical formulae for the guide center position on the xy-plane and the magnetic guide depths and gradients as a function of the normalized bias field β. Then the formulae given in Table 5.1, apply to the trap when $B_z = 0$.

The quadrupole traps ($|B| \propto r$) become harmonic with frequency given by Equa-

	Units	$\beta < 1$	$\beta = 1$	$\beta > 1$
(x_0,y_0)	$\frac{1}{\beta}(0,1\pm\sqrt{1-\beta^2})$	(0,1)	D	$\frac{1}{\beta}(\pm\sqrt{\beta^2-1},1)$
u_0	$\mu_B B_0$	$(\beta$,1-$\beta)$	1	β-1
$\partial B/\partial\rho$	B_0/D	$\sqrt{1-\beta^2}(1\mp\sqrt{1-\beta^2})$	0	$\beta\sqrt{\beta^2-1}$

Table 5.1: Position of the center (x_0,y_0), magnetic potential depth u_0 and gradient of the magnetic guide(s) $\partial B/\partial\rho$ created by two wires and the bias field β. Table has been taken from reference [108].

tion (2.22) when adding the axial bias field B_z. Using the formula in Table 5.1 for the transverse field gradient $\partial B/\partial\rho$ with $\beta > 1$, the guide frequency becomes

$$\omega = \sqrt{\frac{\mu_B}{mB_z}\frac{\partial B}{\partial\rho}} = \sqrt{\frac{\mu_B}{mB_z}\beta\sqrt{\beta^2-1}\frac{B_0}{D}}. \tag{5.1}$$

Thus, if β is increased from 1 to 1+ϵ, the trap starts to split along x into two traps, each of frequency

$$\omega = \sqrt{\frac{\mu_B 2\epsilon}{mB_z}\frac{B_0}{D}}. \tag{5.2}$$

Roughly speaking, the guide will split when the ground state energies $\frac{1}{2}\hbar\omega$ become smaller then the barrier height $u_0 = \mu_B B_0\epsilon$. From Equation (5.2) this gives

$$\Delta B_{\text{min}} = \epsilon_{\text{min}} B_0 = \frac{\hbar^2 B_0}{2\mu_B m B_z D^2} \tag{5.3}$$

as the minimum bias field change that would split the ground state of the single well into two. In order to avoid a small ΔB_{min}, we should make B_z small but at the same time it has to satisfy the adiabatic condition

$$\omega_L = \frac{\mu_B B_z}{\hbar} \geq \omega, \tag{5.4}$$

where ω_L is the Larmor frequency at the bottom of the trap. Equations (5.4) and (5.2) together yield

$$B_z^3 \geq \frac{2\hbar^2 B_0^2\epsilon}{\mu_B m D^2}. \tag{5.5}$$

By using ϵ_{min} from Equation (5.3), we obtain

$$B_z \geq \frac{\hbar}{D}\sqrt{\frac{B_0}{\mu_B m}}. \tag{5.6}$$

As discussed later in sections 5.3 and 5.4, one of our atom chips has $D = 41.5\ \mu$m and the wires can carry currents of the order of 1 A, giving $B_0 = 4.8$ mT. With these numbers, $B_z \geq 152$ nT is required. Thus we obtain a minimum ϵ required to split the ground state of our trap of 1.6×10^{-4}. Expressed as a field, this is $\Delta B_{\text{min}} = 76$ nT. Though challenging, such a level of field control is readily achieved with modest shielding.

5.3 The atom chip with four Z-wires

Figure 5.4 (a) shows a photograph of the new interferometer atom chip based on an extension of the Z-wire idea. The design of this atom chip includes four wires with a Z-shape. Each one of these wires is suitable to create a Ioffe-Pritchard microtrap by driving a current I through it [28]. The Z-shape of these wires, highlighted by the red arrows in Figure 5.4 (a), causes the ends of the traps to be closed. This atom chip has been also patterned with two end wires. These are the thickest wires on the atom-chip as can be seing in Figure 5.4 (a). They were designed to give the option of running the current in a U-shaped pattern, showed by the red arrows plus the green arrow in Figure 5.4 (a). This is used for magneto-optical trapping [28]. Alternatively, the end wires can be used to increase the axial depth of the Ioffe-Pritchard trap(s) created by the Z-wires. All the wires have been wet-etched in gold on the surface of a silicon wafer. The gold layer is 5.5 μm thick and covers the full atom-chip surface (26 × 22 mm) in order to reflect laser light for a mirror MOT.

Figure 5.4 (b) is an optical microscope image of the central part of the Z-wires. The outer wires are 85 μm wide and the width of the inner wires is 33 μm. The center-to-center distances are 83 μm between the inner wires and 300 μm between the outer wires. The techniques employed to construct this atom chip are described by Koukharenko *et al.* [109]. The chip is built on a 0.5 mm silicon wafer covered by a 600 nm thick insulating layer of SiO_2. A thin, adhesive layer of Cr is sputtered on to the SiO_2, followed by a 5.5 μm layer of gold. A schematic of all these layers is shown in Figure 5.5 (a). The wires were patterned on the gold surface with a photolithography technique using a mask made of standard photoresist and exposure to UV light. The schematic in Figure 5.5 (b) illustrates the lithography process after UV exposure. Figure 5.5 (c) shows the cross section of all layers after the wires were wet etched. This completes the manufacturing process of the wires.

This atom chip was built before the implications of atom-surface interactions were well understood. As a result of the research presented in Chapter 3, and in particular Equation (3.40), we now know that the spin flip lifetime is longer by a factor of d/h_0 near thin surfaces. Here d is the atom-surface distance and h_0 is the height of the

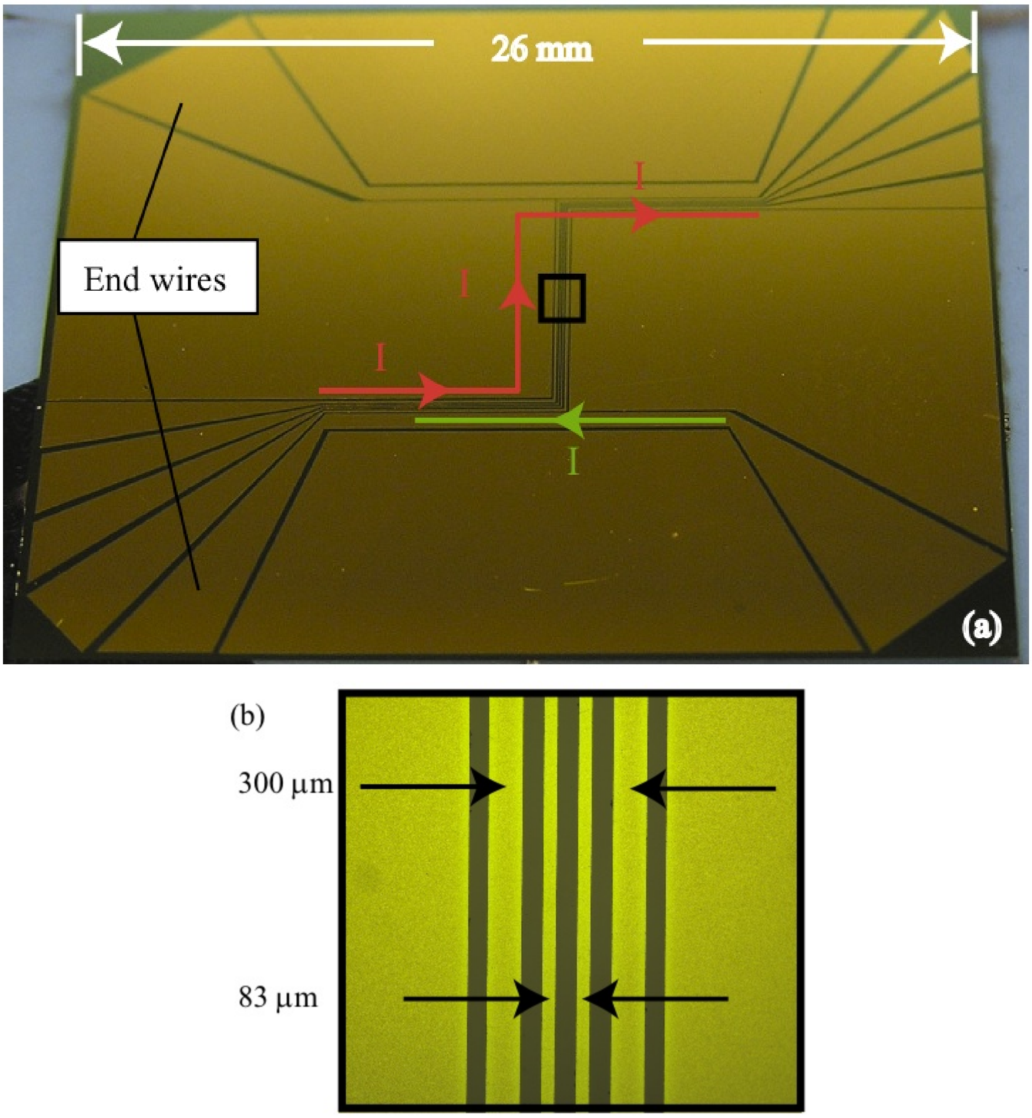

Figure 5.4: Images of the new interferometer atom chip. (a) full-scale photograph of the atom chip. The red arrows are parallel to the Z-shape of the wires and denote the direction of a current flowing through them. The green arrow illustrates the option of running a current with a U-geometry by driving current a current I through one of the end wires. (b) is an optical microscope image of the central region. The inner and outer wires are 33 μm and 85 μm wide respectively. The arrows in (b) indicate the center-to-center distance between each pair of wires.

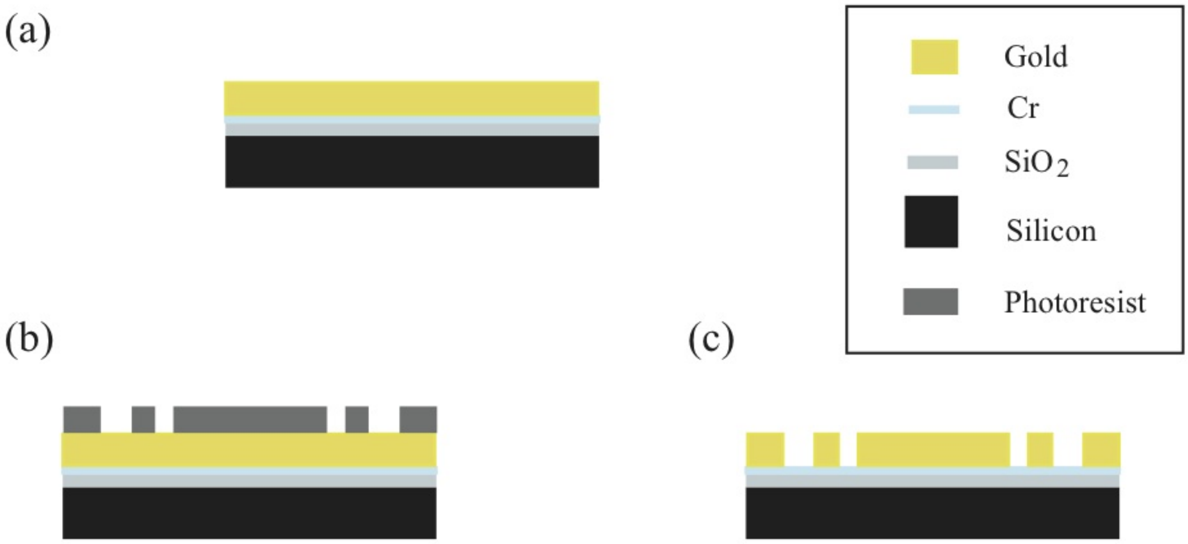

Figure 5.5: Schematic (not to scale) of the techniques employed to build the 4Z-wire atom chip. (a) the surface of this atom chip has been built on silicon wafers. It has been constructed by layers: SiO_2, Cr and Au. (b) the photoresist mask is developed. (c) all layers after wet etching the gold wires.

wire, see Figure 4.12. For this reason, the next generation of atom chips, will have a significantly thinner gold layer.

The DC field of wires manufactured with a similar technique has already been probed with cold atoms [104]. It was shown that the edges of wet-etched wires produce transverse currents that contribute significantly to the corrugations of the trapping potentials. It was also shown that ion beam milling is a better technique to manufacture wires for microtraps [81]. The later technique is being used to build the next generation of atom chips. Nevertheless, the atom chip described here is useful to learn about the experiments that are possible with the 4Z-wire design.

5.4 The new flange and control interface

We carried out a number of modifications to the BEC apparatus to prepare it for the 4Z-wire atom chip. The atom chip with a single guide wire described in Chapter 2 was oriented with gravity acting towards the surface. This orientation limits ballistic measurements to just a few milliseconds of expansion time. Longer expansion times provide a more convenient diagnostic. For this reason, the entire vacuum chamber has been inverted in preparation for the 4Z-wire atom chip so gravity points away from its surface. Additionally, the computer-control interface has been updated.

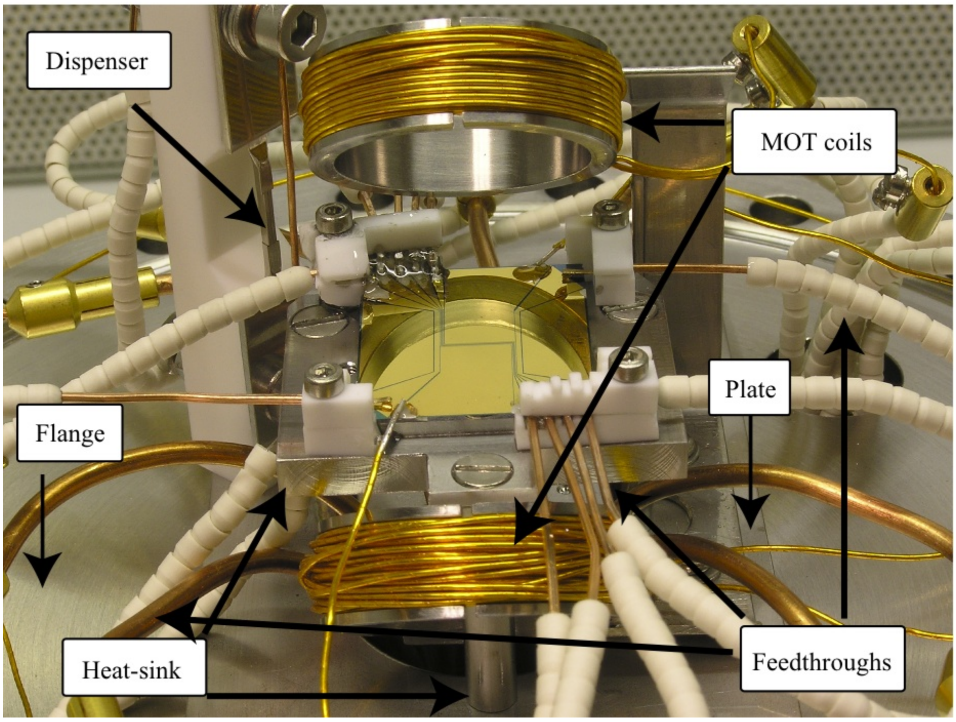

Figure 5.6: The 4Z-wire atom chip assembled on its mount, a stainless-steel heat sink. The wires were connected to computer controlled supplies through three UHV feedthroughs located in the flange. The dispenser is mounted 3 cm from the center of the atom chip. The MOT coils have been designed to create a quadrupole magnetic field 4 mm above the center of the atom chip.

5.4.1 Mounting the 4Z-wire atom chip

Figure 5.6 is a photograph of the 4Z-wire atom chip ready to be introduced to the vacuum chamber. This shows the atom chip, its mount, the MOT coils, the rubidium dispenser and the stainless-steel flange on which everything is assembled. The atom chip is mounted on a stainless steel heat sink built in separate pieces: a 1 mm-thick slab exactly matching the area of the atom chip (26 ×22 mm), a rectangular block (5 × 38 × 32 mm) and three 23 mm long rods with a radius of 5 mm.

Figures 5.7 (a) and (b) are detailed diagrams of the atom chip and its mount. The atom chip is directly mounted onto the slab matching its area. Which in turn sits on the rectangular block of stainless steel. These are fixed in place by four corner-shaped pieces of Macor grooved with 0.81 mm square channels, shown pink in Figure 5.7 (a). The grooves are machined on the Macor pieces to locate thin strips of BeCu at their bottom. The BeCu strips, are attached to the Macor with a drop of silver paint and then mechanically held by 20-Gauge square copper wire pushed into the grooves, see figures 5.7 (a) and (b). Atom chip, grooved Macor pieces, BeCu strips and square-copper wire are held together by another set of corner-shaped Macor pieces bolted to the block of stainless steel through the grooved Macor pieces as shown in Figure 5.7

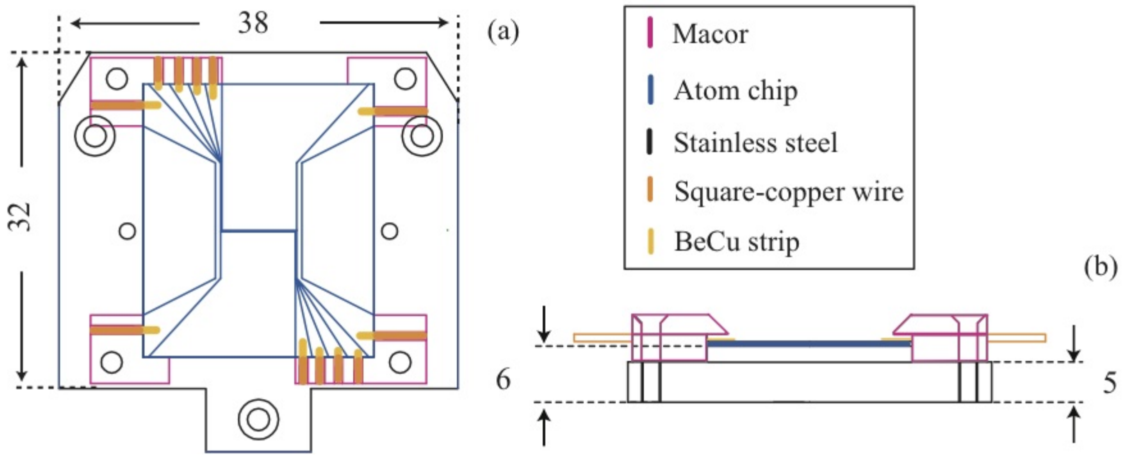

Figure 5.7: The new atom chip has been mounted directly onto a stainless-steel heat sink. It is fixed on place by four corner-shaped pieces of Macor grooved with 0.81 mm square channels. In each channel, a thin strip of BeCu and 20 gauge square copper wire are fixed to allow electric contact from each wire to the control hardware of the experiment (a). The connections were mechanically supported by another set of four corner-shaped pieces of Macor that were bolted to the heat-sink block through the grooved pieces of Macor (b).

(b) which is a lateral view of the atom chip and its mount. The function of the BeCu strips is to make electrical contact between the copper wires and the atom chip. This contact is achieved by gluing them to the extremes of the wires first with silver paint and then with Bylapox for mechanical strength. In this manner, the wires of the atom chip are connected to the control hardware through the strips of BeCu, the square copper wire and the feedthroughs mounted on the flange as shown in Figure 5.6.

The MOT coils, also shown in Figure 5.6, are orientated so they produce the field for a mirror MOT as explained in Section 2.3.1. Their coil formers have a 25 mm diameter and their center-to-center distance is 45 mm. The coils are wound with 47 turns of Kapton insulated copper wire with 0.62 mm diameter. The center of the quadrupole field is placed about 4 mm above the center of the atom-chip surface, with the axis of the coils making a 45° angle its normal. The dispenser is mounted 3 cm from the center of the atom chip to allow MOT loading in a pulsed mode. The atom-chip mount, dispenser and MOT coils were assembled on a rectangular stainless-steel plate which in turn is attached to the conflat (CF) stainless steel flange, 203 mm (8 in) in diameter.

All the currents inside the vacuum chamber – through atom-chip wires, MOT coils and dispenser – are supplied through three feedthroughs in the CF flange, providing 24 connections to the control hardware. In Figure 5.6 one can see the square copper wires and other wire connections grouped to access each of the three feedthroughs. Figure 5.8 is a diagram to scale the whole vacuum system together. It shows the top view of the vacuum system, in which the location of each feedthrough on the CF flange can be seen. The central feedthrough has a 70 mm (2 3/4 in)-diameter and eight-pin connectors. This feedthrough is supplied by MDC Vacuum Products, LLC (part No.647051). The lateral feedthroughs have also eight pin connectors each, they were supplied by Ceramaseal (part No.9340-05-CF) and their diameter is 34 mm (1 1/3 in).

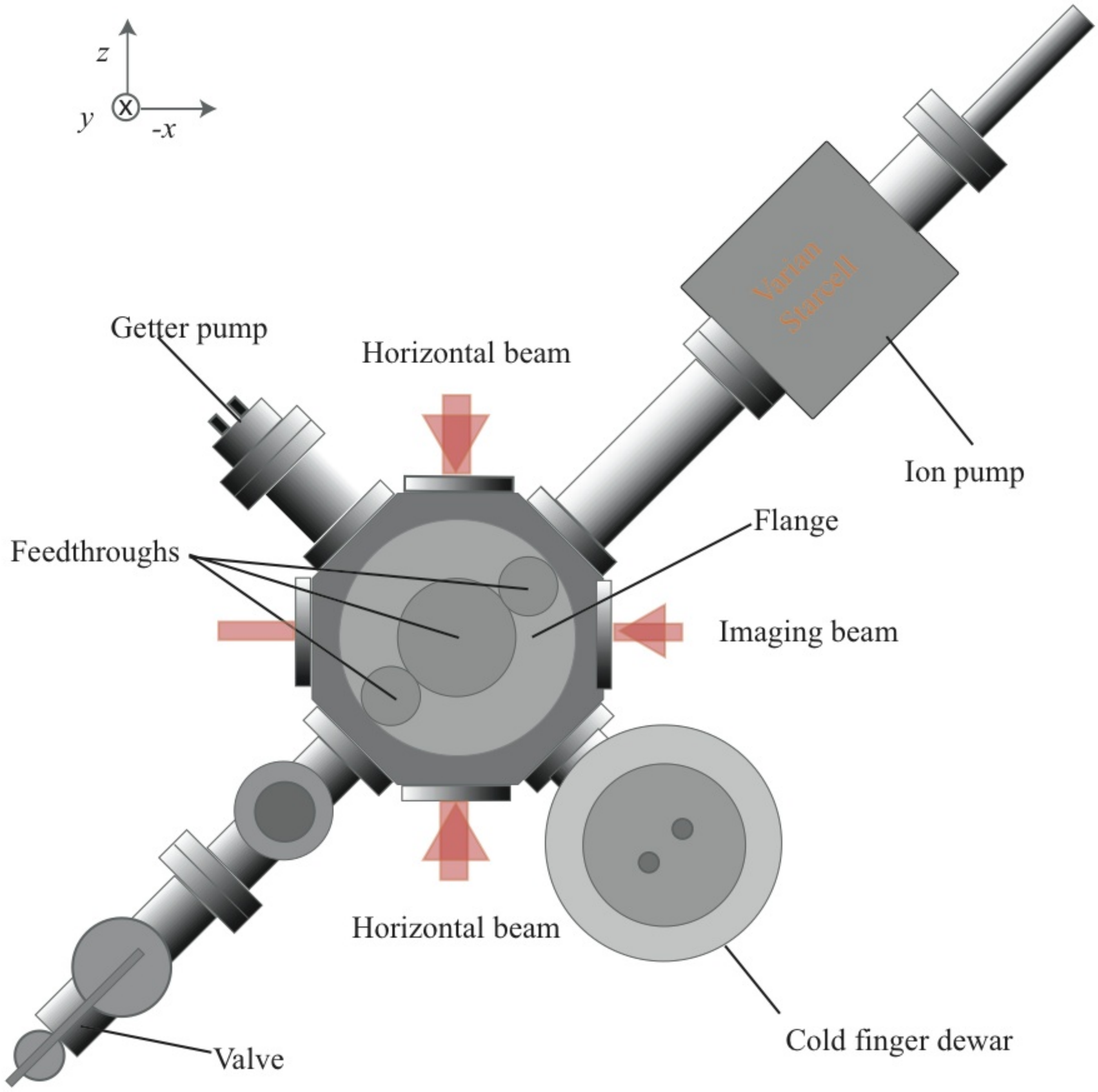

Figure 5.8: Diagram to scale of (the top view) our vacuum system. A base pressure in the mid 10^{-11} torr range is achieved with a non-evaporable getter (NEG) pump and an ion pump. Vacuum recovery from rubidium dispensing during experiments is supported with a liquid-nitrogen cold finger.

5.4.2 Computer control

In addition to the modifications that prepared the experiment to receive the new atom chip, we also updated the computer control interface of the experiment. Both the software and hardware of computer control were replaced. The base of the new hardware are two National Instruments (NI) cards that generate TTL and analog signals. The control software is called Hermes, and was written in JAVA by C. D. J. Sinclair [114]. This combination of software and hardware provides us with more TTL lines, the possibility to drive two digital signals through a single TTL channel, and a source of analog signal with good quality.

Hermes has a user friendly interface in which an experiment can be tailored with a chosen number of processes. A screen shot of the Hermes' interface is displayed in Figure 5.9 to illustrate its functioning. Each row represents one process which can have as many TTL and analog channels as provided by the NI cards. A process can be as short as 10 μs. Hermes generates TTL signals in two manners. It can send either one or two-bit TTL signals. On the screen, the one-bit signals have the natural on and off options represented by the green or white filled squares in Figure 5.9. The two-bit signals are generated by what we call a 'level setter', also shown in Figure 5.9. With these, we give to a single experimental parameter up to four states that can be changed as fast as the TTL time resolution. The level setters are currently used in our experiment due to historical reasons. The old interface was not provided with analog channels, wave generators were used instead. The level setters were a solution to control with a certain freedom a few parameters of the experiment requiring sharp switching such as the current through the MOT coils or the Rubidium dispenser. One of the goals of using the new interface, is to replace the level setters with analog channels. That would remove the restriction for these parameters to have just four options to input the experiment and free useful TTL channels. Each process in the Hermes's interface can also include the analog control of currents as shown in Figure 5.9. For this, one is required to input an initial and a final voltage in each process. During experiments, the analog output signal is linearly ramped from the initial to the final voltage over the duration of each process.

The digital signals are sent from the computer to the experiment by a PCI 6534 card with 32 TTL ports. This card has a 68-pin male output which is connected to a signal distribution panel by a NI shielded cable (Part No. 183432-05). The distribution panel directs the signals to the current driving electronics. Each TTL signal is first amplified by a Multiplexer circuit, and then forwarded to the circuit which finally delivers the current into the experiment. The later circuit has a field effect transistor (FET) as switching component. In its 'on' mode, reached with a response time of about 100 μs, the 'FET' circuit outputs a voltage proportional to the input signal. The load of this circuit can be either resistive, such as wires and rubidium dispenser, or inductive like the MOT or external coils in the experiment.

To generate the analog-controlled currents we use a NI PCI 6713 card with eight analog channels. Each channel outputs a 0-10 V peak-to-peak signal. If a larger signal

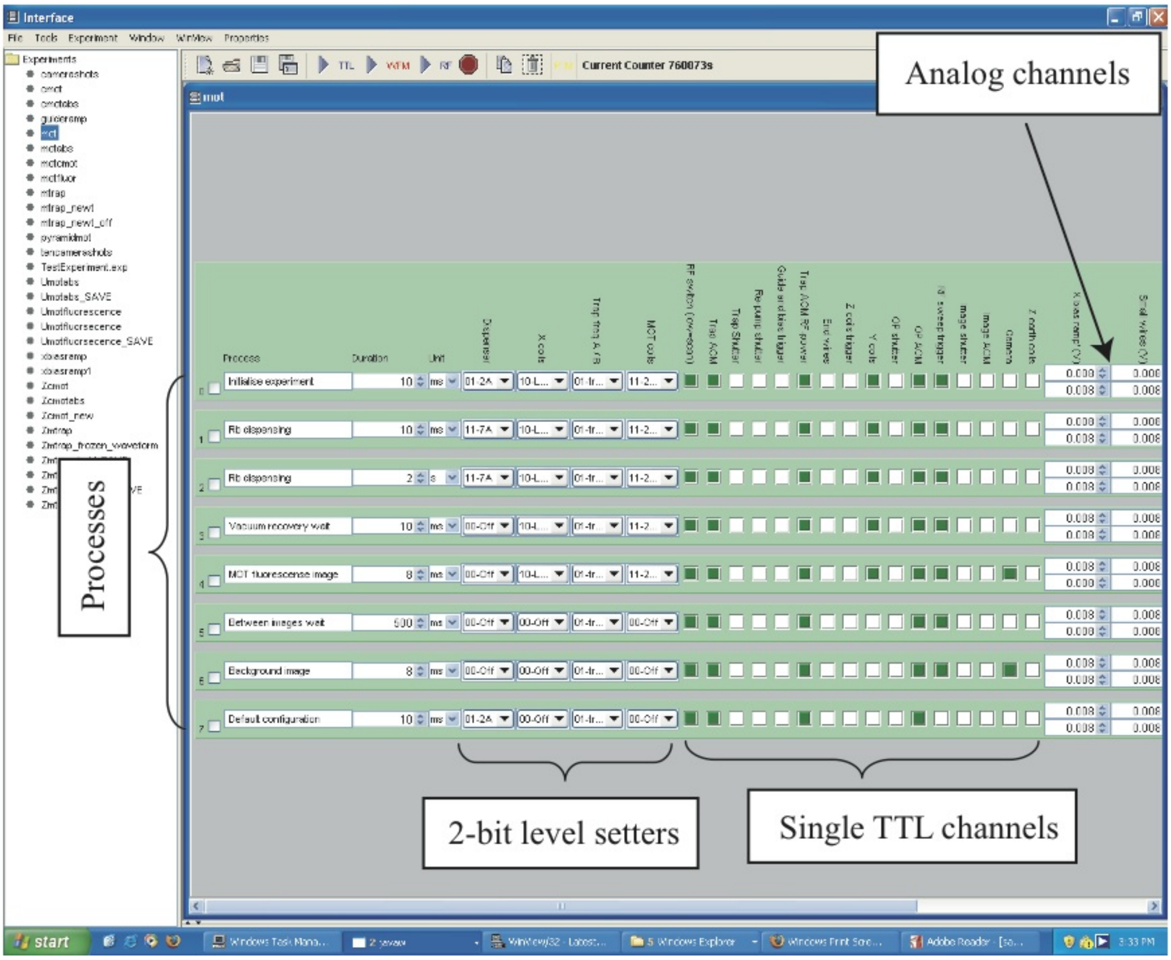

	Process	Duration	Unit	Dispenser	X coils	Trap freq A / B	MOT coils	RF switch (ON=open)	Trap AOM	Trap Shutter	Re-pump shutter	Guide and bias trigger	Trap AOM RF power	End wires	Z coils trigger	Y coils	OP shutter	OP AOM	RF sweep trigger	Image shutter	Image AOM	Camera	Z earth coils	X bias ramp (V)	Small wires (V)
0 ☐	Initialise experiment	10	ms	01-2A	10-L...	01-fr...	11-2...	■	■	☐	☐	☐	■	☐	☐	■	☐	■	■	☐	☐	☐	☐	0.008 0.008	0.008 0.008
1 ☐	Rb dispensing	10	ms	11-7A	10-L...	01-fr...	11-2...	■	■	☐	☐	☐	■	☐	☐	■	☐	■	■	☐	☐	☐	☐	0.008 0.008	0.008 0.008
2 ☐	Rb dispensing	2	s	11-7A	10-L...	01-fr...	11-2...	■	■	☐	☐	☐	■	☐	☐	■	☐	■	■	☐	☐	☐	☐	0.008 0.008	0.008 0.008
3 ☐	Vacuum recovery wait	10	ms	00-Off	10-L...	01-fr...	11-2...	■	■	☐	☐	☐	■	☐	☐	■	☐	■	■	☐	☐	☐	☐	0.008 0.008	0.008 0.008
4 ☐	MOT fluorescense image	8	ms	00-Off	10-L...	01-fr...	11-2...	■	■	☐	☐	☐	■	☐	☐	■	☐	■	■	☐	☐	■	☐	0.008 0.000	0.008 0.000
5 ☐	Between images wait	500	ms	00-Off	00-Off	01-fr...	00-Off	■	■	☐	☐	☐	■	☐	☐	☐	☐	■	■	☐	☐	☐	☐	0.008 0.008	0.008 0.008
6 ☐	Background image	8	ms	00-Off	00-Off	01-fr...	00-Off	■	■	☐	☐	☐	■	☐	☐	☐	☐	■	■	☐	☐	■	☐	0.008 0.008	0.008 0.008
7 ☐	Default configuration	10	ms	01-2A	00-Off	01-fr...	00-Off	■	■	☐	☐	☐	■	☐	☐	☐	☐	■	☐	☐	☐	☐	☐	0.008 0.008	0.008 0.008

Figure 5.9: Screen shot of Hermes, the new software for computer control of our BEC setup. Each TTL channel can be arranged to receive a 1-bit or 2-bit signal. The analog channels ramp linearly the output voltage from the initial and final values given by the user.

is required, one needs to feed power into the card through one of its input channels. The analog channels are updated by a 1 kHz TTL signal from the digital (PCI 6534) card, fixing the time resolution of the analog signals to 1 ms. A convenient change, to allow sharper changes of the analog driven currents, would be to update the analog card with a faster TTL signal. The analog signals are also sent from the NI card to a distribution panel through a NI shielded cable (Part No. 183432-05). This panel sends each signal directly to its corresponding FET circuit, which in turn delivers a current to its load inside the experiment.

5.5 The 4Z-wire atom chip in UHV

Our vacuum chamber is a 203 mm Multi-CF Spherical Octagon supplied by Kimball Physics, Inc. It is cylindrical, with ten CF ports. The top and bottom ports have 203 mm diameter, while eight ports of 70 mm diameter are located in the sides of the cylinder. Once the CF flange is assembled with the new chip and connections,

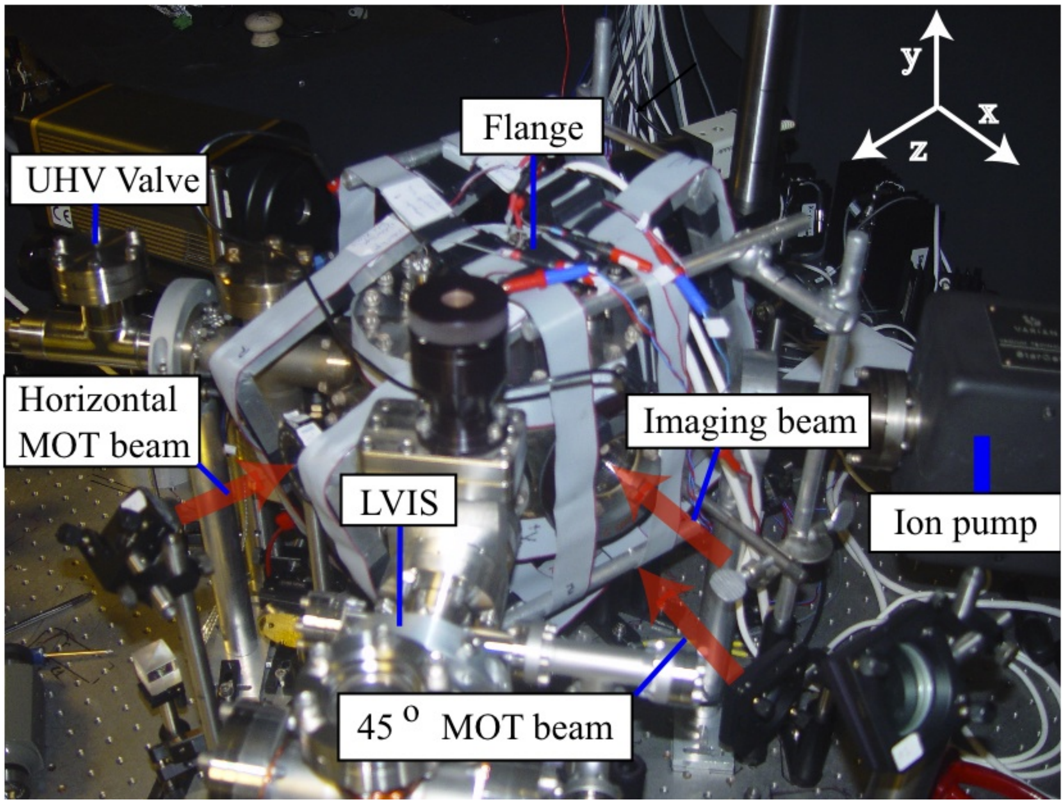

Figure 5.10: This is a picture of our BEC apparatus in its current stage. The Low-Velocity Intense Source (LVIS) of cold atoms is one of the changes made after this thesis; it is connected to the vacuum chamber through the opening that used to host the liquid nitrogen cold finger.

it is bolted to the top of the vacuum chamber. The chip is mounted upside down to increase the time available for the atoms to fall after being released from a MOT or a magnetic trap. Figure 5.10 shows a picture of the vacuum chamber assembled.

BEC on atom chips is normally achieved with RF-evaporations that last for about 10 s. The magnetic trap lifetimes should be long enough to allow a successful evaporation and leave time to realise experiments. In order to have magnetic trap lifetimes in the order of a minute, ultra high vacuum (UHV) is required inside the vacuum chamber. A base pressure in the mid 10^{-11} torr is maintained inside our vacuum chamber with the assistance of an ion pump (Varian VacIon Plus 20 model 919-0235) and a Non-Evaporable Getter (NEG) pump (SAES Sorb-AC GP50), both shown in Figure 5.8. During experiments we use a cold finger sticking a few centimeters into the vacuum chamber for a quick vacuum recovery after rubidium dispensing. The pressure is monitored by a Varian UHV-24 ion gauge with a working pressure range from 10^{-3} to 2×10^{-11} torr.

We achieved UHV by baking the whole vacuum system for 5 days at 120 °C inside a home built oven. A long bakeout time is required because the baking temperature is limited to 125° C by the Bylapox glue that is used to connect the the wires of the atom-chip. During the bakeout, a turbo pump and a Residual Gas Analyzer (RGA) are connected to the vacuum chamber through the UHV valve shown on Figure 5.8. This enables us to pump down from atmospheric pressure and monitor the internal gas composition. The oven is heated slowly from room temperature to the baking temperature over approximately ten hours to avoid thermal stresses.

We activated the NEG pump by running 2 A through it for one hour and then 4 A for 45 minutes during the bakeout. At this point we ended the activation prematurely because we realise that the atom chip is being heated up to more than 120 °C when running current through the NEG. Next, we degased the MOT coils by running them at 2.5 A for approximately one hour. The Rb dispenser is also degased by gradually increasing its current from 0 to 5 A and keeping it constant for one hour. This is followed by a second NEG activation and MOT coils degas. When the pressure reached the 10^{-4} torr scale, the ion gauge is switched on and degased as well. The ion pump is turned on and the turbo pump isolated with the UHV valve when the pressure falls to about 10^{-8} torr. Finally, the turbo pump and the RGA are turned off and disconnected from the system. This bakeout allows us to reach a base pressure in the mid 10^{-11} torr scale.

Wires	ρ_r (Ω)	I (A)	J (A m^{-2})
Inner	6.8	1.7	9.4×10^9
Outer	2.5	2.7	5.5×10^9
End	0.5	8	3×10^9

Table 5.2: Maximum current and current densities to safely run through the diverse wires on the 4Z-wire atom chip.

Once UHV is achieved in the vacuum chamber, we measure the resistance of the wires on the chip as recorded in Table 5.2. Next, we tested the current carrying capability of each wire by applying a 1 s current pulse and monitoring the change of resistance.

Theoretically, the temperature rise of thin wires patterned on a silicon substrate behaves as [115]

$$\Delta T = \frac{h\rho j^2}{k - h_0 j^2 \alpha\rho}(1 - e^{-t/\tau_{\text{fast}}}), \tag{5.7}$$

where k is the thermal conductance defined as the quantity of heat per unit time transmitted through the contact surface between the wire and silicon substrate due to their difference in temperature; h_0 is the height of the wire (see Figure 4.12); ρ is the resistivity of the gold wires with coefficient of linear dependency α, $\Delta\rho = \alpha\rho\Delta T$ and j is the current density flowing through the wire. In Equation (5.7), the saturation time is

$$\tau_{\mathrm{fast}} = \frac{C_w h}{k - hj^2\alpha\rho}, \tag{5.8}$$

were C_w is the heat capacity per unit volume of the wire.

The height of our wires is $h_0 = 5.5$ μm, the thermal conductance $k = 2.6 \times 10^6$ W $\mathrm{K}^{-1}\mathrm{m}^{-2}$ for gold surface in contact with a 500 nm thick layer of SiO_2, the resistivity of gold $\rho = 2.44 \times 10^{-8}$ Ωm and $\alpha = 3.5 \times 10^{-3}$ K^{-1} is its linear coefficient. When the current density exceeds

$$J_{\mathrm{max}} = \sqrt{\frac{k}{h_0\alpha\rho}}, \tag{5.9}$$

the factor at the left in Equation (5.7) reaches a singularity, leading to an almost immediate destruction of the wire. Note that both, the time dependence of the temperature change and the maximum current density, are independent of the width of the wire. Thus, we can estimate a single maximum current density for all the wires on our chip: $J_{\mathrm{max}} = 7.44 \times 10^{10}\mathrm{Am}^{-2}$.

Our temperature response tests start with a 0.11 A current, equivalent to 6.1 $\times$ 10^6 A m^{-2} in the narrowest (inner) wires. The current through the wires is then increased and stopped when the temperature rise shows big and random peaks due to abrupt changes in the resistance of the glued connections. The current for which this happens in each wire is defined as the maximum current to run the experiment in a safe manner. These are the currents shown in Table 5.2, together with their corresponding current density which are about an order of magnitude lower than the maximum current density predicted by Equation (5.9). This suggests that indeed, the maximum current densities that can safely be run through the wires are in practice limited by the 120 °C maximum operating temperature of the Bylapox glue supporting the silver-paint electrical connections.

5.6 The first experiments

We arranged the BEC apparatus so the magnetic trap is supplied with cold atom by a pulsed mirror MOT, as previously done on the atom chip with a single-guide wire. This section reports our first steps towards trapping atoms with this atom chip.

5.6.1 The mirror MOT

An absorption image of a mirror MOT created on this atom chip is shown in Figure 5.11. This MOT is created by initially running 2 A through the new MOT coils, providing us with a field gradient of about 1.9 mT cm^{-1} in the axial direction of the anti-Helmholtz arrangement. The center of the MOT quadrupole is about 4 mm from the atom chip surface. During most of the MOT stage the main beam has a 160 mW total power evenly distributed among the four MOT beams and the detunning of the trapping light is - 18 MHz from the $F = 2 \longrightarrow F = 3$ resonant frequency. In the last 2 ms seconds, the MOT-quadrupole gradient is decreased to 75 % of its original value and the trapping-light detuning is increased to -40 MHz. This mirror MOT cools 5×10^7 atoms down to 220 μK. The temperature of the atoms is measured with ballistic expansion, as explained in Appendix D.

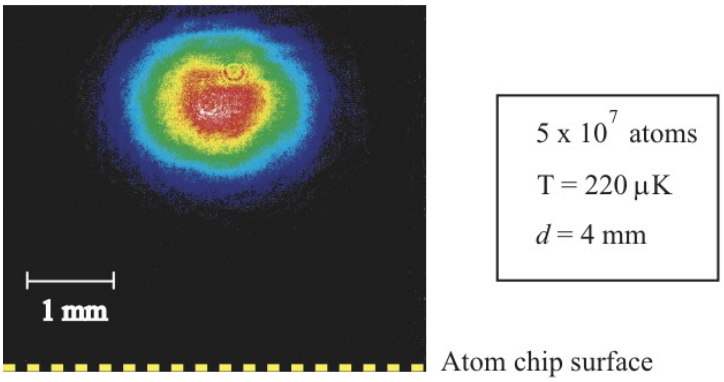

Figure 5.11: Absorption image of the mirror MOT on the 4Z-wire chip.

Both, atom number and temperature in the mirror MOT, are to be optimized. Variation of parameters such as the trapping light power and detuning and distance from the MOT to the atom chip surface should enable us to reach temperatures of the order of tens of microkelvin and increase the atom number by about a factor of two.

5.6.2 The U-MOT

Figure 5.13 (a) is a schematic of the U-current in the atom chip. The thick strips of gold at the top and bottom represent the end wires. A magnetic quadrupole is produced with the field of a U-shape current plus a bias field, shown as B_x in Figure 5.13 (a). This field is parallel to the plane of the chip.

Figure 5.13 (b) shows the contour lines of the field produced with 4 A following a U path (1 A through each Z-wire and 4 through the lower end wire) and a bias field of 0.76 mT. B_x is provided by the same pair of external coils source of bias field for the old atom chip. The resulting magnetic field is shown in Figures 5.13 (c). The field has a zero line at $y = 1$ mm, parallel to the central section of the U and shifted by about 200 μm towards -x, see figures 5.13 (b) and (c).

The correct correspondence between the local field direction and the laser light polarization is crucial for atom collection in a MOT. The magnetic field created with this U-configuration [Figure 5.13 (c)] can be considered a magnetic quadrupole just

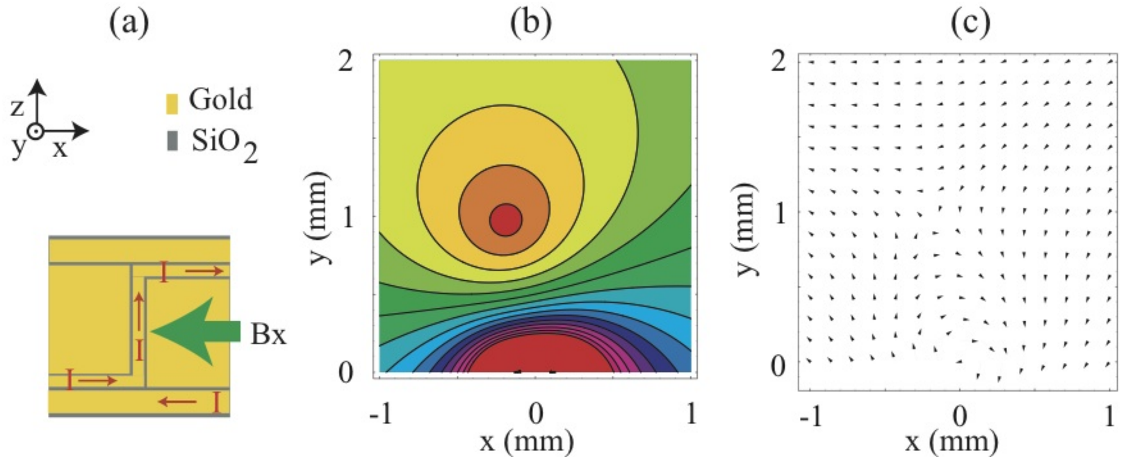

Figure 5.12: Magnetic field produced with the U-configuration in this atom chip. This is realized by (a) running 1 A through each one of the Z-wires and 4A through the lower end wire plus 0.76 mT of bias field B_x. The field produced with the wires cancels with B_x at $x_0 = -0.2, y_0 = 1$ (mm) as shown in (b). The vector field is shown in (c). It is a magnetic quadrupole just near the cancellation point.

within a small region in the vicinity of its center. In order to capture a large number of atoms with a U-MOT, one must either optimize the field design[1], or concentrate a large number of cold atoms in the region where the field is close to a magnetic quadrupole. Our experiment is designed for the the second option; we transfer atoms cooled and trapped by the mirror MOT to the U-MOT. Performing magneto-optical trapping with the U-configuration has the aim to pull atoms towards the surface of the atom chip and give the atom cloud a cigar shape. This is equivalent to the compressed MOT stage used with the single-guide wire atom chip, in which atom clouds were prepared to match in shape that of the Ioffe-Pritchard trap.

To transfer atoms from trap to trap, we superimpose the U-field on the MOT quadrupole by linearly ramping the current through the Z wires and one the lower end wire from 0 to 4 A over 50 ms. Simultaneously the bias field B_x is also linearly ramped up, from 0 to 0.76 mT. This transformation of the trap pulled about 10^7 atoms down to about 1 mm from the surface. Three parameters of the MOT are changed over the last 2 ms of the U-MOT stage. The trapping light detuning is changed from -18 to -40 MHz, its power is decreased from 160 to 20 mW and the MOT coils are switched off. Thus magneto-optical trapping is achieved just with the U-quadrupole. The absorption image shown in Figure 5.13 is taken 3 ms after releasing atoms from the U-MOT. With ballistic expansion measurements, we find that the temperature of atoms is 112 μK at this point (see Apendix C).

---

[1] The number of atoms that a U-MOT can capture without previous cooling and trapping can be optimized by increasing the surface of the central part of the U or by adding bias fields that will make the total field close to a magnetic quadrupole in a longer spatial region [116].

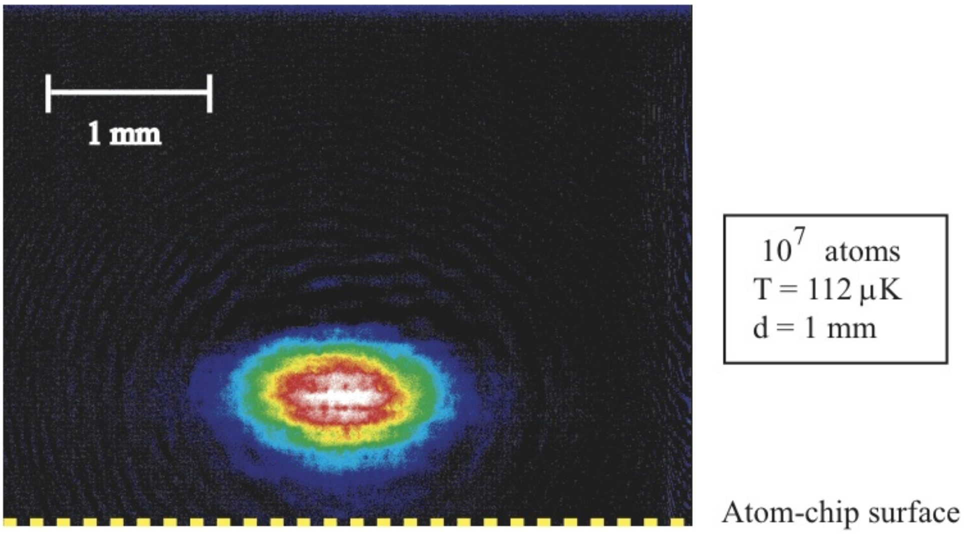

Figure 5.13: Absorption image of the U-MOT.

5.6.3 The Z-Ioffe-Pritchard trap

The U-MOT prepares the atoms for loading into a Ioffe-Pritchard trap, created by running 4 A through the Z wires with the same 0.76 mT of bias field.

Figure 5.14 (a) shows the layout of atom chip running a Z-current, producing a Ioffe-Pritchard microtrap. Once the U-quadrupole is switched on, the Z-configuration is activated by just turning off the current through the end wire. In the case described here, we continue to use the final current and bias field of the U-MOT stage: 4 A and 0.76 mT. These create a magnetic quadrupole (atom guide) at 1 mm from the surface of the wire, as illustrated in Figure 5.14 (b). The magnetic guide is closed to form a Ioffe-Pritchard trap by the field created due to the end sections of the Z. These fields combined form a cigar-shaped potential, whose axis makes an angle to the z-axis as shown in Figure 5.14 (c).

The cross sections through the center of this trapping potential, along each spatial direction are shown in Figure 5.14. In the xy-plane, the trapping potential is equivalent to an atom guide produced by a single guide wire as shown in figures 5.14 (d) and (e). Figure 5.14 (f) shows the z cross section of the trapping potential. The z-component of the field is produced by the ends of the Z. It creates a Ioffe-Pritchard trap (apart from the tilt of the guide axis), providing axial confinement and offsetting the field at its center to prevent Majorana transitions. The insets in figures 5.14 (c) and (d) show a zoom to the center of the trap in the x and y directions, where the trap is well approximated by a harmonic potential. The depth of this trap in the x and y directions is 469 μK, given by the difference between the bias field B_x and the field at the center of the trap. The axial depth is 471 μK, the difference between the trapping potential at the center of the trap and above the end parts of the Z.

We can load 10^6 atoms into the Z-trap. A picture of an atom cloud 3 ms after being released from the magnetic trap is shown in Figure 5.15. There is an atom loss of one order of magnitude while transferring atoms from the U to the Z-quadrupole, occurring for two reasons. Firstly, atoms held by the U-MOT are shifted 200 μm from the center of the Ioffe-Pritchard microtrap. The shift exists because the lateral parts of the U are not equidistant from its central section. This causes sloshing of the atom cloud, which leads to heating and ultimately to atom loss. One possibility for fixing this problem is to bring the center of the U-quadrupole near the center of

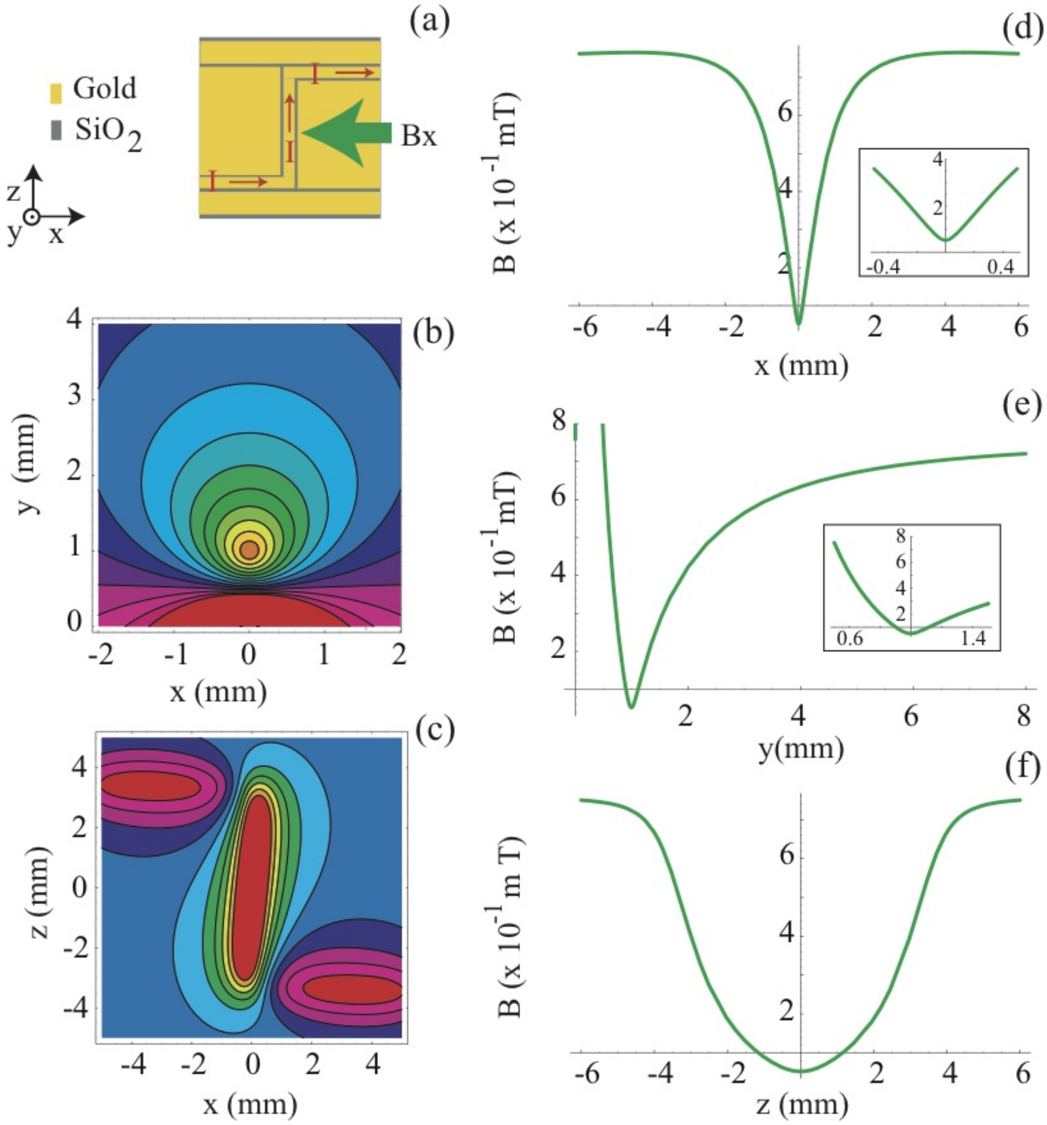

Figure 5.14: The Z-trap in our atom chip. It is achieved with 4 A running through the Z-wires and 0.76 mT of bias field, by just switching off the lower end wire after the U-MOT stage (a). (b) and (c) are the contour plots on the xy (top) and xz (bottom) planes of the Ioffe-Pritchard trap. (d), (e) and (f) show the magnetic potential in the three spatial directions. The insets in (d) and (e) are zooms into the center of the trapping potential, showing that at this point it has a smooth change and therefore, is a harmonic potential in the x and y directions.

the Ioffe-Pritchard trap by adding a bias field in the y-direction. The second factor causing an inefficient atom transfer between traps is that no optical pumping is done before magnetic trapping. It is possible to increase the number of transferred atoms by optically pumping the atoms to the $5S_{1/2}, |F = 2, m_F = 2\rangle$ sub-level. This would increase the atom population inside the trap by a factor up to 2.5 because it enables us to trap the atoms that originally occupied the non-trapped sub-levels of the ground state: $m_F = -2, -1, 0$.

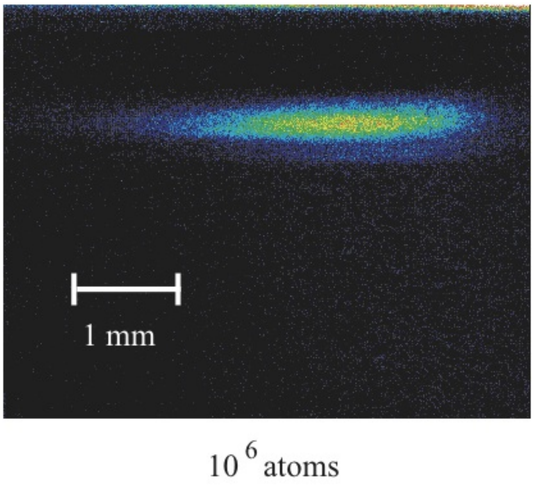

Figure 5.15: Absorption image of an atom cloud 3 ms after being released from the Ioffe-Pritchard trap on the 4Z-wire atom chip.

Loading 10^6 atoms into a Ioffe-Pritchard trap is the last experiment reported in thesis. The next generation of atom chips with the same design and improved surface arrived. This gave our group the opportunity to update the BEC apparatus in view of our experience with the atom chip of the first generation and ideas that we learned from other research groups working on similar projects. All the modifications that have been carried out on the experiment to receive the second generation of 4Z-wire chips are beyond the scope of this thesis.

5.7 Outlook

The next generation of 4Z-wire atom chips is ready to be used by our group. The gold layer of this chip is thinner (h_0=3 μm) as dictated by the results on spin flips near surfaces by us and other groups. It has been deposited by evaporation and patterned with ion beam milling. These techniques have been chosen because they produce smoother surfaces and edges than techniques such as electroplating and wet-etching [117]. One of these atom chips has already been incorporated into the BEC apparatus and atoms are being magnetically trapped following the routine explained in Section 5.6. The next steps with this atom chip are obvious: to reach BEC and to probe the surface with atoms. Once the the surface of this atom-chip is tested, it should be possible to proceed with interferometry experiments.

Chapter 6

Summary and conclusions

Detailed studies of two decoherence effects in microtraps have been presented in this thesis. Thermally induced spin flips were observed and compared with theoretical predictions resulting in good agreement. Atom cloud fragmentation due to corrugations in the DC field of a magnetic trap was also investigated. Our results contributed to a full understanding of both decoherence phenomena which in turn led to improvements in the design of atom chips.

These results were followed by the description of our first steps toward the achievement of a full-quantum control of ultra-cold atoms and condensates on atom chips. These steps are: the inclusion of a new atom chip (with more complex wire patterns on its surface) to our BEC apparatus and the first experiments in which magnetic trapping of atoms has been achieved with the new atom chip.

6.1 Thermal spin flips

The magnetic coupling between the surface's thermal field and atomic spin results in atom loss from microtraps. We measured the atom loss due to this interaction [56] in a Ioffe-Pritchard microtrap.

The lifetime of the magnetically trapped atoms was vacuum limited to more than one hundred seconds for atom clouds confined at further than two hundred microns from the surface of our guide wire. At shorter distances from the surface, the spin coupling to the RF-thermal radiation of the guide wire shortens the trapped state lifetime down to a couple of seconds. We studied the dependence of the atom loss rate on the distance to the wire for two different resonant frequencies: 0.56 and 1.8 MHz. The measured lifetimes were initially compared with theoretical values from an infinite plane slab [55]. Subsequently, a more appropriate comparison became possible when Rekdal *et al.* [57] generalized the theory to an arbitrary geometry of the thermal surface and did the calculations for the particular case of our cylindrical guide wire. Close agreement with our experimental results was found.

Our results in combination with theory [57] can therefore, provide us with guidance to optimize the atom-chip fabrication by predicting the best composition and thickness for the surface layers.

6.2 Atom-cloud fragmentation

We probed the DC field of our guide wire with cold atoms and investigated the dependence of the anomalous component (which causes fragmentation) on the distance to the atom-chip surface. The field behaviour revealed by our data reproduces the decay that one would expect from a meandering current inside the wire which decays as a Bessel function of the second kind. We surmised that these current-density fluctuations are caused by imperfections of the internal structure of our guide wire.

Theoretical and experimental research by other groups on atom-cloud fragmentation near wires demonstrated that imperfections in their surface and edges can also cause corrugations of the DC field induced when running a current, but that was not the case for our wire.

Our work on atom cloud fragmentation has contributed to finding the best techniques and materials to fabricate wires for atom chips. The most recent results indicate that evaporation to deposit the gold layer and electron beam milling to pattern the wires minimize trapping potential corrugations and are therefore, the most appropriate techniques.

6.3 Next steps

Following the understanding of thermal spin flips and atom-cloud fragmentation near surfaces, our group is now ready to pursue quantum control of atoms using atom chips. As a result of the progress reported here, a micro-fabricated atom chip is now installed in the BEC apparatus and our firsts steps have been made to load cold atoms into microtraps created with this atom-chip design. The next step is to evaporate atoms down to BEC and to probe the new atom chip with cold atoms to confirm the expected improvements, in lifetime and field corrugation, have been achieved.

These atom chips were designed to perform matter-wave interferometry in the double guide scheme [108] with pure DC magnetic fields. Splitting a BEC in this scheme has been recently achieved [39]. However no deterministic interference between condensates was observed with just pure DC magnetic fields. To achieve BEC coherent splitting, the static magnetic fields in that experiment were assisted by an optical field. This was required because the double-guide wire scheme for BEC splitting has a hexapole trap at the guide merging point. This gives low trap frequencies, making it difficult to achieve adiabatic splitting of the cloud. These are technical difficulties to be considered when choosing the method by which condensates will be split on the new atom chip. An alternative method is to dynamically split a Ioffe-Pritchard microtrap with RF magnetic fields as recently demonstrated [40]. In this experiment, the RF fields were supplied by a wire lying next to the guide wire. This splitting scheme can be realized with our atom chip and thus, it is worthwhile for our group to explore.

Appendix A

Angular factor S_{if}^2

I calculated the angular factors S_{if}^2 for the two transitions $|2\rangle \rightarrow |1\rangle$ and $|1\rangle \rightarrow |0\rangle$ by a direct application of Equation (3.10).

Each $|F\ m_F\rangle$ sub-level is a linear combination of electron and nuclear spin eigenvectors in terms of their Clebsch-Gordon (C-G) coefficients,

$$|I\ S\ F\ m_F\rangle = \sum_{m_I, m_s} \langle I\ S\ m_I\ m_s|\ F\ m_F\rangle|\ I\ m_I\rangle|\ S\ m_S\rangle. \tag{A.1}$$

The non-vanishing G-C coefficients give rise to the following expansions of the $|F\ m_F\rangle$ sub-levels:

$$\begin{aligned}
|2\rangle = |2\ 2\rangle &= |\ 3/2,\ 3/2\ \rangle|\ 1/2,\ 1/2\rangle \qquad (A.2)\\
|1\rangle = |2\ 1\rangle &= \frac{\sqrt{3}}{2}|\ 3/2,\ 1/2\rangle|\ 1/2,\ 1/2\rangle + \frac{1}{2}|\ 3/2,\ 3/2\rangle|\ 1/2,\ -1/2\rangle\\
|0\rangle = |2\ 0\rangle &= \frac{1}{\sqrt{2}}\big\{|\ 3/2,\ 1/2\rangle|\ 1/2,\ -1/2\rangle + |\ 3/2,\ -1/2\ \rangle|\ 1/2,\ 1/2\rangle\big\}.
\end{aligned}$$

The angular factor S_{if}^2 for each transition is calculated by adding up the matrix elements of the three q-spatial directions in Equation (3.10):

$$S_{if}^2 = |\langle i|\hat{S}_x|f\rangle|^2 + |\langle i|\hat{S}_y|f\rangle|^2 + |\langle i|\hat{S}_z|f\rangle|^2 = 2|\langle i|\hat{S}_x|f\rangle|^2. \tag{A.3}$$

The operator $\hat{S}_z$ does not cause a spin flip in this frame of reference and thus, its contribution to the angular factor is zero. Moreover, Equation A.3 uses the fact that the two transverse matrix elements, in x and y, have the same absolute value.

$\hat{S}_x$ can be expressed in terms of the Pauli matrix σ_1,

$$\hat{S}_x = \frac{1}{2}\begin{pmatrix} 0 & 1 \\ 1 & 0 \end{pmatrix}. \tag{A.4}$$

Thus, using Equation A.2 the matrix element of $\hat{S}_x$ for the first transition is

$$\langle 1|\hat{S}_x|2\rangle = \frac{1}{2}\begin{pmatrix} 0 & 1 \end{pmatrix}\begin{pmatrix} 0 & 1/2 \\ 1/2 & 0 \end{pmatrix}\begin{pmatrix} 1 \\ 0 \end{pmatrix} = \frac{1}{4}, \tag{A.5}$$

where $\begin{pmatrix} 1 \\ 0 \end{pmatrix}$ and $\begin{pmatrix} 0 \\ 1 \end{pmatrix}$ represent the eigenvectors with spin projection 1/2 and -1/2 respectively. Therefore the angular factor for this transition is

$$S^2_{21} = 2|\langle 1|\hat{S}_x|2\rangle|^2 = \frac{1}{8}. \tag{A.6}$$

Similarly, for the transition $|1\rangle \rightarrow |0\rangle$ the matrix element of $\hat{S}_x$ is given in terms of the expansions in Equation A.2 and σ_1,

$$\langle 0|\hat{S}_x|1\rangle = \frac{\sqrt{3}}{2\sqrt{2}}\begin{pmatrix} 0 & 1 \end{pmatrix}\begin{pmatrix} 0 & 1/2 \\ 1/2 & 0 \end{pmatrix}\begin{pmatrix} 1 \\ 0 \end{pmatrix} = \frac{\sqrt{3}}{4\sqrt{2}}. \tag{A.7}$$

Hence the angular factor for this transition is given by

$$S^2_{10} = 2|\langle 0|\hat{S}_x|1\rangle|^2 = \frac{3}{16}. \tag{A.8}$$

Appendix B

Atom loss data

Here I present in detail the experimental results from measuring the thermal spin-flip rate in our magnetic trap as a function of the distance d to the wire.

Table B.1 shows the number N of atoms in microtraps with 1.8 MHz spin-flip frequency for different times t of confinement. In these measurements, atoms were counted from absorption images as explained in Section 3.4.3. Each set of the data shown in Table B.1 is labelled with the distance d to the wire at which atoms where counted, and is one out of five measurements of the trap's lifetime $\tau(d) = 1/\Gamma(d)$. It gives a decay curve of the atom population in the trap, a line if one plots the logarithm of N against the time as shown in Figure B.1. A least squares fit to the data for each distance d is shown red in Figure B.1. Its slope is the loss rate $\Gamma(d)$, the spin-flip rate R_{21} from which each lifetime $\tau(d)$ shown in Table 3.1 and Figure 3.10 was deduced; the uncertainty of these measurements is given by the least squares fit.

The equivalent data, atom number N(t) and loss rate $\Gamma(d)$, for the 560 kHz spin-flip frequency is shown in Table B.2. We measured the lifetime $\tau(d)$ of the magnetic trap at seven different distances d from the wire for this frequency. These data are illustrated by the coloured symbols that, together with their correspondent fitted lines, are plotted in Figure B.2. Here the atom-loss rate $\Gamma(d)$ is also given by the slope of the least squares fit for each distance d, yielding the lifetimes shown in Table 3.1 and Figure 3.11.

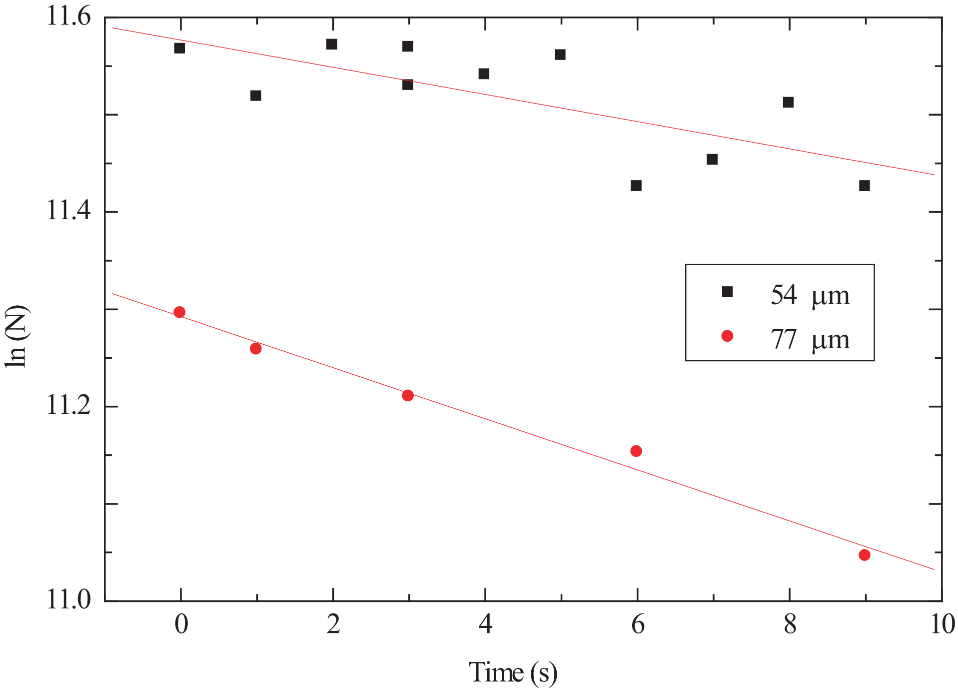

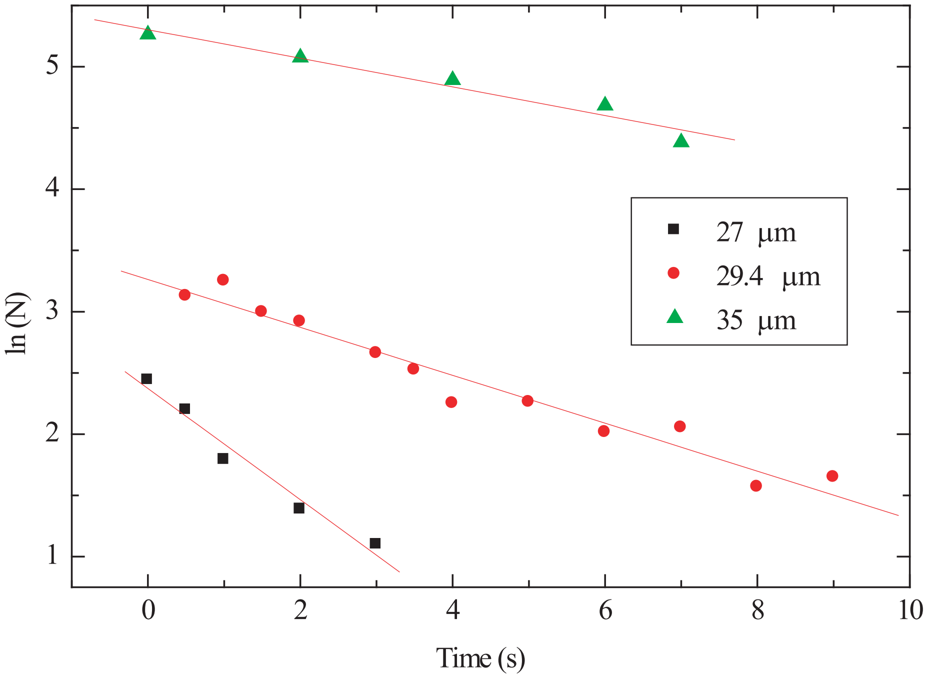

Figure B.1: The coloured symbols in both graphs are the natural logarithm of the number N of atoms counted at different times in magnetic traps with 1.8 MHz spin-flip frequency. An 1.5 to 3.5 offset has been included in $\ln(N)$ for clarity of the graphs. Each set of data was taken for different atom-surface distance d as labelled by the insets. The red lines are fitted by least squares, their slopes are the atom-loss rates $\Gamma(d)$ at each distance d, equal to the spin-flip rate R_{21}.

		t (s)	N			t (s)	N
$d\,(\pm 1.4\,\mu$m$)$	27	0	2622	$d\,(\pm 1.4\,\mu$m$)$	29.4	0.5	5198
Γ (s^{-1})	0.45 ± 0.046	2	912	Γ (s^{-1})	0.2 ± 0.014	2	4218
		1	1368			4	2166
		3	684			3	3260
		0.5	2052			1	5882
						5	2189
						6	1710
						7	1778
						9	1186
						8	1094
						1.5	4560
						3.5	2850
		t (s)	N			t (s)	N
$d\,(\pm 1.4\,\mu$m$)$	35	0	44004	$d\,(\pm 1.4\,\mu$m$)$	54	0	75468
Γ (s^{-1})	0.12 ± 0.015	6	24624	Γ (s^{-1})	0.0263 ± 0.0018	3	80484
		2	36480			6	73872
		4	30324			1	77520
		7	18240			9	62700
						7.5	69540
		t (s)	N	t (s)	N		
$d\,(\pm 1.4\,\mu$m$)$	77	0	105564	3	101688		
Γ (s^{-1})	0.0140 ± 0.0044	9	91656	6	91656		
		5	104880	1	100548		
		2	106020	4	102828		
		8	99864	7	94164		
		3	105792				

Table B.1: Record of the atom number N as a function of time for several distances d to the wire's surface. These are our experimental results for the 1.8 MHz spin-flip frequency. The reported rates Γ are obtained by fitting a line to the atom population decay as shown in Figure B.1.

		t (s)	N			t (s)	N
d ($\pm$ 1.4 μm)	27	3	4560	d ($\pm$ 1.4 μm)	27	2	6156
Γ (s^{-1})	0.47 ± 0.042	3.5	3192	Γ (s^{-1})	0.71 ± 0.07	0	38076
		1	11172			1	12540
		2	5130			4	2052
		1.5	9120			3	3420
		2.5	5700				
		3.5	3192				
		0.5	12996				
d ($\pm$ 1.4 μm)	35	5	32376	d ($\pm$ 1.4 μm)	54	5	49020
Γ (s^{-1})	0.19 ± 0.007	2	60192	Γ (s^{-1})	0.12 ± 0.008	9	27588
		7	22800			3	57000
		3	47196			7	37620
		3	49932			1.5	67260
		6	28500				
d ($\pm$ 1.4 μm)	54	0	53124	d ($\pm$ 1.4 μm)	71	0	67032
Γ (s^{-1})	0.12 ± 0.006	5	29640	Γ (s^{-1})	0.06 ± 0.001	5	59508
		2	44460			2	67260
		8	20292			8	50388
d ($\pm$ 1.4 μm)	88	5	50160			1	70452
Γ (s^{-1})	0.06 ± 0.001	8	46968			9	38304
		1	53124			7	43776
		7	43320			1	65208
		2	55404			0.5	68172
		3	50616			8.5	37392
		9	36936			3	58368
		0	53808				

Table B.2: Record of the atom number N as a function of time for several distances d to the wire's surface. These are our experimental results for the 0.56 MHz spin-flip frequency. The reported rates Γ are obtained by fitting a line to the atom population decay as shown in Figure B.2.

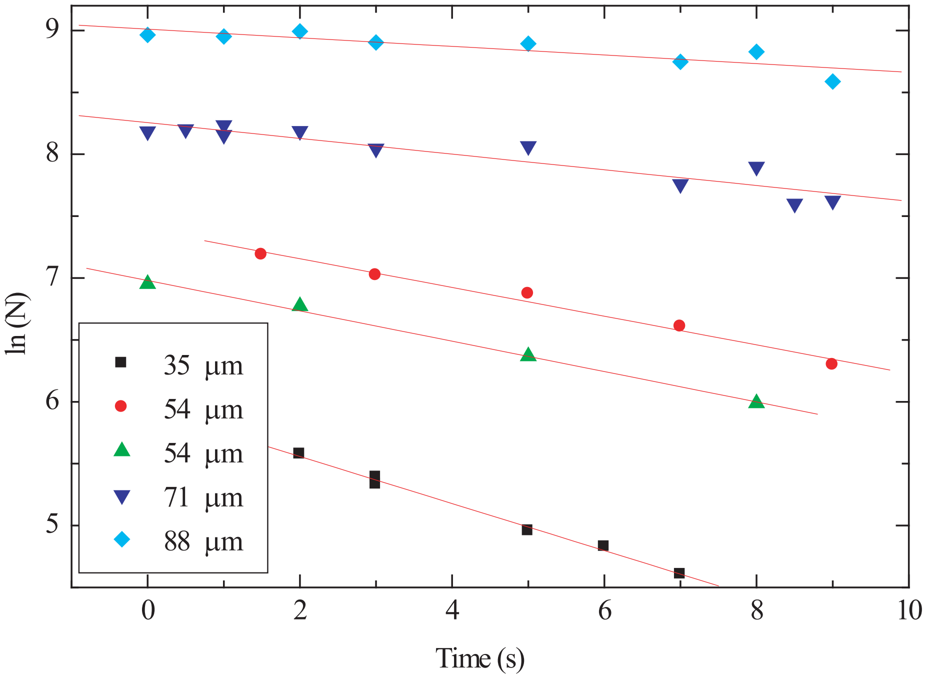

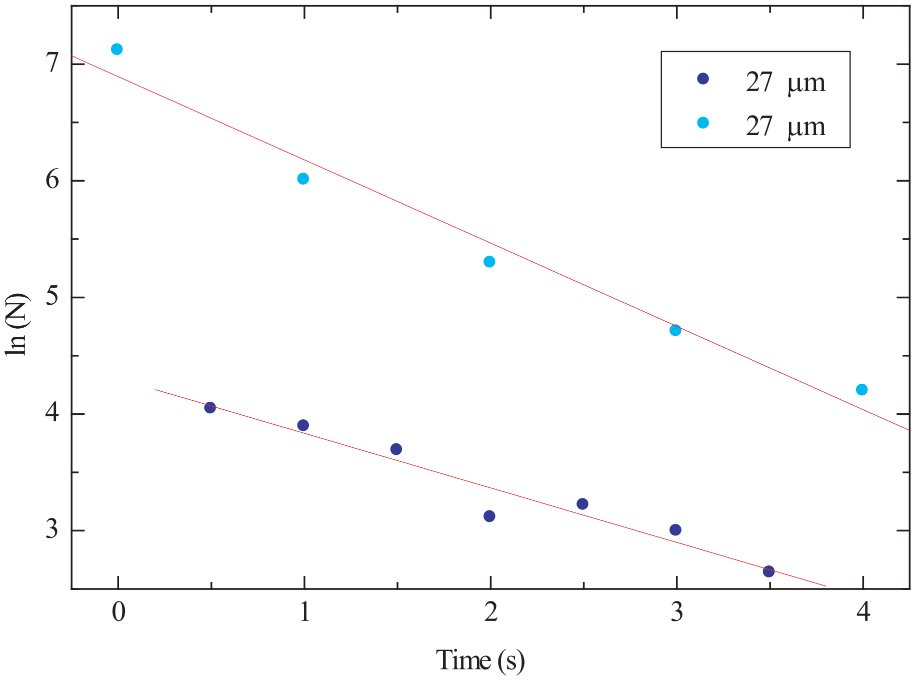

Figure B.2: Plot of $\ln(N)$ versus time for 560 kHz spin-flip frequency. Each set of data, shown by the coloured symbols, was taken for different atom-surface distances d, labelled in the insets. The red lines were fitted by least squares. Their slopes are the atom-loss rates $\Gamma(d)$ at each distance d from the wire, equal to the thermal spin-flip rate R_{21}.

Appendix C

Temperature of the guide wire

The interpolated temperatures represented by the circles in Figure 3.14 were deduced with a linear model for the temperature of the wire as a function of the power dissipated

$$T_{\text{wire}} = T_0 + kRI^2, \tag{C.1}$$

where T_0 =297 K, k is a constant that characterizes the details of the flow, R is the resistance of the guide wire and I is the current. The resistance changes with temperature as

$$R(T) = R_0[1 + \alpha(T_{\text{wire}} - T_0)], \tag{C.2}$$

where R_0 is the resistance at T_0 and α is the coefficient of the resistance. Thus from Equation (C.1), the change in temperature $\Delta T = T_{\text{wire}} - T_0$ is given, to a first approximation by

$$\Delta T = kR_0I^2 + k^2R_0^2\alpha I^4. \tag{C.3}$$

The interpolated points in Figure 3.14 were obtained by fitting a polynomial with the form

$$T = a_1I^2 + a_2I^4 \tag{C.4}$$

to the values of temperature measured at fixed time. The coefficients a_1 and a_2 were the fitting parameters, meaning in effect that we measured the constant k of our atom chip.

Appendix D

Ballistic-expansion measurements

Ballistic expansion is a well known method to measure the temperature of cold atom clouds in any of the three spatial directions. It is carried out by releasing an atom cloud from confinement and observing the dependence of its size on time while expanding. Here I explain our measurements of temperature along z, see Figure 5.12.

It is assumed that the velocity distribution of atoms is well described by the Gaussian

$$\rho(v) = \frac{1}{\sqrt{2\pi}\sigma} e^{-v^2/2\sigma^2}, \tag{D.1}$$

where the variance is

$$\sigma = \langle v^2 \rangle = \frac{k_B T}{m}. \tag{D.2}$$

By replacing $v \to (z - z_0)/t$ in Equation (D.1), where z_0 is the initial position of an atom in the cloud and z is its position at time t, we see that the density distribution with explicit time dependence is

$$\rho(z - z_0/t) = \frac{1}{\sigma(t)\sqrt{2\pi}} e^{-\frac{(z-z_0)^2}{2\sigma^2(t)}}, \tag{D.3}$$

where

$$\sigma^2(t) = \langle (z - z_0)^2/t^2 \rangle = \frac{k_B T t^2}{m}. \tag{D.4}$$

Thus the distribution of atoms [from Equation (4.2)] is given by

$$dN = \frac{1}{\sqrt{2\pi}\sigma} \int_{-\infty}^{\infty} e^{-\frac{(z-z_0)^2}{2\sigma^2(t)}} \frac{1}{\sqrt{2\pi}\sigma_0} e^{-\frac{z_0^2}{2\sigma_0^2}} dz, \tag{D.5}$$

where $\sigma_0 = \frac{1}{\omega}\frac{k_B T}{m}$ is the initial radius of the density distribution, ω the trap frequency and m the mass of atoms.

When the trapping fields are turned off, the atoms expand and hence, the atom distribution becomes time dependent given by Equation (D.5), which is the convolution

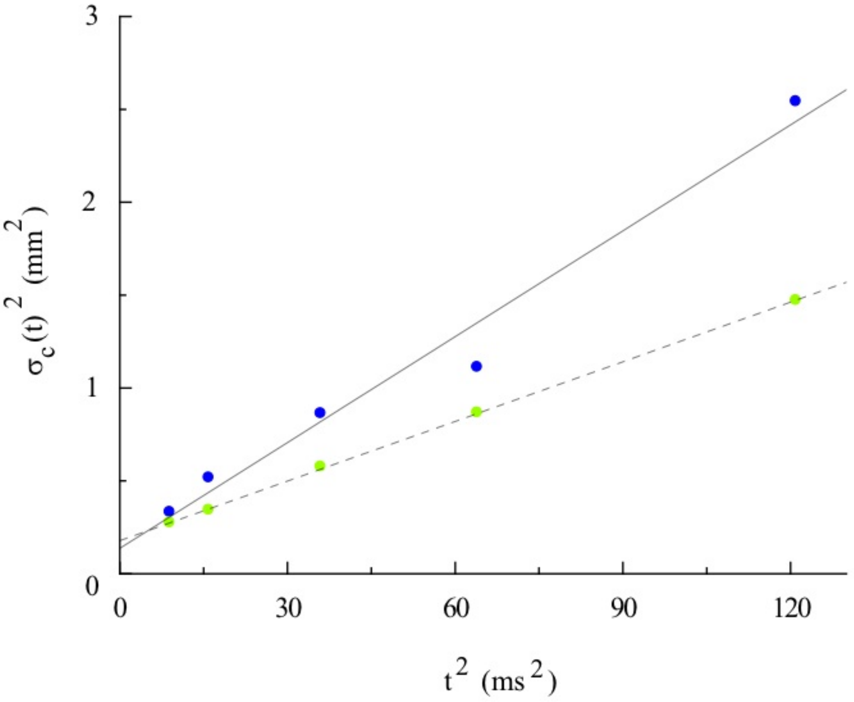

Figure D.1: Temperature measurement by ballistic expansion of the mirror and U-MOT on the 4Z-wire chip. The blue and green circles are the squared size of the mirror and U-MOT at diverse expansion times. The solid and dashed lines are linear fits to the data of the mirror and U-MOT respectively. These fits yield the temperatures of 200 and 112 μK reported by Section 5.6.

of two Gaussian distributions. For this particular case it can be shown [87] that after an expansion time τ, the thermal distribution given by Equation (D.5) is also well described by a Gaussian whose variance is given by

$$\sigma_c^2(\tau) = \sigma_0^2 + \frac{k_B T \tau^2}{m}. \tag{D.6}$$

The temperature is measured by imaging atom clouds after several different expansion times, fitting a Gaussian to each probability distribution of atoms and plotting $\sigma_c^2(t)$ against t^2.

The temperature measurements of both the mirror-MOT and the U-MOT are shown in Figure D.1. The blue circles are the squared radii of mirror-MOT atom clouds. The solid line is a linear fit to these data which yields a measured temperature of 200 μK, as discussed in Section 5.6.1. The green circles in Figure D.1 are the experimental data taken to measure the U-MOT temperature. A linear fit (dashed line) to this data allowed us to measure T=112 μK as discussed in Section 5.6.2.

Bibliography

[1] W. Gerlach and O. Stern, *Der experimentelle nachweis des magnetischen moments des silberatoms*, Zeitschrift f. Physik 8, **110** 126 (1921).

[2] T. H. Maiman, *Stimulated optical radiation in Ruby*, Nature, **187** 493 (1960).

[3] D. J. Wineland, R. E. Drullinger and F. L. Walls, *Radiation-pressure cooling of bound resonant absorbers*, Phys. Rev. Lett., **40** 1639 (1978).

[4] S. Andreev, V. Balykin, V. Letokhov and V. Minogin, *Radiative slowing and reduction of the energy spread of a beam of sodium atoms to 1.5 k in an oppositely directed laser beam*, JETP Lett., **34** 442 (1981).

[5] W. D. Phillips, *Laser decelaration of an atomic beam*, Phys. Rev. Lett., **48** 596 (1982).

[6] S. Chu, L. Hollberg, J. E. Bjorkholm, A. Cable and A. Ashkin, *Three-dimensional viscous confinement and cooling of atoms by resonance radiation pressure*, Phys. Rev. Lett., **55** 48 (1985).

[7] P. Lett, R. N. Watts, C. I. Westbrook, W. D. Phillips, P. L. Gould and H. Metcalf, *Observation of atoms laser cooled below the doppler limit*, Phys. Rev. Lett., **61** 169 (1988).

[8] J. Dalibard and C. Cohen-Tannoudji, *Laser cooling below the doppler limit by polarization gradients: Simple theoretical models*, J. Opt. Soc. Am. B, **6** 2023 (1989).

[9] P. Lett, W. Phillips, S. Rolston, C. Tanner, R. Watts and C. I. Westbrook, *Optical molasses*, J. Opt. Soc. Am. B, **6** 2084 (1989).

[10] A. Migdall, J. Prodan, T. Bergeman, H. Metcalf and W. Phillips, *First observation of magnetically trapped neutral atoms*, Phys. Rev. Lett., **54** 2596 (1985).

[11] S. Chu, J. Bjorkholm, A. Ashkin and A. Cable, *Experimental observation of optically trapped atoms*, Phys. Rev. Lett., **57** 314 (1986).

[12] M. Anderson, J. Ensher, M. Matthews, C. Wiemann and E. A. Cornell, *Observation of Bose-Einstein condensation in a dilute atomic vapor*, Science, **269** 198 (1995).

[13] C. C. Bradley, C. A. Sackett, J. J. Tollett and R. Hulet, *Bose-Einstein Consensation in an atomic gas with attractive interactions*, Phys. Rev. Lett., **75** 1687 (1995).

[14] K. B. Davis, M. O. Andrews, N. J. van Druten, D. S. Durfee, D. M. Kurn and W. Ketterle, *Bose-Einstein consensation in a gas of sodium atoms*, Phys. Rev. Lett., **75** 3969 (1995).

[15] H. F. Hess, G. P. Kochanski, J. M. Doyle, N. Masuhara, D. Kleppner and T. J. Greytak, *Magnetic trapping of spin-polarized atomic hydrogen*, Phys. Rev. Lett., **59** 672 (1987).

[16] Y. B. Ovchinnikov, S. Shul'ga and V. I. Balykin, *An atomic trap based on evanescent light waves*, J. Phys. B, **24** 3173 (1991).

[17] Y. B. Ovchinnikov, I. Manek and R. Grimm, *Surface trap for Cs atoms based on evanescent-wave cooling*, Phys. Rev. Lett., **79** 2225 (1997).

[18] Y. B. Ovchinnikov, I. Manek and R. Grimm, *Optical traps for quantum gases*, Appl. Phys. B, **67** 709 (1998).

[19] M. J. Renn, D. Montgomery, O. Vdovin, D. Anderson, C. E. Wiemann and E. A. Cornell, *Laser-guided atoms in hollow-core optical fibers*, Phys. Rev. Lett., **75** 3253 (1995).

[20] J. Schmiedmayer, *Quantum wires and quantum dots for neutral atoms*, Eur. Phys. J. D, **4** 57 (1998).

[21] W. G. Kaenders, F. Lison, I. Muüller, A. Ritcher, R. Wynands and D. Meschede, *Refractive components for magnetic atom optics*, Phys. Rev. A, **54** 5067 (1996).

[22] J. Schmiedmayer, *Guiding and trapping nuetral atoms on a wire*, Phys. Rev. A, **52** 13 (1995).

[23] J. Denschlag, D. Cassettari and J. Schmiedmayer, *Guiding neutral atoms with a wire*, Phys. Rev. Lett., **88** 2014 (1999).

[24] J. Weinstein and K. Libbrecht, *Microscopic magnetic traps for neutral atoms*, Phys. Rev. A, **52** 4004 (1995).

[25] J. Thywissen, M. Olshanii, G. Zabow, M. Drndic, K. Johnson, R. Westervelt and M. Prentiss, *Microfabricated magnetic waveguides for neutral atoms*, Eur. Phys. J. D, **7** 361 (1999).

[26] E. A. Hinds and I. G. Hughes, *Magnetic atom optics: mirrors, guides, traps and chips for atoms*, J. Phys. D: Appl. Phys., **32** 119 (1999).

[27] M. Key, I. G. Hughes, W. Rooijakkers, B. E. Sauer and E. A. Hinds, *Propagation of cold atoms along a miniature magnetic guide*, Phys. Rev. Lett., **84** 1371 (2000).

[28] J. Reichel, W. Hänsel and T. W. Hänsch, *Atomic micromanipulation with magnetic surface traps*, Phys. Rev. Lett., **83** 3398 (1999).

[29] J. Denschlag, D. Cassettari, A. Chenet and J. Schmiedmayer, *A neutral atom and a wire: towards mesoscopic atom optics*, Appl. Phys. B, **69** 291 (1999).

[30] N. H. Dekker, C. S. Lee, V. Lorent, J. Thywissen, S. P. Smith, M. Drndic, R. M. Westervelt and M. Prentiss, *Guiding neutral atoms on a chip*, Phys. Rev. Lett., **84** 1124 (2000).

[31] D. Müller, D. Z. Anderson, R. J. Grow, P. D. D. Schwindt and E. A. Cornell, *Guiding neutral atoms around curves with lithographically patterned current-carrying wires*, Phys. Rev. Lett., **83** 5194 (1999).

[32] D. Cassettari, B. Hessmo, R. Folman, T. Maier and J. Schmiedmayer, *Beam splitter for guided atoms*, Phys. Rev. Lett., **85** 5483 (2000).

[33] W. Hänsel, J. Reichel, P. Hommelhoff and T. Hänsch, *Magnetic conveyor belt for transporting and merging trapped atom clouds*, Phys. Rev. Lett., **86** 608 (2001).

[34] H. Ott, J. Fortágh, G. Schlotterbeck, A. Grossmann and C. Zimmermann, *Bose-Einstein condensation in a surface microtrap*, Phys. Rev. Lett., **87** 230401 (2001).

[35] W. Hänsel, P. Hommelhoff, T. W. Hänsch and J. Reichel, *Bose-Einstein condensation on a microelectronic chip*, Nature, **413** 498 (2001).

[36] C. Vale, B. Hall, D. Lau, M. Jones, J. Retter and E. Hinds, *Atom chips*, Europhys. News., **33** (2002).

[37] M. P. A. Jones, *Bose-Einstein Condensation on an Atom Chip*, Ph.D. thesis, University of Sussex (2002).

[38] Y. J. Wang, D. Z. Anderson, V. M. Bright, E. A. Cornell, Q. D., T. Kishimoto, M. Prentiss, R. A. Saravanan, S. R. Segal and S. Wu, *Atom Michelson interferometer on a chip using a Bose-Einstein condensate*, Phys. Rev. Lett., **94** 090405 (2005).

[39] Y. Shin, C. Sanner, G.-B. Jo, T. A. Pasquini, M. Saba, W. Ketterle and D. E. Pritchard, *Interference of Bose-Einstein condensates on an atom chip*, Phys. Rev. A, **72** 021604 (2005).

[40] T. Schumm, S. Hofferberth, L. M. Andersson, S. Wildermuth, S. G. I. Bar-Joseph, J. Schmiedmayer and P. Krüger, *Matter-wave interferometry in a double well on an atom chip*, Nature, **1** 57 (2005).

[41] A. Günther, S. Kraft, M. Kemmler, D. Koelle, R. Kleiner, C. Zimmermann and J. Fortágh, *Diffraction of a Bose-Einstein condensate from a magnetic lattice on a microchip*, Phys. Rev. Lett., **95** 170405 (2005).

[42] A. Günther, S. Kraft, C. Zimmermann and J. Fortágh, *Atom interferometer based on phase coherent splitting of Bose-Einstein condensates with an integrated magnetic grating*, arXiv:cond-mat/0603631 v1 23 Mar 2006 (1985).

[43] T. M. Roach, H. Abele, M. G. Boshier, H. L. Grossman, K. P. Zetie and E. A. Hinds, *Realization of a magnetic mirror for cold atoms*, Phys. Rev. Lett., **75** 629 (1995).

[44] C. D. J. Sinclair, E. A. Curtis, I. L. Garcia, J. A. Retter, B. V. Hall, S. Eriksson, B. E. Sauer and E. A. Hinds, *Cold atoms in videotape micro-traps*, Eur. Phys. J. D, **35** 105 (2005).

[45] C. D. J. Sinclair, E. A. Curtis, I. L. Garcia, J. A. Retter, B. V. Hall, S. Eriksson, B. E. Sauer and E. A. Hinds, *Bose-Einstein condensation on a permanent-magnet atom chip*, Phys. Rev. A, **72** 031603.

[46] S. Eriksson, F. Ramirez-Martinez, E. Curtis, B. Sauer, , P. Nutter, E. Hill and E. Hinds, *Micron-sized atom traps made from magneto-optical thin films*, Appl. Phys. B, **79** 811 (2004).

[47] P. Horak, B. G. K. A. Haase, R. Folman, J. Schmiedmayer, P. Domokos and E. A. Hinds, *Possibility of single-atom detection on a chip*, Appl. Phys. B, **79** 811 (2003).

[48] S. Eriksson, M. Trupke, H. Powell, D. Sahagun, C. Sinclair, E. Curtis, B. Sauer, E. Hinds, Z. Moktadir, C. Gollasch and M. Kraft, *Integrated optical components on atom chips*, Eur. Phys. J. D, **35** 135 (2005).

[49] A. Görlitz, J. M. Vogels, A. E. Leanhardt, C. Raman, T. L. Gustavson, J. R. Abo-Shaeer, A. P. Chikkatur, S. Gupta, S. Inouye, T. Rosenband and W. Ketterle, *Realization of Bose-Einstein condensates in lower dimensions*, Phys. Rev. Lett., **87** 130402 (2001).

[50] M. Olshanii, *Atomic scattering in the presence of an external confinement and a gas of impenetrable bosons*, Phys. Rev. Lett., **81** 938 (1998).

[51] D. W. Vernooy, A. Furusawa, N. P. Georgiades, V. S. Ilchenko and H. J. Kimble, *Cavity QED with high-Q whispering gallery modes*, Phys. Rev. A, **57** 2293 (1998).

[52] P. W. H. Pinkse, T. Fischer, P. Maunz and G. Rempe, *Trapping an atom with single photons*, Nature, **404** 365 (2000).

[53] T. Calarco, E. A. Hinds, D. Jaksch, J. Schmiedmayer, J. I. Cirac and P. Zoller, *Quantum gates with neutral atoms: Controlling collisional interactions in time-dependent traps*, Phys. Rev. A, **61** 022304 (2000).

[54] S. Scheel, J. Pachos, E. A. Hinds and P. L. Knight, *Quantum Coherence, Lecture notes in Physics 689* (Springer, Berlin, 2006).

[55] C. Henkel, S. Pötting and M. Wilkens, *Loss and heating of particles in small and noisy traps*, Appl. Phys. B, **69** 379 (1999).

[56] M. P. A. Jones, C. J. Vale, D. Sahagun, B. Hall and E. A. Hinds, *Spin coupling between cold atoms and the thermal fluctuations of a metal surface*, Phys. Rev. Lett., **91** 080401 (2003).

[57] P. K. Rekdal, S. Scheel, P. L. Knight and E. A. Hinds, *Thermal spin flips in atom chips*, Phys. Rev. A, **70** 013811 (2004).

[58] M. P. A. Jones, C. J. Vale, D. Sahagun, B. V. Hall, C. C. Eberlein, B. E. Sauer, K. Furusawa, D. Richardson and E. A. Hinds, *Cold atoms probe the magnetic field near a wire*, J. Phys. B, **66** 15 (2004).

[59] C. J. Pethick and H. Smith, *Bose-Einstein Condensation in Dilute Gases*, first edition (Cambridge University Press, 2004).

[60] A. S. Arnold, J. Wilson and M. Boshier, *A simple extended cavity diode laser*, Rev. of Sci. Inst., **69** 1236 (1998).

[61] S. Bize, Y. Sortais, M. S. Santos, C. Mandache, A. Clairon and C. Salomon, *High-accuracy measurement of the* ^{87}*Rb ground-state hyperfine splitting in an atomic fountain*, Europhys. Letts., **45** 558 (1999).

[62] J. Ye, S. Swartz, P. Jungner and J. L. Hall, *Hyperfine structure and absolute frequency of the* ^{87}Rb *5*$P_{3/2}$ *state*, Opts. Lett., **21** 1280 (1996).

[63] P. Bender, E. Beaty and A. Chi, *Optical detection of narrow* Rb^{87} *hyperfine absorption lines*, Phys. Rev. Lett., **1** 311 (1958).

[64] B. Senitzky and I. Rabi, *Hyperfine structure of* $Rb^{85,87}$ *in the 5p state*, Phys. Rev. Lett., **103** 315 (1956).

[65] J. B. Jr., J. L. Bohn, B. D. Esry and C. H. Greene, *Prospects for mixed-isotope Bose-Einstein condensates in Rubidium*, Phys. Rev. Lett., **80** 2097 (1998).

[66] C. P. Pearman, C. S. Adams, S. G. Cox, P. F. Griffin, D. A. Smith and I. G. Hughes, *Polarization spectroscopy of a closed atomic transition: Applications to laser frequency locking*, J. Phys. B, **35** 5141 (2002).

[67] W. Demtröder, *Laser Spectroscopy: Basic Concepts and Instrumentation* (Springer, Berlin, London, 2003).

[68] U. Schünemann, H. Engler, R. Grimm, M. Weidemüller and M. Zielonkowski, *Simple scheme for tunable frequency offset locking of two lasers*, Rev. of Sci. Inst., **70** 242 (1999).

[69] Z. T. Lu, K. L. Corwin, M. J. Renn, M. H. Anderson, E. A. Cornell and C. E. Wieman, *Low-velocity intense source of atoms from a magneto-optical trap*, Phys. Rev. Lett., **77** 3331 (1996).

[70] K. Dieckmann, R. J. C. Spreew, M. Weidemüller and J. T. M. Walraven, *Two-dimensional magneto-optical trap as a source of slow atoms*, Phys. Rev. A, **58** 3891 (1998).

[71] J. Arlt, O. Marago, S. Webster, S. Hopkins and C. Foot, *A pyramidal magneto-optical trap as a source of slow atoms*, Opt. Commun., **157** 303 (1998).

[72] J. Reichel, W. Hänsel and T. W. Hänsch, *Atomic micromanipulation with magnetic surface traps*, Phys. Rev. Lett., **83** 3398 (1999).

[73] E. Raab, M. Prentiss, A. Cable, S. Chu and D. Pritchard, *Trapping of neutral sodium atoms with radiation pressure*, Phys. Rev. Lett., **59** 2631 (1987).

[74] E. A. Hinds, M. G. Boshier and I. G. Hughes, *Magnetic waveguide for trapping cold atom gases in two dimensions*, Phys. Rev. Lett., **80** 645 (1998).

[75] J. Fortágh, A. Grossmann, T. W. Hänsch and C. Zimmermann, *Fast loading of a magneto-optical trap from a pulsed thermal source*, J. Appl. Phys., **84** 6499 (1998).

[76] D. E. Pritchard, *Cooling atoms in a magnetic trap for precision spectroscopy*, Phys. Rev. Lett., **51** 1336 (1983).

[77] W. Ketterle and D. Pritchard, *Trapping and focusing ground state atoms with static fields*, Appl. Phys. B, **54** 403 (1992).

[78] T. Bergeman, G. Erez and H. Metcalf, *Magneto-static trapping fields for neutral atoms*, Phys. Rev. A, **35** 1535 (1987).

[79] E. Majorana, *Atomi orientati in campo magnetico variabile*, Nuovo Cimento, **9** 43 (1932).

[80] N. F. Ramsey, *Molecular beams*, The international series of monographs in physics (Oxford University Press, Oxford, 1956).

[81] T. Schumm, J. Estève, C. Figl, J.-B. Trebbia, C. Aussibal, H. Nguyen, D. Mailly, C. W. I. Bouchoule and A. Aspect, *Atom chips in the real world: the effects of wire corrugation*, Eur. Phys. J. D, **32** 171 (2005).

[82] P. Krüger, S. Wildermuth, S. Hofferberth, L. M. Andersson, S. Groth, I. Bar-Joseph and J. Schmiedmayer, *Cold atoms close to surfaces: Measuring magnetic field roughness and disorder potentials*, J. Phys.: Conference Series, **19** 56 (2005).

[83] D. W. Snoke and J. P. Wolfe, *Population dynamics of a bose gas near saturation*, Phys. Rev. B, **39** 4030 (1987).

[84] A. Arnold, *Preparation and Manipulation of an ^{87}Rb Bose-Einstein Condensate*, Ph.D. thesis, University of Sussex (1999).

[85] V. Bagnato, D. E. Pritchard and D. Kleppner, *Bose-Einstein Condensation in an external potential*, Phys. Rev. A, **35** 4354 (1987).

[86] O. J. Luiten, M. W. Reynolds and J. T. M. Walraven, *Kinetic theory of the evaporative cooling of a trapped gas*, Phys. Rev. A, **53** 381 (1996).

[87] R. Loudon, *The Quantum Theory of Light*, Oxford Science Publications, second edition (Oxford University Press, Oxford, 1997).

[88] L. D. Landau and E. Lifshitz, *Statistical Physics*, Course of Theoretical Physics, third edition (Butterworth and Heimann, Oxford, 1997).

[89] J. B. Johnson, *Thermal agitation of electricity in conductors*, Phys. Rev., **32** 97 (1928).

[90] S. Scheel, P. Rekdal, P. Knight and E. Hinds, *Atomic spin decoherence near conducting and superconducting films*, Phys. Rev. A, **72** 042901 (2005).

[91] M. O. Scully and M. S. Zubairy, *Quantum Optics* (Cambridge University Press, Cambridge, 1999).

[92] L. D. Landau and E. Lifshitz, *Electrodynamics of Continous Media*, second edition (Pergamon, Oxford, 1960).

[93] J. D. Jackson, *Classical Electrodynamics*, third edition (John Wiley & Sons, Inc, New York, 1998).

[94] A. E. Leanhardt, Y. Shin, A. P. Chikkatur, D. Kielpinski, W. Ketterle and D. E. Pritchard, *Bose-Einstein condensates near a microfabricated surface*, Phys. Rev. Lett., **90** 100404 (2003).

[95] E. A. Hinds and V. Sandoghdar, *Cavity qed level shifts of simple atoms*, Phys. Rev. A, **43** 398 (1932).

[96] H. B. G. Casimir and D. Polder, *The influence of the retardation on the London-van der Waals forces*, Phys. Rev., **73** 360 (1948).

[97] C. Sukenik, M. G. Boshier, D. Cho, V. Sandoghdar and E. A. Hinds, *Measurement of the Casimir-Polder force*, Phys. Rev., **70** 560 (1993).

[98] P. H. W. Hänsel, J. Reichel and T. W. Hänsch, *Trapped-atom interferometer in a magnetic microtrap*, Phys. Rev. A, **64** 063607 (2001).

[99] J. Fortágh, H. Ott, S. Kraft, A. Gúnther and C. Zimmermann, *Surface effects in magnetic microtraps*, Phys. Rev. A, **66** 041604 (2002).

[100] P. K. Rekdal, U. Hohenester, A. Eiguren and B.-S. K. Skagerstam, *Spin decoherence in superconducting atom chips*, arXiv:quant-ph/0603229 v1 25 Mar 2006 (2006).

[101] A. S. Kraft, H. Ott, D. Wharam, C. Zimmermann and J. Fortágh, *Anomalous longitudinal magnetic field near the surface of copper conductors*, J. Phys. B, **35** 469 (2002).

[102] A. E. Leanhardt, Y. Shin, A. P. Chikkatur, D. Kielpinski, W. Ketterle and D. E. Pritchard, *Propagation of Bose-Einstein condensates in a magnetic waveguide*, Phys. Rev. Lett., **89** 040401 (2002).

[103] A. E. Leanhardt, Y. Shin, A. P. Chikkatur, D. Kielpinski, W. Ketterle and D. E. Pritchard, *Bose-Einstein condensates near a microfabricated surface*, Phys. Rev. Lett., **90** 100404 (2003).

[104] J. Estève, C. Aussibal, T. Schumm, C. Figl, D. Mailly, I. Bouchoule, C. I. Westbrook and A. Aspect, *Role of wire imperfections in micromagnetic traps for atoms*, Phys. Rev. A, **70** 043629 (2004).

[105] S. Wildermuth, S. Hofferberth, I. Lesanovsky, E. Haller, L. M. Andersson, S. Groth, I. Bar-Joseph, P. Krüger and J. Schmiedmayer, *Microscopic magnetic-field imaging*, Nature, **435** 400 (2005).

[106] M. Abramowitz and I. A. Stegun, *Handbook of Mathematical Functions.*

[107] D.-W. Wang, M. D. Lukin and E. Demler, *Disordered Bose-Einstein condensates in quasi-one-dimensional magnetic microtraps*, Phys. Rev. Lett., **92** 076802 (2004).

[108] E. A. Hinds, C. J. Vale and M. G. Boshier, *Two-wire waveguide and interferometer for cold atoms*, Phys. Rev. Lett., **86** 1462 (2001).

[109] E. Koukharenko, Z. Moktadir, M. Kraft, M. Abdelsalam, D. Bagnall, C. Vale, M. Jones and E. Hinds, *Microfabrication of gold wires for atom guides*, Sensors Actuat. A-Phys., **115** 600 (2004).

[110] P. Hommelhoff, W. Hänsel, T. Steinmetz, T. W. Hänsch and J. Reichel, *Transporting, splitting and merging of atomic ensembles in a chip trap*, New J. of Phys., **7** 3 (2005).

[111] M. Albiez, R. Gati, J. Fölling, S. Hunsmann, M. Cristiani and M. K. Oberthaler, *Direct observation of tunneling and nonlinear self-trapping in a single bosonic Josephson junction*, Phys. Rev. Lett., **95** 010402 (2005).

[112] C. Buggle, J. Léonard, W. von Klitzing and J.T.M.Walraven, *Interferomic determination of the s and (d)-wave scattering amplitudes in* ^{87}Rb, Phys. Rev. Lett., **93** 173202 (2004).

[113] M. R. Andrews, C. G. Townsend, H. J. Miesner, D. S. Durfee, D. M. Kurn and W. Ketterle, *Observation of interference between two Bose Condensates*, Science, **275** 637 (1997).

[114] C. D. J. Sinclair, *Bose-Einstein Condensation in Microtraps on a Videotape*, Ph.D. thesis, Imperial College, London (2006).

[115] S. Groth, P. Krüger, S. Wildermuth, R. Folman, T. Fernholz, J. Schmiedmayer, D. Mahalu and I. Bar-Joseph, *Atom chips: Fabrication and thermal properties*, Appl. Phys. Lett., **85** 2980 (2004).

[116] S. Wildermuth, P. Krger, C. Becker, M. Brajdic, S. Haupt, A. Kasper, R. Folman and J. Schmiedmayer, *Optimized magneto-optical trap for experiments with ultracold atoms near surfaces*, Phys. Rev. A, **69** 030901 (2004).

[117] G. Lewis, Z. Moktadir, C. O. Gollasch, M. Kraft, M. Trupke, S. Eriksson and E. A. Hinds, *Comparison of fabrication processes using electrochemical deposition of gold wires for atom guides*, Proceedings of 16th MME Micromechanics Europe workshop, 56 (2005).